



**MARMARA UNIVERSITY
INSTITUTE FOR GRADUATE STUDIES
IN PURE AND APPLIED SCIENCES**



**THE PRODUCTION OF ALUMINA-
TITANIA BIOCOMPOSITE COMBINED
WITH HYDROXYAPATITE (HA)**

BURCU NİLGÜN ÇETİNER

MASTER THESIS

Department of Metallurgical and Materials
Engineering

ADVISOR

Prof. Dr. Ziya Engin ERKMEN

ISTANBUL, 2014



MARMARA UNIVERSITY
INSTITUTE FOR GRADUATE STUDIES
IN PURE AND APPLIED SCIENCES



**THE PRODUCTION OF ALUMINA-
TITANIA BIOCOMPOSITE COMBINED
WITH HYDROXYAPATITE (HA)**

BURCU NİLGÜN ÇETİNER

(524709821)

MASTER THESIS

Department of Metallurgical and Materials
Engineering

ADVISOR

Prof. Dr. Ziya Engin ERKMEN

ISTANBUL, 2014

PREFACE

This was a long road walked on bare foot. During this walk, the suffer was permanent. But the success is the sum of the losses and failures we lived through this journey and the real men don't talk about their losses.

July, 2014

Burcu Nilgün ÇETİNER

ACKNOWLEDGMENT

This work was financially supported by The Marmara University Scientific Research Committee (FEN-C-031210-0288). I express sincere appreciation to Prof. Dr. Ziya Engin ERKMEN for his guidance and insight throughout the research , Prof.Dr. Faik OKTAR for allowing using his lab facilities and Assoc. Prof.Dr. Bora DERIN, for his consistent help for making FACT SAGE analysis. Also, we would like to thank Prof.Dr. Mustafa ÖKSÜZ and Res. Ass. S. Serdar PAZARLIOĞLU for their incredible support to measure the materials' mechanical properties, Prof.Dr. Gürcan ORALTAY and Dr.Eng. Mustafa İLHAN for their kindly help to monitorize the microstructure of the materials, Assoc. Prof. Dr. S. Sinan KESKİN and Res. Ass. Özgür ÇINAR for their sustained assistance to analyze our specimens. Thermal spray processing of the specimens was carried out in the surface engineering application company, Yüzey Muhendislik San. Tic. Ltd. Sti., without considering commercial interest, i also appreciate their contribution to scientific research.

This thesis can not be terminated without sustainable support of my family. But over all, this master thesis is dedicated to my beloved sister, Müberra Burçin ÇETİNER who passed away in 2009, at the age of 23.

July, 2014

Burcu Nilgün ÇETİNER

TABLE of CONTENTS

	PAGE
PREFACE	i
ACKNOWLEDGMENT	ii
TABLE of CONTENTS	iii
ÖZET	v
ABSTRACT	vi
SYMBOLS	vii
ABBREVIATIONS	viii
LIST of FIGURES	ix
LIST of TABLES	xv
1. INTRODUCTION	1
2. GENERAL BACKGROUND	2
2.1.1. Alumina	2
2.1.2. Seydişehir Alumina	5
2.2. Titania	6
2.3. Aluminum Titanate	8
2.4. Hydroxyapatite	17
2.5. Thermal Spray Coating Processes	22
2.6. Instruments Used in this Research	23
3. MATERIAL and METHOD	25
3.1. Experimental Setup	25
3.1.1. Materials Used in the Experiment	25
3.1.2. Experimental Setup of Each Procedure	25
4. RESULTS and DISCUSSION	38
4.1. Results and Discussion of Beneficiation of Seydişehir Alumina	38
4.1.1. Differential Thermal Analysis Results and Discussion	38
4.1.2. XRF Analysis Results and Discussion	39
4.1.3. XRD Analysis Results and Discussion	40
4.1.4. SEM Analysis Results and Discussion	41
4.1.5. Laser Particle Size Results and Discussion	41

4.2. Results and Discussion of Production of Alumina-Titania Biocomposite	42
4.2.1. Archimèdes Density Measurement Results and Discussion	42
4.2.2. XRD Analysis Results and Discussion	43
4.2.3. SEM and EDS Analysis Results and Discussion	45
4.2.4. Microhardness Testing Results and Discussion	55
4.2.5. Compressive Strength Testing Results and Discussion	57
4.3. Results and Discussion of Coating with HA the Alumina-Titania Substrate using Flame Spray Process	58
4.3.1. Microhardness Testing Results and Discussion	58
4.3.2. SEM and EDS Analysis Results and Discussion	60
5. CONCLUSION	71
REFERENCES	74
CURRICULUM VITAE	

ÖZET

Alümina 20 yıldan daha uzun bir süredir yüksek sertliğine eşlik eden düşük sürtünme, aşınma ve in vivo ortamda tepkimesizliği nedeni ile seçilen bir biyomalzemedir. Okside olan titanyumun rutil fazının biyouyumlu olduğu belirtilmiştir. Bu, biyocam ve sinterlenmiş hidroksilapatit (HA) gibi bazı seramiklerde keşfedilen bir özelliktir. Fakat alümina ve titanyanın meydana getirdiği tialit karışımı (Alüminyum titanat- 50 % mol Al_2O_3 ve 50 % mol TiO_2 yeni bir meydan okumadır. Bu çalışmada, ilk olarak Seydişehir alüminasını “Kral Suyu” asidik çözeltisinin içinde yıkayıp ıslahını, akabinde % ağı. 2.5, % ağı. 3.5, % ağı. 4.5 MgO ve % ağı. 1 SiO_2 ve kalanı alümina ve titania karışımı (1:1 mol) olacak şekilde harmanların hazırlanması sağlandı. 1600 °C ‘de 12 sa bu harmanları sinterledikten sonra, mekanik özellikleri (basma ve sertlik testi) ve faz oranları (XRD analizi) analiz edildi ve Seydişehir alüminası yerine laboratuvar ölçeğindeki alümina –analitik saflık- içeren kontrol grubu ile karşılaştırıldı. Altlık malzemesinin karakterizasyonunun ardından (SEM ve EDS analizi), iki farklı tür malzemenin karşılaştırılması gerçekleştirildi. Alümina-titanya biyokompozitinin üretimini takiben, alev spreysel prosesi kullanılarak sığır hidroksiapatiti ile ısıl püskürtme kaplaması uygulandı ve kaplama tabakalarının karakterizasyonu (SEM ve EDS analizi ve mikrosertlik ölçümleri) yapıldı.

Haziran , 2014

Burcu Nilgün ÇETİNER

ABSTRACT

Alumina is a biomaterial of choice for more than 20 years due to its high hardness accompanied by low friction, wear and inertness to in vivo environment. It has been reported that titanium oxidized to the rutile phase is bioactive. This is a property discovered for certain ceramics such as Bioglass and sintered hydroxylapatite (HA). But the combination of alumina and titania forming tialite (Aluminium titanate-50 mol % Al_2O_3 and 50 mol % TiO_2) is a new challenge. In this work we made firstly the beneficiation of the Seydişehir alumina by leaching it in the acidic solution “the Aqua Regia” followed by preparation of batches containing 2,5 wt %, 3,5 wt % and 4,5 wt % of MgO as the sintering aid, 1 wt % of SiO_2 and the balance; the alumina and titania powder mixture (1:1 mole). After sintering these batches at 1600 °C for about 12 h, their mechanical properties (the compression and hardness testings) and phase ratios (the XRD analysis) were analyzed and compared with the control group containing the laboratory scale (analytical purity) alumina instead of the Seydişehir alumina. Following the characterization (the SEM and the EDS analysis) of the substrate material, the comparison of two different kinds of materials was carried out. Following the production of the alumina-titania biocomposite, the thermal spray coating using the flame spray process by bovine hydroxyapatite was applied and the characterization of the coating layers (the SEM & EDS analysis and the microhardness measurements) was performed.

July, 2014

Burcu Nilgün ÇETİNER

SYMBOLS

E : Elastic Modulus

Å : Armstrong

°C: Celcius

α : Linear dilatation coefficient

Al₂O₃ : Aluminum Oxide-Alumina

SiO₂ : Silicium Oxide-Silica

Fe₂O₃ : Iron Oxide

Na₂O : Sodium Oxide

Al(OH)₃ : Aluminum hydroxide

CaO : Calcium oxide-Calcia

MgO : Magnesium oxide-Magnesia

TiO₂ : Titanium oxide-Titania

Al₂TiO₅ : Aluminum titanate

La₂O₃ : Lantalum oxide

SnO₂ : Tin oxide

C : Carbon

S : Silicium

ABBREVIATIONS

HA : Hydroxyapatite

EU : European Union

USA : United States of America

Ti-OH : Titanium hydroxide

Bov. HA : Bovine Hydroxyapatite

β-TCP : β-tricalcium phosphate

TTCP : Tetracalcium phosphate

ACP : Amorphous calcium phosphate

AT : Aluminum titanate

CaP : Calcium phosphate

SEM : Scanning Electron Microscopy

EDS : Energy Dispersive Spectrometry

XRF : X-Ray Fluorescence Spectrometry

XRD : X-Ray Diffraction

LIST of FIGURES

Page

Figure 2.1. Example of the acetabular cup (The Exceed ABT Acetabular system for hip prosthesis co–designed by Mr Smith1 in conjunction with Biomet® Inc.)	3
Figure 2.2. Thermal transformation sequence of the aluminum hydroxides.....	4
Figure 2.3. The crystal structure of alpha alumina.....	4
Figure 2.4. Flow chart for the Bayer Process.....	6
Figure 2.5. The atomic configuration of rutile.....	7
Figure 2.6. Conventional crystal structure of Al_2TiO_5 showing both the (a) distorted, edge-shared oxygen octahedra about each metal site and (b) the oxygen–metal bonds (green: Al, purple: Ti, red: O). The square structure on each image is the outline of a single unit-cell.....	14
Figure 2.7. The binary phase diagram of Al_2O_3 - TiO_2	14
Figure 2.8. The ternary phase diagram of Al_2O_3 - TiO_2 - MgO	15
Figure 2.9. Formation solid solution substituting some Al^{3+} ions by Mg^{2+} into tialite crystal. (Red:O, Green:Al, Blue: Mg, V: Void).....	16
Figure 2.10. The crystal structure of Al_2TiO_5 showing the oxygen–metal bonds after the addition of MgO (Mg^{2+} ions) as sintering aid and substituting some Al^{3+} ions (green: Al, purple: Ti, red:O, blue: Mg).....	16
Figure 2.11. The cortical or compact bone, the trabecular or spongy bone and the arrangement of carbonate hydroxyapatite and collagen in the formation of hard tissues.....	17
Figure 2.12. Crystal structure of carbonate hydroxyapatite and the powder X-ray diffraction patterns and infrared spectra of enamel, dentine and bone.....	18
Figure 2.13. Hydroxyapatite structure projected down the c-axis onto the basal plane.....	20

Figure 2.14. X-ray diffraction pattern of the Bov.HA powder
(●, HA; ▲, FA; ■, HA (OH, Cl, F rich); β, whitlockite)
(Before thermal spray coating process, bottom)
X-ray diffraction pattern of the Bov.HA after plasma spray
{▲, FA; ●, HA; ■, HA (OH, Cl, F rich); ○, CaO}
(After thermal spray coating process, above).....21

Figure 2.15. Powder flame spray system.....23

Figure 3.1. Experiment set up of our procedure.....27

Figure 3.2. Procedure of beneficiation of Seydişehir alumina;
a) alumina powder as taken (at left), b) leaching procedure
b) on heating magnetic stirrer, c) After boiling with distilled
c) water and decantation of the excess water.....28

Figure 3.3. Powders of alumina after beneficiation when drying at the
drying oven (at left) and when sintering in the furnace (at right).....28

Figure 3.4. The standard calibration samples.....30

Figure 3.5. The calibration lines of standard samples.....30

Figure 3.6. The basic ball milling process we applied for grinding and
also homogenization of the specimens.....33

Figure 3.7. Pressing procedure; (a) the uniaxial manual pressing,
(b) steel mold, (c) powder, (d), filled powder into the mold,
(e) piston in the mold, (f) mold in the pressing, (g) pressing,
(h) pressure applied onto the press (2000 psi), (i) and
j) relieving of pression (0 psi), (k) ejection of the pellet from the mold.....34

Figure 3.8.Sintered specimens of the first group of –S- type specimens,
from left to right, S1 group to S4 group.....34

Figure 3.9. Crushing and grinding of bioceramic pellets for XRD powder analysis measurements.....	35
Figure 3.10. Our process of HA flame spray coating; a) Cleaned powder filler, b) Combustion Flame Spray System, c) Oxygen tubers, d) Acetylen tube, e) Our specimens put in the order for the process, f) and g) Bond coating application (specific color and shape of the flame; White and irregular), h) and i) Bovine HA coating application (specific color and shape of the flame; Yellowish orange and long curved), j) At the end of the application, our specimens, k) Our specimens when cooled down to the room temperature.....	37
Figure 4.1. The DTA thermogram of Seydisehir alumina before beneficiation and calcination.....	38
Figure 4.2. The calibration lines of Seydisehir alumina samples.....	39
Figure 4.3. The XRD patterns of raw Seydisehir alumina and Seydisehir alumina powders after beneficiation and calcination at 1200 °C.....	40
Figure 4.4. SEM micrographs of Seydisehir alumina powders (x90 magnification); Seydisehir raw alumina powder (upleft), after 3 hours of beneficiation and after calcination at 1200 °C (downleft), after 5 hours of beneficiation and after calcination at 1200 °C for 2 hours (downright).....	41
Figure 4.5. The average particle size distribution of Seydisehir alumina powders after beneficiation and calcination before ball milling.....	42
Figure 4.6. Graphical comparison of the specimens' density (1-4; S1-4 and 5-8; L1-4).....	43

Figure 4.7. The XRD peaks of –S- type specimens.....	44
Figure 4.8. The XRD peaks of –L- type specimens.....	44
Figure 4.9. The comparison of XRD peaks of our specimens.....	45
Figure 4.10. Comparison of all the batches sintered at the same temperature (1600 °C) with the same magnification (x500, back scattering mode).....	47
Figure 4.11. Comparison of all the batches sintered at the same temperature (1600 °C) with the same magnification (x2000, back scattering mode).....	48
Figure 4.12. SEM microstructure (x5000, back scattering mode) and the related EDS analysis of L1 type specimen.....	50
Figure 4.13. SEM microstructure (x5000, back scattering mode) and the related EDS analysis of S1 specimen.....	51
Figure 4.14. SEM microstructure (x2000, back scattering mode) and the related EDS analysis of L4 specimen indicating different composition at the different places of the structure “n1” and “n2”.....	53
Figure 4.15. SEM microstructure (x2000, back scattering mode) and the related EDS analysis of S4 specimen indicating different composition at the different places of the structure “1” and “2”.....	55
Figure 4.16. Comparison of the specimens’ hardnesses (1: S1, 2:S2, 3:S3, 4:S4, 5:L1, 6:L2, 7:L3, 8:L4).....	56
Figure 4.17. Comparison of the specimens’ compressive strength. (1:S1, 2: S2, 3:S3, 4:S4, 5:L1, 6:L2, 7:L3, 8:L4).....	57
Figure 4.18. Comparison of the specimens’ hardnesses after coating (1: CS1, 2: CS2, 3:CS3, 4:CS4, 5:CL1, 6:CL2, 7:CL3, 8:CL4).....	59
Figure 4.19. Trace of diamond probe of Vickers microhardness measurement device taken on the coating’s cross-section.....	59

Figure 4.20. Stereomicroscopy (x50 at upper left and x 100 at upper right middle respectively) and SEM images (x250, back scattering mode, down) of the L1 type specimen.....	61
Figure 4.21. Stereomicroscopy (x50 at left and x 100 in the middle respectively) and SEM images (x250, back scattering mode,at right) of the L2 type specimen.....	61
Figure 4.22. Stereomicroscopy (x50 at left and x 100 in the middle respectively) and SEM images (x250, back scattering mode, at right) of the L3 type specimen.....	62
Figure 4.23. Stereomicroscopy (x50 at left and x 100 in the middle respectively) and SEM images (x250, back scattering mode, at right) of the L4 type specimen.....	62
Figure 4.24. Stereomicroscopy (x50 at left and x 100 in the middle respectively) and SEM images (x250, back scattering mode, at right) of the S1 type specimen.....	62
Figure 4.25. Stereomicroscopy (x50 at left and x 100 in the middle respectively) and SEM images (x250, back scattering mode) of the S2 type specimen.....	63
Figure 4.26. Stereomicroscopy (x50 at left and x 100 in the middle respectively) and SEM images (x250, back scattering mode) of the S3 type specimen.....	63
Figure 4.27. Stereomicroscopy (x50 at left and x 100 in the middle respectively) and SEM images (x250, back scattering mode) of the S4 type specimen.....	63

Figure 4.28. SEM microstructure (x2000, back scattering mode) and the related EDS analysis of L2 specimen indicating different composition at the different places of the structure “1” ,“2” and “3”67

Figure 4.29. SEM microstructure (x2000, back scattering mode) and the related EDS analysis of S2 specimen indicating different composition at the different places of the structure “1” ,“2” and “3”70

LIST of TABLES**Page**

Table 2.1. Chemical composition and physical property requirements of Alumina...	3
Table 2.2. The impurity content of Seydişehir alumina powders.....	5
Table 2.3. Physical properties of titanium oxide (Rutile phase).....	7
Table 2.4. The typical physical properties of aluminum titanate.....	10
Table 3.1. The standard samples' composition (weight %).....	29
Table 3.2. The standard samples' composition (mass %).....	30
Table 3.3. The powder composition of each batch in the slurry.....	32
Table 4.1. Seydisehir alumina (raw and with different leahing times) samples' composition (mass %) [51].....	39
Table 4.2. Results of Archimèdes density measurements.....	42
Table 4.3. Results of microhardness testing of the alumina-titania biocomposite....	55
Table 4.4. Results of compressive strength testing results.....	57
Table 4.5. Results of microhardness testing of the alumina-titania biocomposite coated with HA using the combustion flam spray method.....	58

1. INTRODUCTION

In recent years, humans have realized that ceramics and their composites can be used to modify or replace various parts of the body, particularly bone. Thus, the ceramics used for these purposes are classified as bioceramics [1]. In this research, it is intended to present the alumina-titania composite (here, especially the tialite phase) as the biomaterial combining with the hydroxyapatite (HA) [here, coating with HA using the thermal spray process, the flame spray (combustion flame) coating] for increasing the biocompatibility of the implant.

Another innovation of this thesis is the new method proposed that is to make the beneficiation of Seydişehir alumina, and its possible application as a potential economical biomaterial.

The aim of this thesis is to produce alumina-titania biocomposite combined with HA to use in bioceramic applications for hard tissues such as ear ossicles and bones. Alumina is a ceramic material, known as bioinert, that reinforces the implant structure. The rutile phase of titania has been reported to be bioactive. Moreover it is used as reinforcement component in bioactive composite systems. The addition and coating of calcium phosphates increase the bioactivity so decrease the time required for implant to be accepted by the host. However the price of HA powder is higher compared with the alumina's and titania's, also it is difficult to utilize the HA in load-bearing applications and if the chemical and physical stability of the implant is essential.

The ceramic composites are known to be used in applications such as protheses of tympanoplastic surgery. During literature research it is realized that it is relatively a novel area compared to implants used in hip arthroplasty. Additionally as the conventional HA implants are imported from the EU or the USA, they are considered economically inconvenient. Hence, it is expected to produce the bioceramic composite material cheaper but qualified enough to be used in applications to fulfill human and animal needs.

2. GENERAL BACKGROUND

2.1.1. Alumina

Alumina as being relatively inert ceramic maintains its physical and mechanical properties when implanted into the host tissues, and it is noted that high purity aluminum oxide has potential to be applied for total synovial joint replacements because of its bioinertness and it is still widely used in total hip prostheses because of a combination of excellent corrosion resistance, good biocompatibility, low friction, high wear resistance, and high strength providing the structural support [1,2]. The main problem of alumina is relatively low fracture toughness, which makes it prone to catastrophic failure. However, alumina lacks thermal shock resistance and has a relatively high thermal expansion coefficient of $8.7 \times 10^{-6} \text{ }^\circ\text{C}^{-1}$ [3]. In this research, high purity alumina, Al_2O_3 was obtained from bauxite or native corundum and it is prepared by calcining alumina trihydrate where the chemical composition of commercially available “pure” calcined alumina is provided in Table 2.1 [1].

When implanted *in vivo*, alumina shows the formation of a non-adherent fibrous capsule at the tissue interface, without exhibiting any chemical bonding with bone, it is considered an almost inert material. This non-adherent fibrous capsule can become quite thick depending on different factors, such as the quality of mechanical fit between implant and bone or the surface roughness of alumina, and can cause problems as loosening and clinical failure. A way to improve alumina osteointegration is to realise a coating on it using materials with a certain degree of biological activity [4].

Alumina as a bioinert ceramic can be used as in reconstruction of acetabular cavities, orbital rims, as bone plates and screws, drug delivery devices, femoral heads, middle ear ossicles, ventilation tubes components of total and partial hips, in the form of ceramic-ceramic composites, sterilization tubes, in the repair of the cardiovascular area [1]. The example of the acetabular cup (aluminum oxide based) can be seen in Fig. 2.1.



Figure 2.1. Example of the acetabular cup (The Exceed ABT Acetabular system for hip prosthesis co–designed by Mr Smith¹ in conjunction with Biomet[®] Inc.) [5].

Table 2.1. Chemical composition and physical property requirements of Alumina [1].

Chemical Composition	Composition (Weight %)
Al ₂ O ₃	99.6
SiO ₂	0.12
Fe ₂ O ₃	0.03
Na ₂ O	0.04
Property	Al₂O₃
Elastic modulus (GPa)	380
Flexural strength (GPa)	>0.4
Hardness, Mohs	9
Density (g/cm ³)	3.8-3.9
Grain size (μm)	4.0

Natural crystalline aluminum oxide or alumina (Al₂O₃) is named as corundum. The aluminas, if not heated above 1200 °C, can adsorb water vapor very fast and no equilibrium was reached for the stability. The alumina heated above 1200 °C was named alpha-alumina in 1916 by Rankin and Merwin [6]. The type or structure of each alumina and its temperature range of existence are determined by the structure of the starting or precursor hydroxide; they are different for gibbsite –the product, bayerite, nordstrandite, boehmite or diaspore.

These are called as “Transition Aluminas” and they are all synthetic. Figure 2.2 [6] presents, the most recent of the thermal transformation sequence:



From Fig. 2.2, may be concluded that all Transition Aluminas may be produced from gibbsite; this fact is one reason more for the industrial importance of the Bayer gibbsite. All Transition Aluminas are synthetic. In Fig. 2.3., the crystal structure of alpha alumina can be seen.

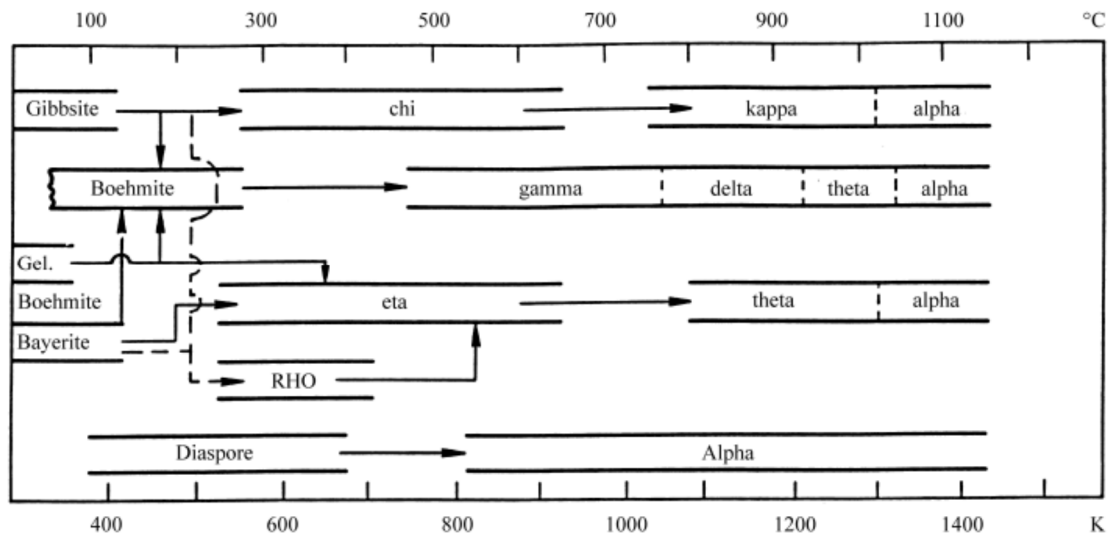


Figure 2.2. Thermal transformation sequence of the aluminum hydroxides [6].

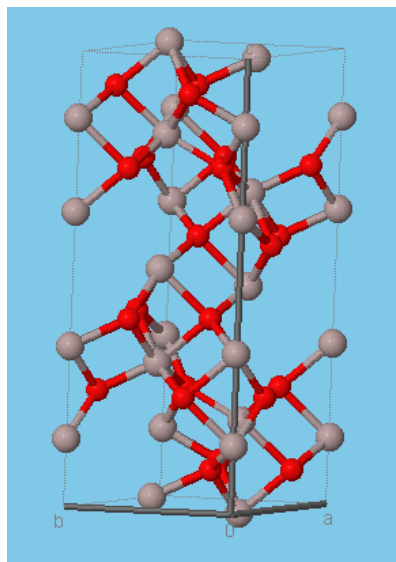


Figure 2.3. The crystal structure of alpha alumina [7].

2.1.2. Seydişehir Alumina

In ETİ/Seydişehir Alüminyum A.Ş., the metallurgical grade aluminum was produced by the Bayer Process. Seydişehir alumina powders contain metastable phases, during the process, $\text{Al}(\text{OH})_3$ is calcined at 1000 °C for dehydration of aluminum trihydroxide. Also, Bayer-processed Seydişehir alumina powders have coarse particle sizes and high Na_2O contamination. As a result, these properties make its powders non-ceramic grade [8]. Therefore a further beneficiation procedure is needed for upgrading. According to the study of Tambaş et al. [8], Seydişehir alumina powders have broad range of particle size distribution from submicron to higher than 125 μm . Chemical analysis shows that these aluminas have high soda contamination of about 0.3 percent. Also XRD analysis shows that Bayer-processed (for the flow chart of Bayer Process, see Fig. 2.4 [9]) Seydişehir alumina powders contain both transition and alpha phases. Tambaş proposed a procedure composed of calcination, washing, grinding (with different techniques). Following calcination, XRD results show that all transition phases are converted to corundum at 1200 °C. With the help of washing (using distilled water), Na_2O content of Bayer processed Seydişehir alumina powders is reduced. Chemical analysis shows that Na_2O content of aluminas washed in cold water is 0.11 percent. The impurity composition of Seydişehir alumina powders before the beneficiation process given in his study is presented in Table 2.2.

Table 2.2. The impurity content of Seydişehir alumina powders [8].

Impurity	Weight Percentage (wt %)
C	0.07
S	0.46
Na_2O	0.32
MgO	0.30
CaO	< 0.001
SiO_2	0.58
Fe_2O_3	0.17

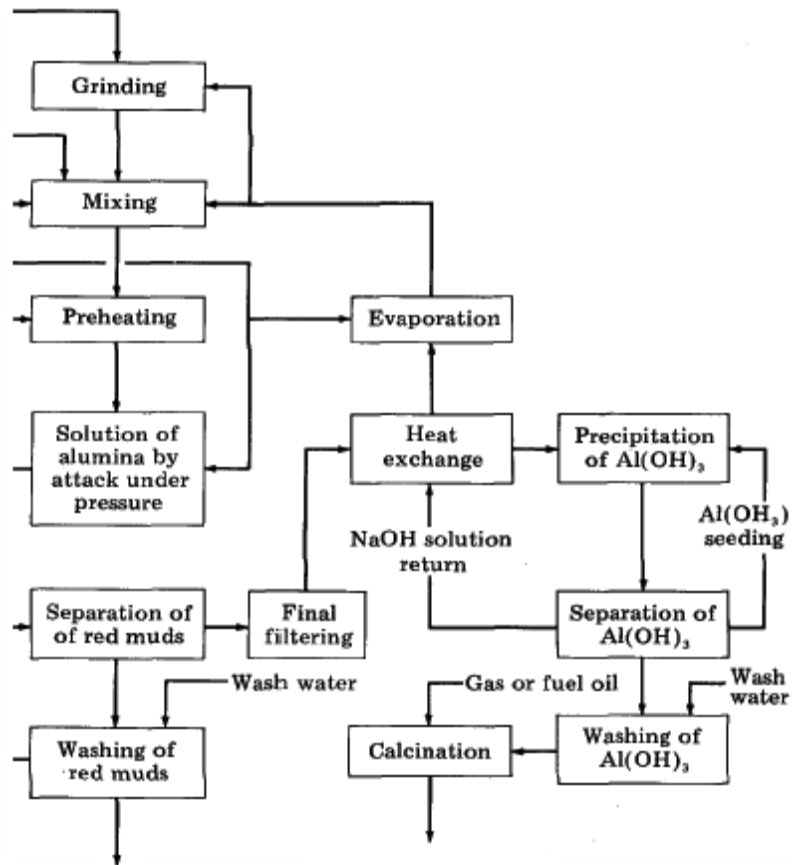


Figure 2.4. Flow chart for the Bayer Process [9].

2.2. Titania

TiO₂, having a high refractive index and low visible absorption, renders it the most important white pigment in the paint, plastic and paper industries. Furthermore, titania and its composite mixtures with a second oxide are used in heterogeneous catalysis as a photocatalyst, in solar cells for the production of hydrogen and electric energy, as gas sensor, as white pigment (e.g. in paints and cosmetic products), as a corrosion protective coating, in ceramics and electric devices such as varistors, in self cleaning and wetting applications, as interface coating and optical devices and advanced ceramics [10,11,12]. The rutile phase of titanium dioxide is bioactive. On the surface of bioactive materials when implanted *in vivo* or immersed in simulated body fluids, a bone-like apatite layer forms. The tendency of titania to adsorb water at the surface results in the formation of titanium hydroxide groups and the basic Ti-OH groups induce apatite nucleation and crystallization. This apatite layer makes chemical bonds with the bioactive surface acting as an intermediate layer between new bone and implant [13,14,15].

There are three major different structures of titanium dioxide,; rutile (tetragonal; $a=b=4.584 \text{ \AA}$, $c= 2.953 \text{ \AA}$), anatase (tetragonal; $a=b=3.782 \text{ \AA}$, $c= 9.502 \text{ \AA}$) and brookite (rhombohedral; $a=5.436 \text{ \AA}$, $b=9.166 \text{ \AA}$, $c= 5.135 \text{ \AA}$) (See, Fig. 2.5. the bulk structure of rutile) [11]. The brookite phase isn't generally described in most publications and the major phases of TiO_2 can be obtained according to the conditions during synthesis, for example, at room temperature, hydrolysis of Ti^{4+} in pure water forms the anatase as major phase whereas in the presence of HCl, the major phase is the rutile. Also when once anatase is formed, it can be transformed into rutile and the rate of this transformation is a function of preparation conditions [16]. In Table 2.3, you can see the some physical properties of titanium dioxide, rutile phase are provided.

Table 2.3. Physical properties of titanium oxide (Rutile phase) [11].

Physical Property	TiO_2 (Rutile)
Density	4,24 g/cm^3
Melting point (°C)	1870
Boiling point (°C)	2927
Linear coefficient of thermal expansion ($\alpha \times 10^{-6}$, $^{\circ}\text{C}^{-1}$) (Temperature; 0-500 °C)	8.19
Modulus of normal elasticity, E (GPa) (Density; 4,25 g/cm^3)	284.2
Hardness (Mohs)	5.0-6.5

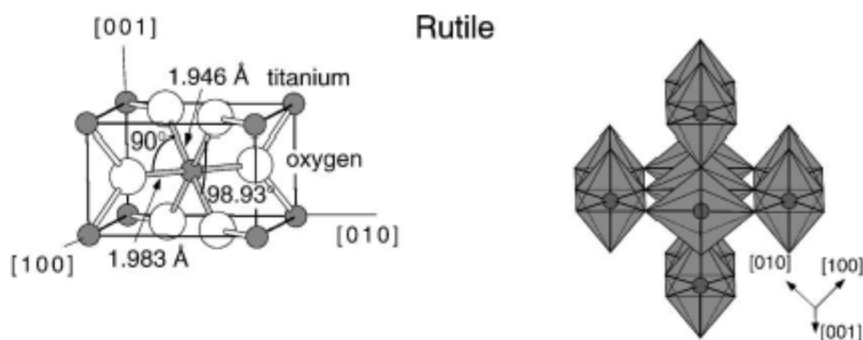


Figure 2.5. The atomic configuration of rutile [11].

2.3. Aluminum Titanate

Aluminum titanate ceramics (Al_2TiO_5) are synthetic materials used mainly as refractories in aluminum alloy casting systems due to their thermal shock resistance and better non wettability compared to molten aluminum alloys, as crucibles, launders, pouring spouts, ladles, plugs. Aluminum titanate is also used in the automotive industry as an insulating liner for exhaust manifolds where there is a need to minimise heat loss in advance of a turbocharger. In this application the metal exhaust manifold is cast around the shaped aluminium titanate liner. The thermal expansion mismatch between the steel manifold and the aluminium titanate during cooling maintains the ceramic in compression thereby overcoming the problems of its low strength. They have a potential for possible structural applications owing to their high melting, good chemical resistance, low thermal conductivity and excellent thermal shock resistance [17,18]. But the thermal expansion of aluminium titanate is highly anisotropic ($\alpha_{a25-1000^\circ\text{C}} = 10.9 \times 10^{-6} \text{ }^\circ\text{C}^{-1}$, $\alpha_{b25-1000^\circ\text{C}} = 20.5 \times 10^{-6} \text{ }^\circ\text{C}^{-1}$, $\alpha_{c25-1000^\circ\text{C}} = -2.7 \times 10^{-6} \text{ }^\circ\text{C}^{-1}$) [18]. The further properties of aluminum titanate can be seen in Table 2.4. [18]. In addition to these properties the service life of aluminum titanate products is longer than competing materials such as calcium silicate and fused silica [18].

Tialite has an orthorhombic structure with the following lattice parameters: $a = 3.591$, $b = 9.429$ and $c = 9.636 \text{ \AA}$. Aluminum titanate (AT) has two allotropic forms such as α and β where β aluminum titanate is the low temperature stable phase. AT can be formed via solid-state reaction between alumina and titania above the eutectoid temperature 1280°C : This is also its first range of stability. This solid-state reaction has two stages: At the first reaction stage, the nucleation of AT cells takes place at 1345°C , then the elimination of Al_2O_3 and TiO_2 dispersoids, which were previously trapped, occurs through a diffusion-controlled mechanism and takes place at 1385°C . AT can be dissociated to alumina and rutile in the temperature range $750\text{-}1280^\circ\text{C}$ decreasing also its mechanical strength. In order to overcome such dissociation, the stabilizers (dopants) such as Fe_2O_3 , MgO , La_2O_3 , SnO_2 or SiO_2 or suitable second-phase materials like Al_2O_3 , ZrO_2 and mullite are added into the batches. Its second range of stability is from 1280°C up to 1820°C . AT is highly stable up to its melting point ($T_m = 1860^\circ\text{C}$). Formation of tialite by individual oxides takes place at temperatures over 1200°C due to solid-state reaction of the components in crystalline state but its decomposition phenomenon to Al_2O_3 and TiO_2

(Rutile) is a serious limitation to the widespread utilization of aluminum titanate based materials, also the microcracks developed especially at the grain-boundaries translating into poor mechanical strength during cooling from the sintering temperature to room temperature due to its thermal expansion behavior or the degree of thermal anisotropy is another inherent problem generally encountered during the production of the tialite [19,20,21,22,23,24]. These problems and decompositions, in fact, are originated from the ability of Al atoms to migrate away from their lattice sites, leading to structural dissolution to rutile and corundum [24]. The aluminum titanate structure can also be obtained at low temperatures over 600 °C by nonhydrolytic synthesis, at 700 °C using acid-catalyzed solutions of aluminum and titanium alkoxides (β - Al_2TiO_5 films) and around 800 °C via the synthesis with alkoxides stabilized with acetylacetonone [21]. Other synthesis methods are; sol-gel, reaction sintering of metal alkoxides, hydrothermal processing, combustion synthesis, plasma flame oxidation, powder electrofusion or infiltration [24,25]. In general, almost all families of aluminium titanate ceramic materials have been developed on compositions containing equimolar ratios of Al_2O_3 and TiO_2 . Small amounts of various additives – stabilizers mentioned above- have also been used with the aim of improving the thermodynamic stability at intermediate temperatures. In some researches, the effects of deviations from the equimolar composition of aluminium titanate on the material properties that are the most relevant for the industrial applications of AT ceramics were investigated. When alumina/titania excess increases, especially an alumina excess, can accelerate the decomposition of AT causing internal stresses accumulated and preserved within these materials. The explanation of this phenomenon by some authors was the action of the excess alumina as nucleation centres for the reaction of decomposition. Higher sintering temperatures and longer dwell times yielded thermodynamically more stable AT materials. [26]. In some point of views, the reversibility of the phase decomposition process was unclear. If the process was reversible, the decomposed aluminum titanate might undergo self recovery (reformation) when reheated to elevated temperature (i.e. > 1300 °C) as the “self healing” phenomenon was observed in the cracks of Al_2TiO_5 at higher temperatures. It was discovered that the process of decomposition in metastable Al_2TiO_5 is reversible and that reformation can occur readily when decomposed Al_2TiO_5 is re-heated above 1300 °C. It is further shown that decomposition of Al_2TiO_5 during cooling below ~1200 °C is governed by the

temperature-dependent atomic diffusion rates and as the temperature rises beyond 1300 °C, reformation or recovery dominates and occurs rapidly to form Al₂TiO₅ because of very high atomic diffusion rates [27].

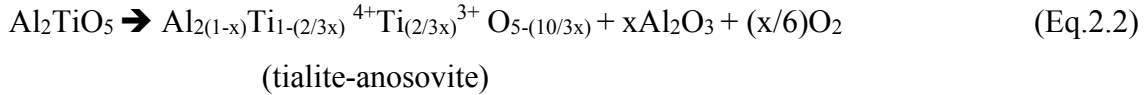
Aluminum titanate is a member of the pseudobrookite family of compounds with the general formula, A₂BO₅ crystallizing in the orthorhombic symmetry with space group Bbmm [25,28]. In an other study, it was mentioned that [29] Al₂TiO₅ crystallised as an orthorhombic unit-cell in the Cmc₂m space-group (using a c-face centred unit-cell) with lattice parameters of **a = 3.557 Å**, **b = 9.436 Å**, and **c = 9.648 Å**. Aluminum titanate exhibits a structure, each Al³⁺ or Ti⁴⁺ cation surrounded by 6 oxygen ions forming distorted oxygen octahedra. These AlO₆ or TiO₆ octahedra (001) oriented double chains weakly bonded by shared edge. This structure causes the strong thermal anisotropy creating a complicated system of localised internal stresses during cooling from the firing temperature resulting in the intrinsic fracture strength of the material, then the severe microcracking. These microcracks contribute to the low thermal conductivity and the excellent thermal shock resistance of the material [28,29]. According to the article [25] , the structure of Al₂TiO₅ consists of distorted edge-shared oxygen [MeO₆] octahedra surrounding the metal sites, M1 and M2 which have a coordination number of 6. The metal atoms exist on fourfold (4c) symmetry sites and the oxygen atoms on eightfold (8f) symmetry sites. The crystal structure of Al₂TiO₅ is shown in Fig. 2.5.

Table 2.4. The typical physical properties of aluminum titanate [18].

Property	Aluminum Titanate
Density	3-3.4 g/cm ³
Modulus of Rupture at room temperature	30MPa
Young's modulus	20GPa
Thermal expansion	0 -1 x10 ⁻⁶ K ⁻¹ (20-600 °C) 1 -2 x10 ⁻⁶ K ⁻¹ (600-1000 °C)
Thermal conductivity (RT-1000°C)	< 2W.m.K ⁻¹
Maximum service temperature	1000 °C continuous 1100 °C intermittent

By a rule of thumb, finer particle sizes of ceramic materials at higher sintering temperatures will cause much more densified and much more tough material due to the final grain size of the sintered material. It was mentioned in the article [25], that there was a critical grain size below which the energy available in the system is insufficient to create microcracks. That critical grain size is a material-related property and is inversely proportional to the square of the degree of thermal expansion anisotropy. Based on the fact that there is no stress relaxation occurred below a sintering temperature of 1500 °C, they proposed that the critical grain size for aluminium titanate is not a unique value but varies inversely with the sintering temperature below 1500°C. Therefore, larger critical grain size and less microcracking are the results of lower sintering temperatures. So it can be derived from these data that in the anisotropic materials such as aluminum titanate, the degree of the thermal expansion anisotropy, reason of the microcracks inside the microstructure of the material, also a crystal structure dependent property affects the final mechanical properties of the material more than the initial particle size of the powders and as much as the critical grain size of the material, related to the initial particle size and sintering temperature of the material especially at the sintering temperatures below 1500°C. Indeed, the morphology of microcracks in AT has a remarkable temperature dependence. The degree of these microcracks and the stress distribution in the matrix have a direct influence on the microstructure of the AT ceramics, affecting strongly their mechanical properties. As the temperature increases up to the actual casting temperature of 702 °C, the microcracks at the grain boundaries close up, and the AT grains are bonded together by the glassy phase added as sintering aid [17]. According to the article [17] above 502 °C, the closed crack surfaces were self-healing and causing bonding of AT grains by the glass phase in the matrix. Accumulated microcracking were due to the thermal expansion anisotropy of the individual AT crystals, which gives rise to stresses on a microscopic scale during cooling. These localized internal stresses constitute the driving force for microcracking. Clearly, the difference in the composition of the glass phase has a great effect on the contraction and expansion of AT crystals. The experimental results showed that the fracture strength of AT ceramics increases with increasing process temperature due to a decrease in the number of microcracks along the AT grain boundaries during bonding of the AT particles via the glass phase at higher temperatures. The fracture toughness increased with increasing temperature [17].

It was mentioned in the article [29] the decomposition of tialite was expected to be very fragile to the aging (annealing) environment or atmosphere, because Ti^{4+} is progressively reduced to Ti^{3+} if the partial pressure of oxygen is decreased. Duran et al. noted that under a nitrogen/oxygen gas mixed atmosphere, decomposition of tialite is increasing at 975 °C as the following reaction with the formation of tialite–anosovite solid solution.

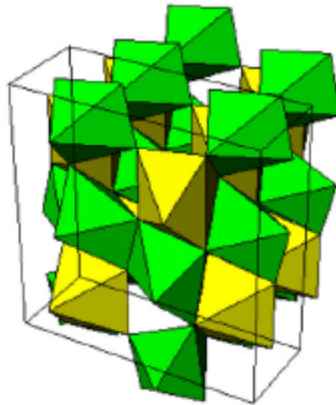


Similarly, Low et al. showed that the decomposition rate of Al_2TiO_5 at 1100 °C is significantly increased in vacuum (10^{-4} Torr) where >90% of tialite decomposed after only 4 h soaking time comparing to less than 10% in air atmosphere and the thermal stability of tialite was improved in an atmosphere of 100% oxygen when compared to ageing in air. [29, 30]. In the study of Low et al. [29], even though the titanium ions in titania is very susceptible to the non-stoichiometry in the atmosphere with decreased content of oxygen, the exact mechanism of enhanced phase decomposition in argon or inert atmosphere remains unclear. This information is especially valuable when studying between 1150-1300 °C, over 1300 °C, the thermal decomposition is arrested and the phase stability is restored. Also, according to the same article; the use of either argon or oxygen atmosphere did not appear to alter or affect the temperature range of thermal decomposition. It can be derived from the study made in the article [30], in the reducing atmospheres, working with non equimolar alumina-titania compositions, after fast cooling, any aluminum titanate structure can't be obtained due to lack of oxygen and the dissociation problem of aluminum titanate between the temperature range 1280-700 °C. The conventional crystal structure of Al_2TiO_5 can be seen in Fig.2.6.

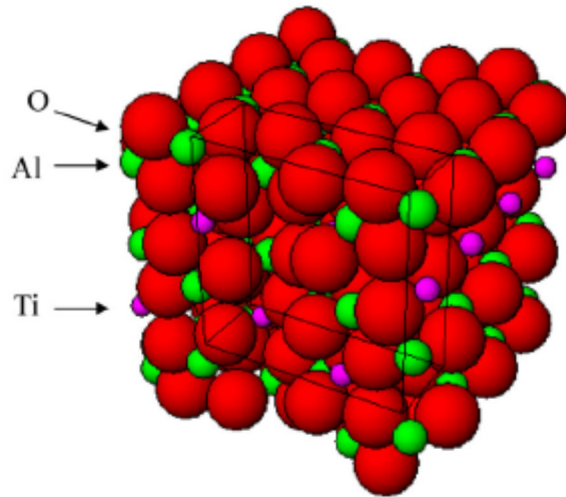
In several studies made on the influence of MgO and Fe_2O_3 additives [31,32]; it was found that;

1. Formation of AT for both MgO-doped and Fe_2O_3 -doped systems (up to 5% (n/n) substitution limit) involves a transition phase and these crystalline phases remain stable between 1000 and 1400 °C.
2. Composition of the transitional phase is $Mg_{0.3}Al_{1.4}Ti_{1.3}O_5$ for the system with MgO additive.

3. In the case of the system with Fe_2O_3 additive, composition of the transitional phase is unknown, but the measured and calculated typical plane d-spacing values are indicated.
4. Addition of 2.5 wt.% Fe_2O_3 to a fine mixture of aluminum hydrate and rutile resulted in decreasing the tialite formation temperature from temperatures over 1280 °C down to 1150 °C. So the addition of Fe_2O_3 helps decreasing formation of the aluminum titanate phase.
5. The moderately good microstructure of Al_2TiO_5 was improved with the addition of Fe_2O_3 up to 7.5% so that tialite grains became larger in size while pores were diminished. Thus the addition of Fe_2O_3 acts as a sintering add, helping decreasing of pore sizes of the aluminum titanate microstructure.
6. It was confirmed by X-ray diffraction and lattice parameter investigations that both Mg^{2+} and Fe^{3+} ions build in the crystal lattice of Al_2TiO_5 forming solid solution series. Respectively, you can see the binary phase diagram of Al_2O_3 - TiO_2 in Fig. 2.7 [33] and the ternary phase diagram of Al_2O_3 - TiO_2 - MgO in Fig. 2.8 [34]. According to the ternary phase diagram, our limitation of MgO addition is approximately 5,5 wt. %. Mg^{2+} ions carried by MgO into tialite crystal formed solid solution substituting some Al^{3+} ions (See Fig.2.9 and 2.10).



(a)



(b)

Figure 2.6. Conventional crystal structure of Al_2TiO_5 showing both the (a) distorted, edge-shared oxygen octahedra about each metal site and (b) the oxygen–metal bonds (green: Al, purple: Ti, red: O). The square structure on each image is the outline of a single unit-cell [28].

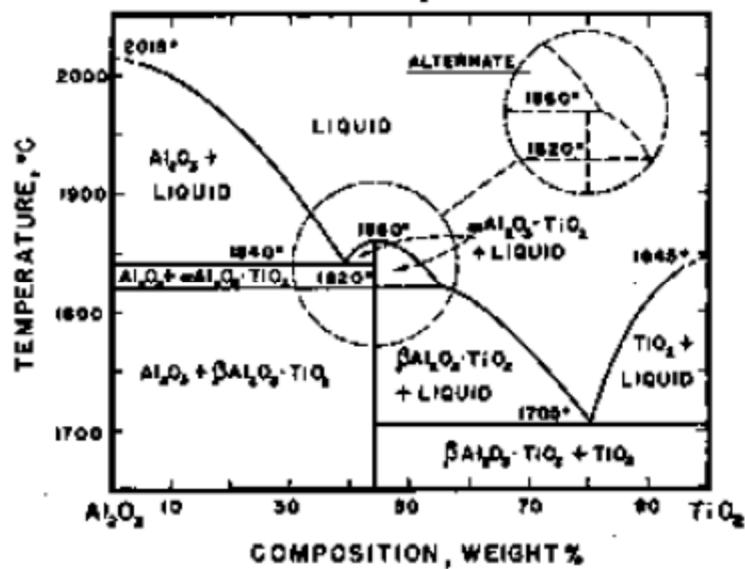


Figure 2.7. The binary phase diagram of Al_2O_3 - TiO_2 [33].

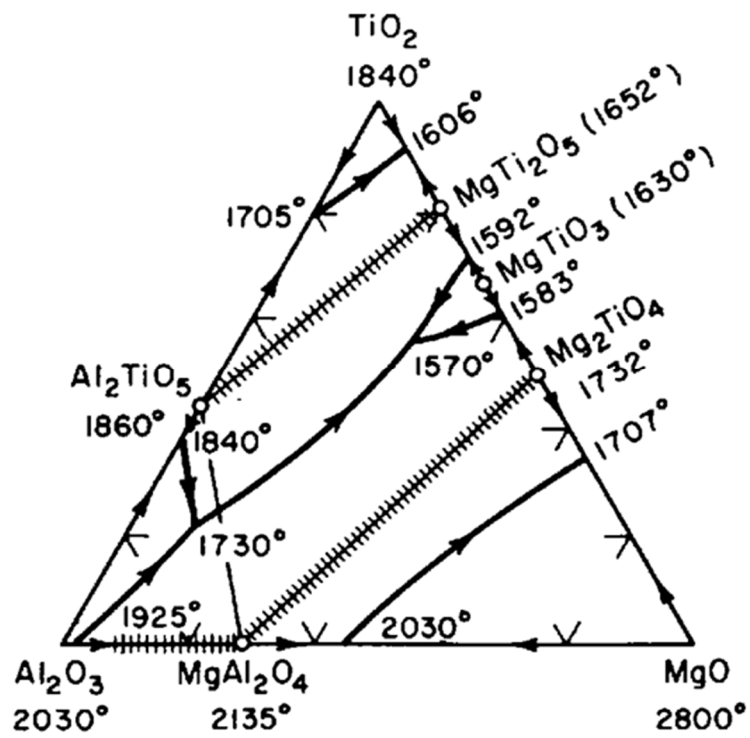
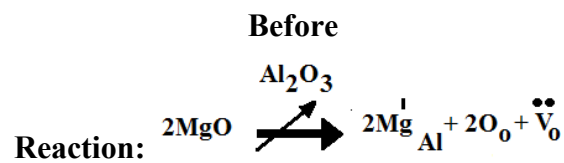
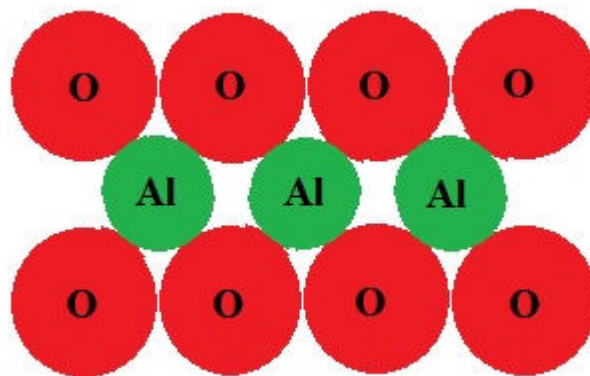
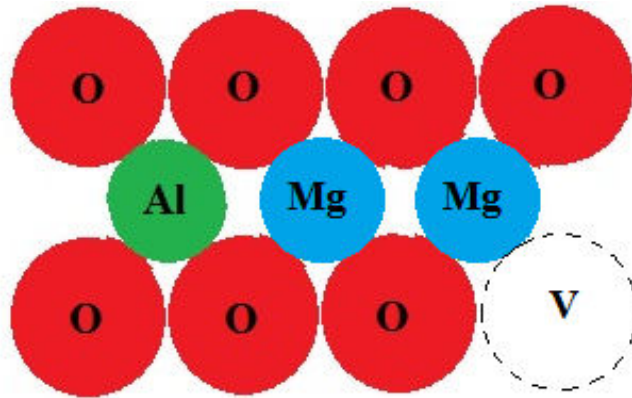


Figure 2.8. The ternary phase diagram of Al₂O₃-TiO₂-MgO [34].





After

Figure 2.9. Formation solid solution substituting some Al^{3+} ions by Mg^{2+} into tialite crystal. (Red: O, Green: Al, Blue: Mg, V: Void).

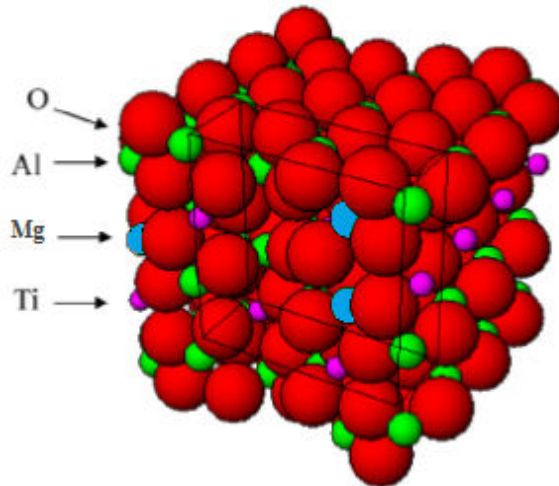


Figure 2.10. The crystal structure of Al_2TiO_5 showing the oxygen–metal bonds after the addition of MgO (Mg^{2+} ions) as sintering aid and substituting some Al^{3+} ions (green: Al, purple: Ti, red: O, blue: Mg).

2.4. Hydroxyapatite

Calcium phosphate group is the largest inorganic part of hard tissues in bones and dentine material in vertebrate animals [35]. Calcium phosphate biomaterials constitute the bioactive ceramics; being capable of bonding with living tissues of bones; i.e. being able to interact chemically with their environment such as an artificial solution chosen to perform *in vitro* assays or the physiological body fluids during *in vivo* assays [36]. There are several methods to synthesize HA powders including wet-chemical method in aqueous solutions, sol-gel method [37], gel casting method [38], hydrothermal method, thermal deposition, conversion of coastal corals, and continuous precipitation [35,36]. Especially porous HA implants served as bone grafts (substitutes) into clinical studies have several benefits such as their light weights and the relatively short time of the histological response [35]. In Fig. 2.11. the cortical or compact bone can be seen, the trabecular or spongy bone and the arrangement of carbonate hydroxyapatite and collagen in the formation of hard tissues [36].

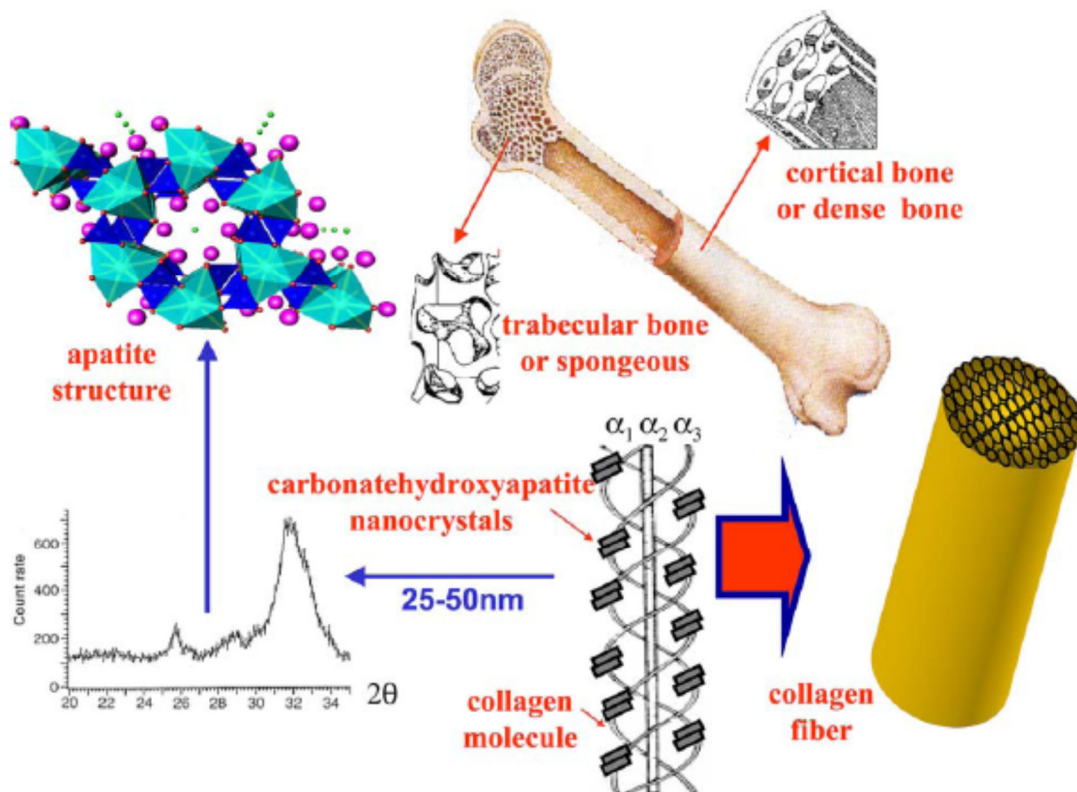


Figure 2.11. The cortical or compact bone, the trabecular or spongy bone and the arrangement of carbonate hydroxyapatite and collagen in the formation of hard tissues [36].

In Fig. 2.12., the crystal structure of carbonate hydroxyapatite can be seen and the powder X-ray diffraction patterns and infrared spectra of enamel, dentine and bone [36].

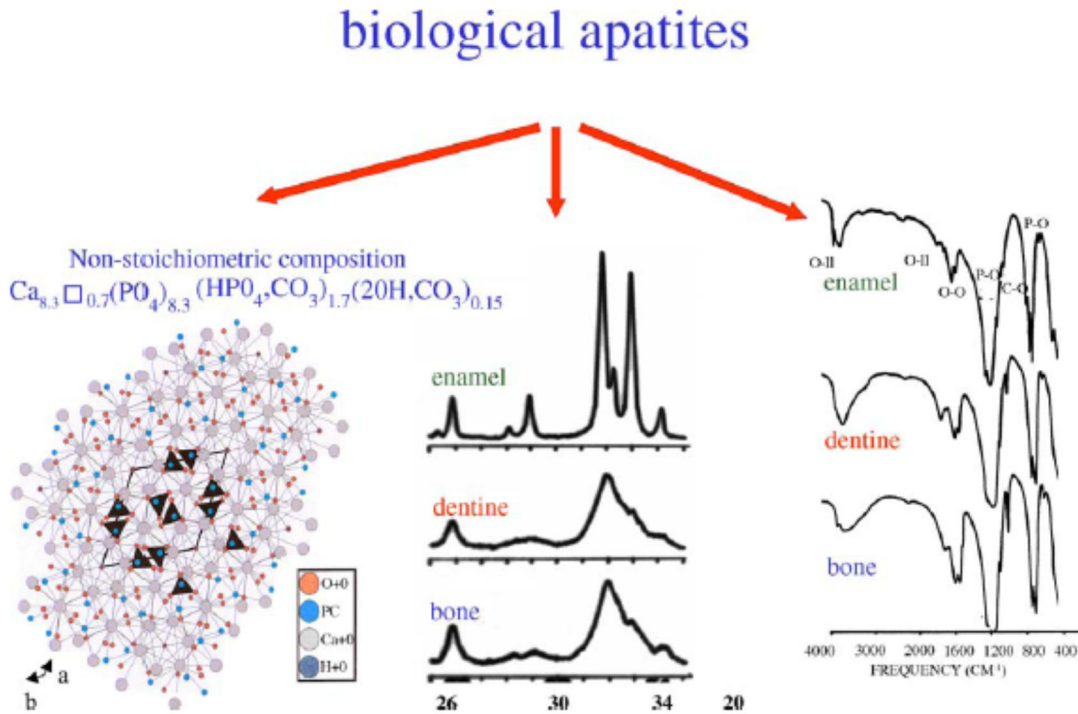


Figure 2.12. Crystal structure of carbonate hydroxyapatite and the powder X-ray diffraction patterns and infrared spectra of enamel, dentine and bone [36].

Lattice parameters of hydroxyapatite ($a = 0.95$ nm and $c = 0.68$ nm), and its symmetry (hexagonal, S.G. $P6_3/m$) most likely its unit cell will be arranged along the c -axis. The crystal structure of the hydroxyapatite can be seen in Fig. 2.13 [1, 36]. But the hydroxyapatite is particularly recognized amongst other calcium phosphates by its Ca/P ratio (1.67; the value of stoichiometric hydroxyapatite). There is a close relation between the Ca/P ratio, acidity and solubility; the lower the Ca/P ratio is, the larger are the acidity and solubility of the mixture [36]. Upon 1050 °C, the hydroxyapatite is converted to β -tricalcium phosphate (β -TCP; the Ca/P ratio=1,50) and mostly depending on the synthesis conditions, coexist in distinct proportions at the same microstructure [36].

Based on increasing the mechanical properties of HA, several composites with bioinert and bioactive ceramics, metal particles or polymers were suggested in previous studies [39,40,41,42].

In general, the utilization of bulk HA components has been restricted by its low flexural strength and low fracture toughness and the final mechanical properties of HA are dependent on the sintering quality [43]. Thus, the use of HA applying as a coating material by several different methods on several different substrates was widely spread such as sol-gel coatings, including dip coating, plasma spray coating, HA blasting, pulsed laser deposition, biomimetic coatings using electrodeposition. In addition, co-precipitation of CaP, biomimetically functionalized coatings, and even ionic implantation [44, 45, 46,47] are under application. HA is utilized having promising results when coated on titanium implants [46]. During the plasma spray processes, the heat causes changes in the composition of the HA ceramic. As results; the different phases of CaP beside HA such as , amorphous calcium phosphates (ACP) and small amounts of α - and β -TCP, tetracalcium phosphate (TTCP) and sometimes, calcium oxide formed [46]. In non loading conditions such as surface coatings, several studies showed, not only HA but its dissociation products like tricalcium phosphate are highly bioactive and resorbable providing an early mechanical implant fixation and by this point of view, it is more stable compared to HA. Biphasic calcium phosphates, mixtures of HA with its dissociation products, also exhibit improved implantation results. Therefore, even subproducts of HA coatings are useful for biocompatibility of the implant.

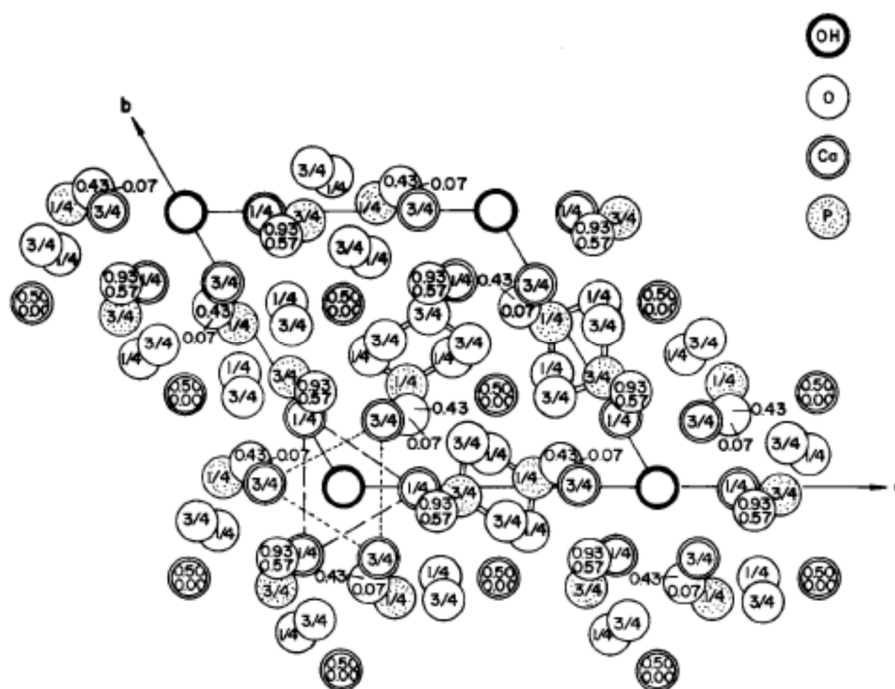


Figure 2.13. Hydroxyapatite structure projected down the c-axis onto the basal plane [1].

In this study, bovine HA [48] was chosen as HA source mainly due to its wide potential to be used a cheaper HA source for plasma spray coating applications in the future.

Bov.HA powders were produced the HA powders from natural bovine femurs, then were dissolved with NaOH treatment. Before sintering, the deproteinization process was carried out with reagent grade NaOH. Demineralized water would be used at each step of the procedure. Deproteinized Bov.HA was calcined at 850 °C for 4 h, based on the procedure of a previous studies, so no prions or any disease-causing agents can survive. Bov.HA was grinded very fast for 30 s with a mechanical grinder. It was noticed that for this Bov.HA only the powder fraction between 150 and 200 microns had enough flowability for the thermal spray processes such plasma spray coating or flame spray coating. Coarser powder would block the feeder [48]. The XRD analysis of the Bov.HA powders before and after thermal spray processes are shown in Fig. 2.14.

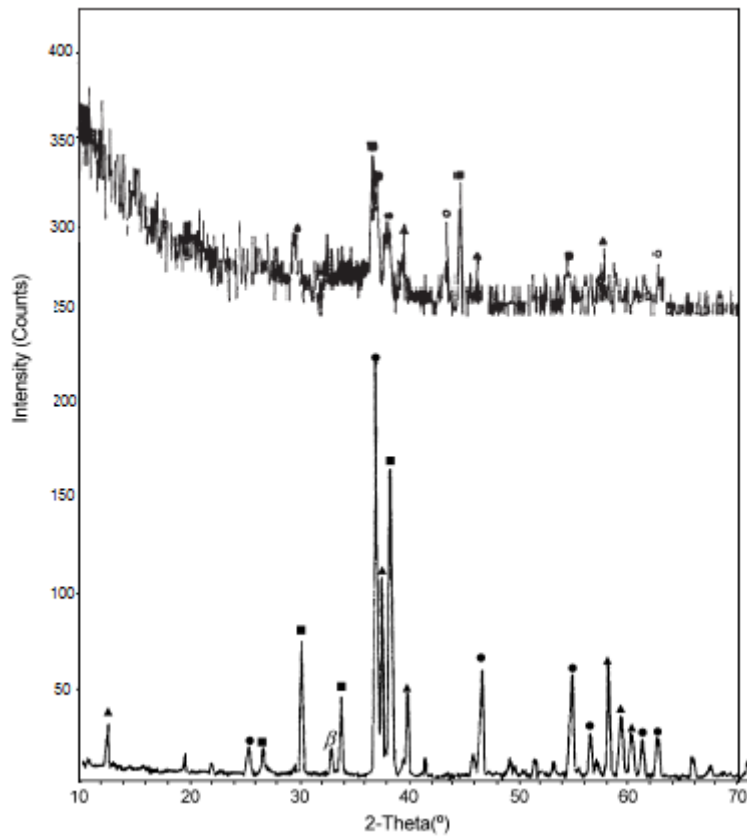


Figure 2.14. X-ray diffraction pattern of the Bov.HA powder (●, HA; ▲, FA; ■, HA (OH, Cl, F rich); β, whitlockite) (Before thermal spray coating process, bottom). X-ray diffraction pattern of the Bov.HA after plasma spray {▲, FA; ●, HA; ■, HA (OH, Cl, F rich); ○, CaO} (After thermal spray coating process, above) [48].

In this research, it is thought to produce a promising material which may find applications as middle ear implants in future. So during this research, it is realized that hydroxyapatite has broad otological application in reconstruction of the auditory ossicular chain. In obliteration of the mastoid cavity due to its biocompatibility, mechanical and chemical properties [49]. It shows low levels of inflammation and fibrosis, on this basis, new bone formation and satisfactory integration of hydroxyapatite-bone formation may be seen in the future studies.

2.5. Thermal Spray Coating Processes

Amongst all spray coating processes, except HVOF (High Fuel Oxygen Fuel) process, ceramic powder material can be applied, even in rod forms, on the substrate material. The choice of coating procedure depends on the powder type (composition, particle size, melting temperature of the powder), substrate material -for example the coating of molybdenum on copper containing alloys is not very successful-, application area of the material and its physical and chemical properties [50]. The adhesion strength of the coating is also dependent on the choice of thermal spray applications, powder, substrate and “bond coat material” used between two different material layers of material to increase the adhesion between layer, off course the adhesion strength over all.

In flame powder coating process, powdered feedstock is aspirated into the oxyfuel flame, melted, and carried by the flame and air jets to the workpiece. Particle speed is relatively low (<100 m/s), and bond strength of the deposits is generally lower than the higher velocity processes. Porosity can be high and cohesive strength is also generally lower [49]. Flame spray uses the chemical energy of combusting fuel gases to generate heat.

Oxyacetylene torches are the most common, using acetylene as the main fuel in combination with oxygen to generate the highest combustion temperatures. Powders are introduced axially through the rear of the nozzle into the flame at the nozzle exit. The feedstock materials are melted and the particles/droplets accelerated toward the substrate surface by the expanding gas flow and air jets. A typical powder flame spray gun is shown in Fig. 2.15 [50]. In conventional flame spray torches, a jet of fuel and oxygen is combusted at the front of the torch, external to the nozzle. Nozzles are used to shape the spray pattern. Air caps are added to wire- and rod-fed torches, producing a concentrated air jet to atomize the molten wire or rod tip. In flame spray processes, fuel/oxygen ratio and total gas flow rates are adjusted to produce the desired thermal output. Optional air jets, downstream of the combustion zone, may further adjust the thermal profile of the flame. Jet gas speeds typically are below 100 m/s (330 ft/s), generating particle speeds up to 80 m/s (260 ft/s) before impact. Externally combusted, or open-flame, jet temperatures are generally above 2600 °C (4700 °F) and are controlled by the combustion temperatures of the fuel/oxygen mixtures and the mixing patterns of the combustion gases with the surrounding air. The temperature curves for fuel gases are parabolic in shape and centered roughly around the stoichiometric ratio with oxygen. Adjusting the fuel/oxygen ratio,

either side of stoichiometry, will cool the flame. The reason behind the adjustment is to make the flame either oxidizing or reducing, as the feedstock material and application dictate. Flames are set to be reducing (fuel-rich) for most metal spraying in order to minimize oxidation. Flame spray processes typically yield coating densities ranging from 85 to 98%, depending on the coating material and particular technique [50].

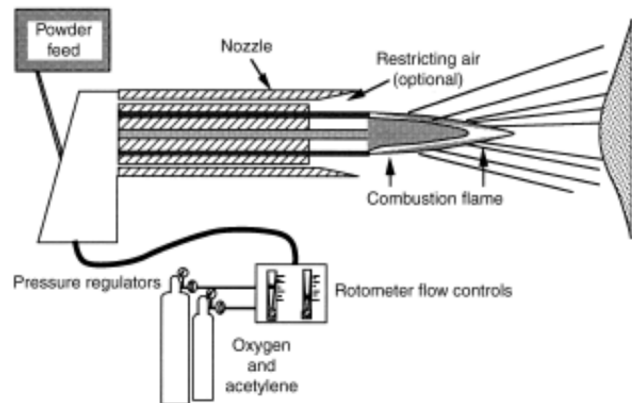


Figure 2.15. Powder flame spray system [50].

II.6. Instruments Used in this Research

This research study has three main aspects;

- 1-Beneficiation of Seydişehir Alumina
- 2-Production of Alumina-Titania Biocomposite (containing the tialite phase)
- 3-Coating with HA the alumina-titania substrate using flame spray process

So the instruments used in each process of the processes in this study are as;

- 1- Beneficiation of Seydişehir Alumina; Naberthem furnace (16/8, High Temperature Furnace), Netzsch STA 409CD (with DTA-TG holder), Malvern Laser Particle Sizer Hydro MU2000, SEM (Jeol JSM-5910 LV –Low Vacuum Scanning-) and EDS (Oxford Inca Energy 200), XRD (Rigaku vertical diffractometer), XRF (Rigaku mini X-ray fluorescence spectrometer)
- 2- Production of Alumina-Titania Biocomposite; mechanical ball milling instrument (roller), the uniaxial manuel press, SEM (Jeol JSM-5910 LV –Low Vacuum Scanning-) and EDS (Oxford Inca Energy 200), XRD, the universal mechanical

testing instrument with compression testing attachment (Devotrans), the microhardness testing instrument (Shimadzu, Japan).

- 3- Coating with HA the alumina-titania substrate using flame spray process; Sulzer-Metco Combustion Flame Spray (6P-II Gun), SEM (Jeol JSM-5910 LV –Low Vacuum Scanning-) & EDS (Oxford Inca Energy 200), the microhardness testing instrument the microhardness testing instrument (Shimadzu, Japan).

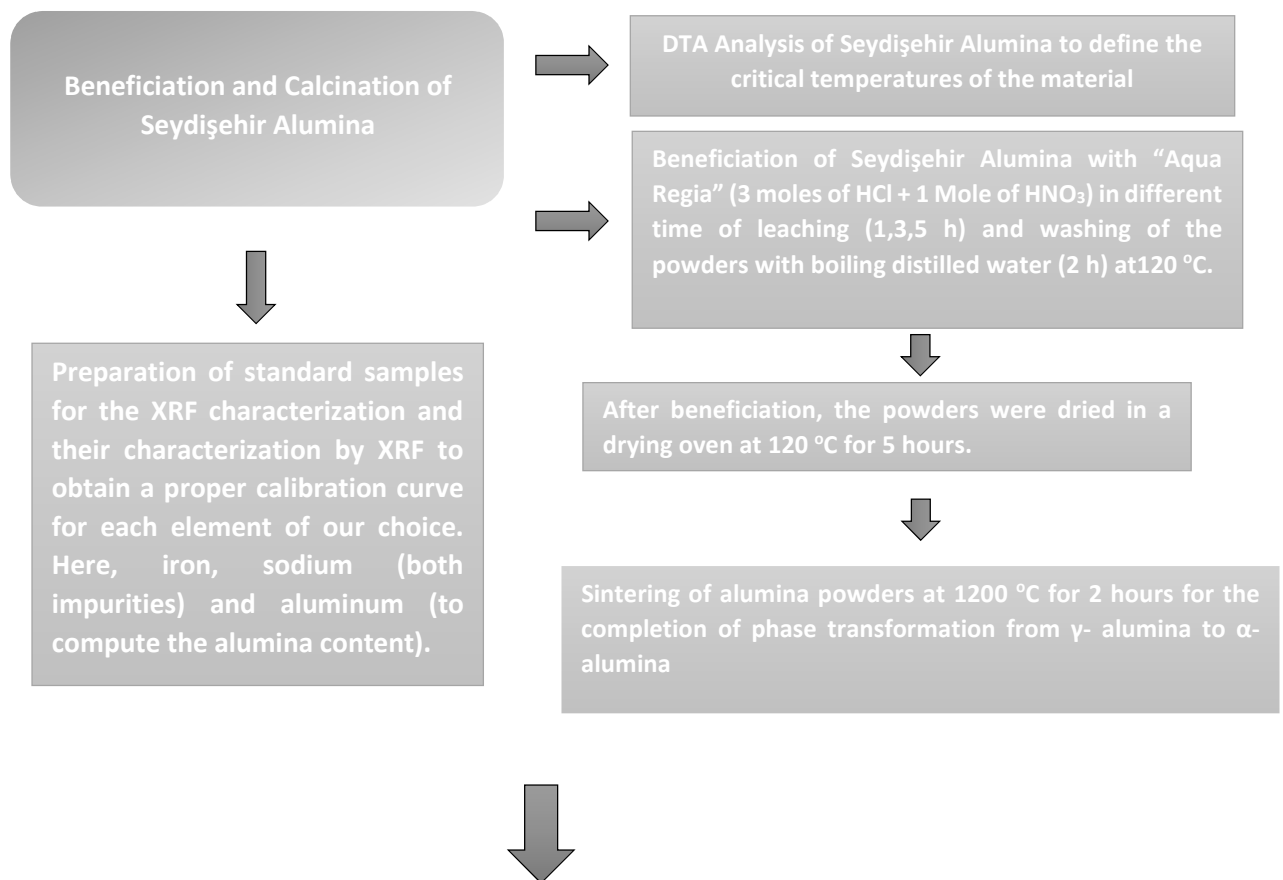
3. MATERIAL and METHOD

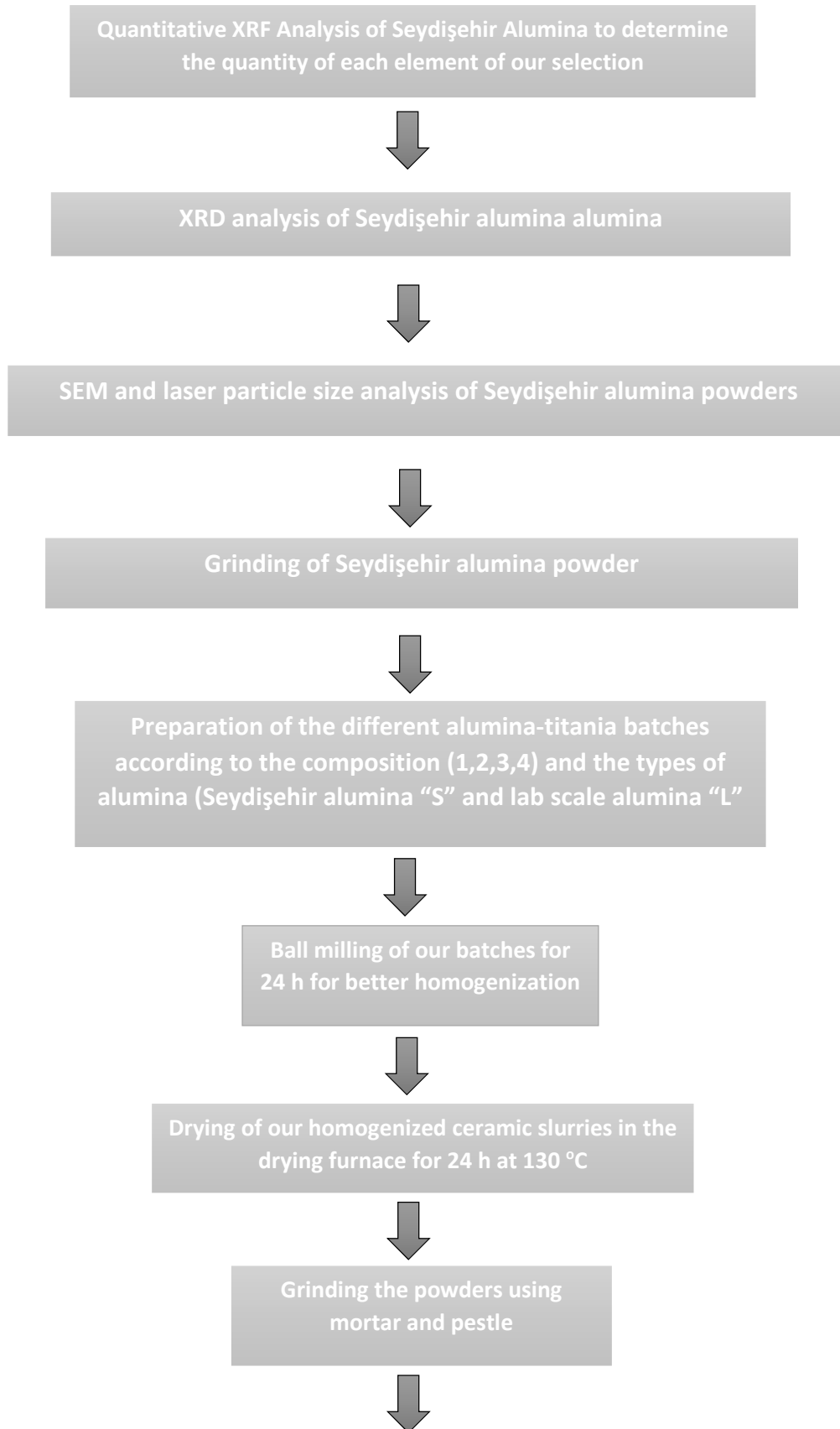
3.1. Experimental Setup

3.1.1. Materials Used in the Experiment

- Seydişehir Alumina Powder provided from the Seydişehir Primary Aluminum Smelter
- Alumina Laboratory Scale (Sigma Aldrich, 325 mesh)
- Titania (Riedel de Haën)
- HA powder produced according to reference [47]
- Hydrochloric acid extra pure (37 %) (Honeywell)
- Nitric acid extra pure (65 %) (Sigma Aldrich)

III.1.2. Experimental Setup of Each Procedure





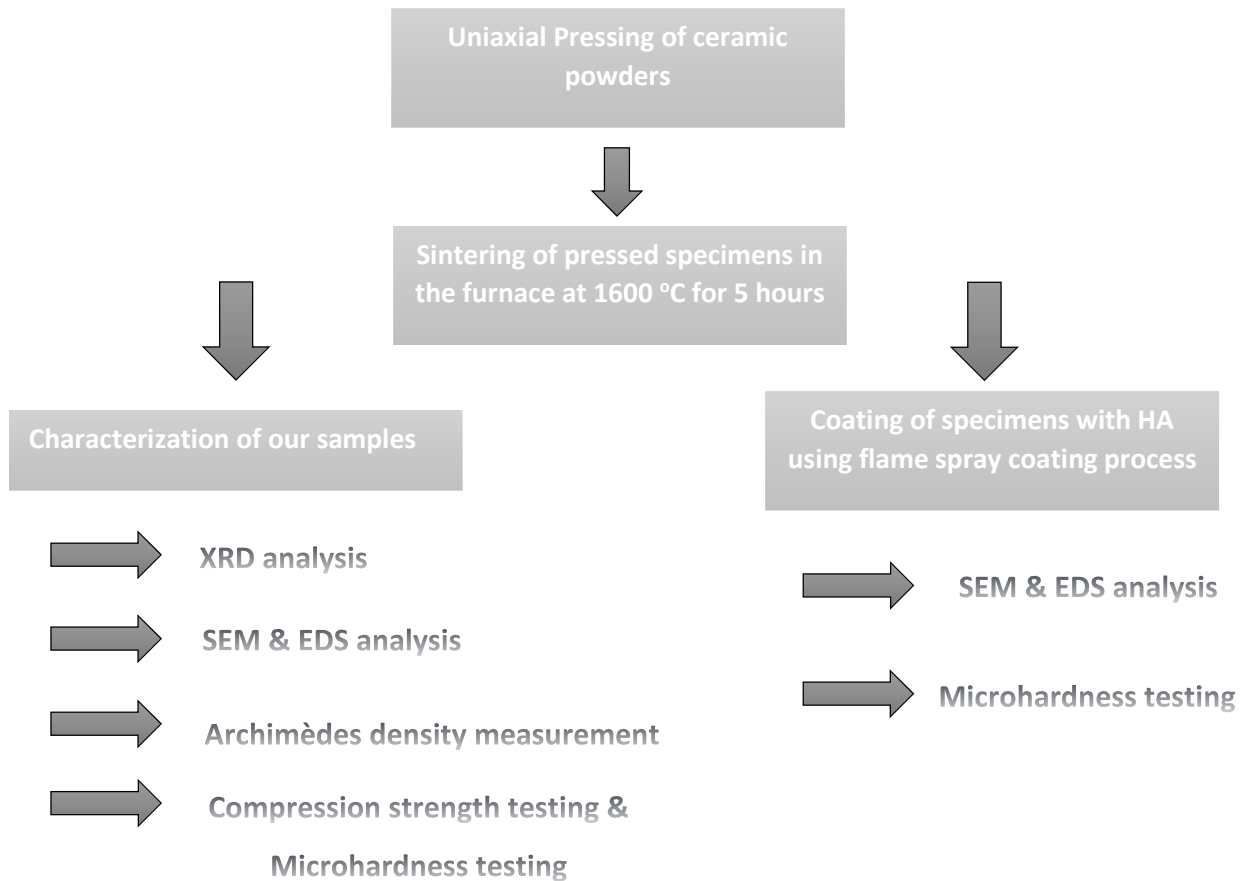


Figure 3.1. Experiment set up of our procedure.

As it was seen in Fig. 3.1., our experiment set up was summarized briefly.

In detail; the experiments in this study can be categorized in 3 stages as following;

1- Beneficiation of Seydişehir Alumina;

When the powders were first provided from Seydisehir Primary Aluminum Smelter, the differential thermal analysis (DTA) of alumina powders was performed with heating rate $10\text{ }^{\circ}\text{K}\cdot\text{min}^{-1}$ using Netzsch STA 409 CD in order to find out the critical temperatures during calcination of Seydişehir alumina. The sodium oxide and iron oxide contents of Seydisehir Alumina are important parameters for ratio of transformed alumina phases. The beneficiation process was performed to reduce the sodium oxide and iron oxide contents. In this process, the alumina powder supplied from Seydisehir Primary Aluminum Smelter (products of 2010) was stirred in a beaker containing “aqua regia” (mixture of 3 moles of HCl and 1 mole of HNO₃) on a hot plate at 150 °C during 1, 3 and

5 hours respectively. Subsequently, after each leaching process, the powders were washed with distilled water for 1 hour in a beaker containing on a hot plate at 100 °C [50]. This process can be seen in Fig. 3.2.



Figure 3.2. Procedure of beneficiation of Seydişehir alumina; a) alumina powder as taken (at left), b) leaching procedure on heating magnetic stirrer, c) After boiling with distilled water and decantation of the excess water.

After beneficiation, the powders were dried in a drying oven at 120 °C for 5 hours. Then the alumina powders were sintered at 1200 °C during 2 hours for the completion of phase transformation from γ -Al₂O₃ to α -Al₂O₃. This procedure can be seen in Fig. 3.3.



Figure 3.3. Powders of alumina after beneficiation when drying at the drying oven (at left) and when sintering in the furnace (at right).

XRD measurements of alumina powders before beneficiation, after beneficiation and crystallization at 1200 °C for 120 min were carried out using a Rigaku vertical diffractometer with Cu K α radiation, using a step of 0.02° (2 θ), with 2 s intervals and under conditions of 40 mA and 20 Kv. The diffraction lines were identified using the

program «JADE 6», there the phase content of Seydişehir alumina powder could be identified before and after beneficiation and calcination and realize the degree of the achievement of the transformation of $\gamma\text{-Al}_2\text{O}_3$ to $\alpha\text{-Al}_2\text{O}_3$.

The preparation of standard samples for the XRF characterization was an obligation to obtain a proper standard calibration curve for each element of our choice, here; iron, sodium (both impurities) and aluminum (to compute the alumina content). After beneficiation, the powders were dried in a drying oven at 120 °C for 5 hours. The standard calibration specimens were prepared according to the composition given in Table 3.1 in the HDPE bottles containing 1/3 slurry (distilled water+calibration specimen powder composition), 1/3 of grinding media (99.5 % pure alumina spheres, 10 mm \varnothing) and 1/3 of free space (see Figure 3.4.) and ball milled for 24 h, then dried in the drying oven at 120 °C for 5 hours. Then the pellets of different alumina powders of 20 mm of diameter for XRF analysis were prepared adding parafilm and cellulose mixture as binder and pressed using uniaxial automatic press. The same process was repeated for standard samples' analysis. XRF measurements of alumina powders before and after beneficiation were carried out using a Rigaku mini X-ray fluorescence spectrometer with Pd target material, using LiF, PeT, TAP crystals and under conditions of 1,25 mA and 40 Kv. The standard samples' composition were given at the Table 3.1 as weight percentage and at Table 3.2 as mass percentage. The calibration curves of standard samples were shown in the Figure 3.5, respectively.

Table 3.1. The standard samples' composition (weight %)

Samples	Fe (weight %)	Na (weight %)	Al (weight %)
Std 1	1	1	98
Std 2	5	5	90
Std 3	10	10	80

Table 3.2. The standard samples' composition (mass %).

Samples	Fe (measured mass %)	Na (measured mass %)	Al (measured mass %)
Std 1	0,14343	0,00653	58,07418
Std 2	0,76199	0,01021	60,42539
Std 3	2,62628	0,01348	57,37671



Figure 3.4. The standard calibration samples.

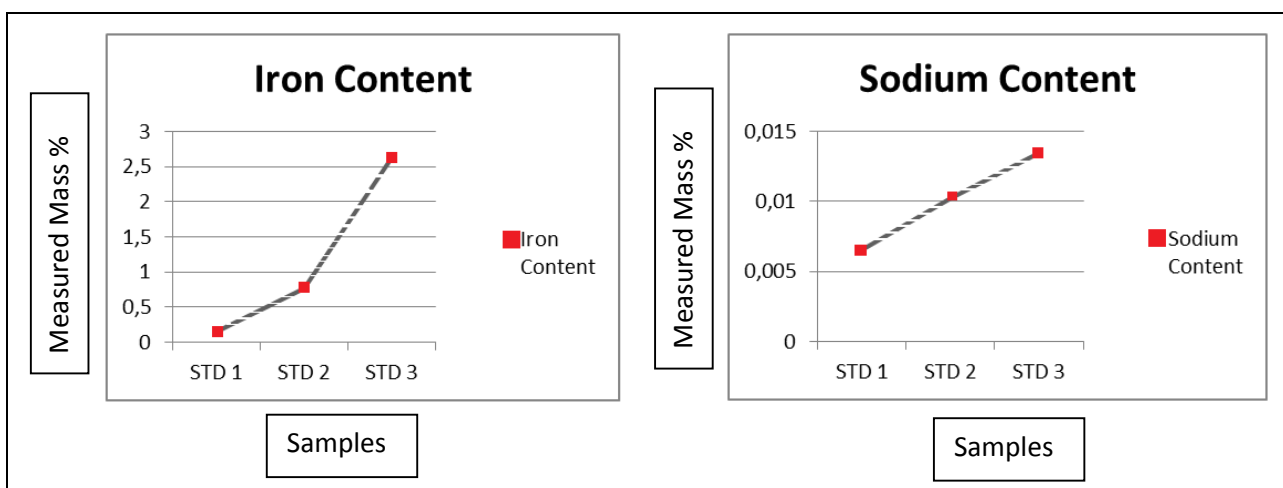


Figure 3.5. The calibration lines of standard samples.

Scanning electron microscopy (SEM) (Jeol JSM-5910 LV –Low Vacuum Scanning-) and energy dispersive spectroscopy (EDX) (Oxford Inca Energy 200) were used to characterize the alumina powders' particle size variations by different leaching times. These results were also detected, calculated and confirmed using Malvern laser particle sizer MU Hydro2000.

2- Production of Alumina-Titania Biocomposite;

The particle sizes of the alumina powders (beneficiated Seydişehir alumina and laboratory scale alumina powder) were made close to each other for a proper comparison using ball milling (rollers) procedure for 24 h. HDPE bottles containing 1/3 of the slurry (Ethyl alcohol (Merck, Ethanol Absolute Gr For Analysis + 34 g (~1/3 mole of Al_2O_3)) 1/3 of grinding media (99,5 % pure alumina spheres, 5 mm \varnothing) and 1/3 of free space were prepared and ball milled for 24 h. The particle size and its distribution for alumina powders were measured using a Malvern MU 2000 laser diffraction particle sizer. The blends whose ratio filtered from literature survey were coded as Seydişehir –S- (1), (2), (3) and (4) and Laboratory Alumina –L- (1), (2), (3), (4). They were weighed and mixed with acetone (Merck, Acetone Gr For Analysis Emsure) to prepare a proper slurry and then put into HDPE bottles. Each bottle contains 33 vol. % of the slurry, 33 vol. % of grinding media (99.5 % pure alumina spheres, 10 mm \varnothing) and 33 vol. % of free space. Each bottle contains “acetone” instead of “ethyl alcohol” or “water”. Magnesia used as sintering additive to decrease the sintering temperature can be transformed magnesium hydroxide when exposed to moisture. The slurry composition of each batch can be summarized as containing 2,5 wt %, 3,5 wt % and 4,5 wt % of MgO as the sintering aid, 1 wt % of SiO_2 and the balance; the alumina and titania powder mixture (1:1 mole) as seen in Table 3.3. The bottles were placed on ball milling rollers and rolled for 24 h to provide a better homogenization (See, Figure 3.6.). Following drying for 24 hours at 130 °C, pellets of 1 inch diameter were obtained using uniaxial manual press (2000 psi force was applied) (for the pressing procedure see, Figure 3.7) and sintered at 1600 °C (See, Figure 3.8. for the sintered specimens) with the following sintering regime;

40 °C → 300 °C in 52 minutes
 300 °C → 300 °C for 3 Hours
 300 °C → 1600 °C in 130 minutes
 1600 °C → 1600 °C for 5 Hours
 1600 °C → 40 °C in 24 Hours.

XRD measurements were carried out using a Rigaku vertical diffractometer with Cu K α radiation, using step size of 0.02° (2 θ), with 2 s intervals and under conditions of 40 mA and 20 kV to analyze the affect of the different alumina kinds and batch compositions on the phase formations and intensities. The sintered specimens were crushed and ground to finer powders using mortar and pestle to perform a proper analysis, each time mortar and pestle were cleaned with detergent, distilled water and pure ethyl alcohol (See, Figure 3.9) The diffraction lines were identified using the program «JADE 6» .

Scanning electron microscopy (SEM) (Jeol JSM-5910 LV –Low Vacuum Scanning-) and energy dispersive spectroscopy (EDX) (Oxford Inca Energy 200) were used to characterize the extraformed (or extrasynthesized) microstructure of the batches; the possible microcracks that can be formed and the residual phases such as existing in the microstructure not easily detected by XRD analysis.

The hardness measurements of the samples were done using Shimadzu Corporation (Scientific Instruments, Japan) Microhardness Tester, 500 g load for 20 s. This load was necessary because no indentation trace could be seen for 100 g and 200 g loading. The compression tests were performed using Devotrans Compression Strength Testing Instrument.

Table 3.3. The powder composition of each batch in the slurry.

Compositions	Alumina (wt.%)	Titania (wt.%)	Magnesia (wt.%)	Silica (wt.%)	Total (wt.%)
Composition 1	56,04	43,96	-	-	100.00
Composition 2	54,08	42,42	2,5	1	100.00
Composition 3	53,52	41,98	3,5	1	100.00
Composition 4	52,96	41,54	4,5	1	100.00



Figure 3.6. The basic ball milling process we applied for grinding and also homogenization of the specimens.



(a)



(b)



(c)



(d)



(e)



(f)



(g)



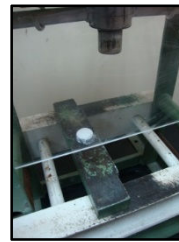
(h)



(i)



(j)



(k)

Figure 3.7. Pressing procedure; (a) the uniaxial manual pressing, (b) steel mold, (c) powder, (d); filled powder into the mold, (e) piston in the mold, (f) mold in the pressing, (g) pressing, (h) pressure applied onto the press (2000 psi), (i) and (j) relieving of pressure (0 psi), (k) ejection of the pellet from the mold.



Figure 3.8. Sintered specimens of the first group of -S- type specimens, from left to right, S1 group to S4 group.



Figure 3.9. Crushing and grinding of bioceramic pellets for XRD powder analysis measurements.

3- Coating with HA the alumina-titania substrate using flame spray process;

In this procedure, the operation was run in a private workshop outside the university, Yüzey Mühendislik Tic. Sti. In this study, Sulzer-Metco Combustion Flame Spray (6P-II Gun) System was used, before the procedure, the pipes and the powder feeder were cleaned using pressurized air, acetone and ethyl alcohol. Then, several trials were made until proper parameters to burn could be found and obtain a sustainable flame while spraying. At the end, it was realized that the bond coating material here Ni20Cr powders, Sulzer Metco Amdry 4535 whose composition is 19.5 wt. % of Cr, 0.75 wt.% of Si, 0.25 wt.% of Fe, 0.25 wt. % of Mn, 0.4 wt. % (max.) of other elements and Ni the rest was necessary to be used in order to increase the adhesion of the Bov.HA powders on the substrate. For, bovine HA coating, the parameters (gas mixture) used were as; 1 bars of acetylene, 4 bars of oxygen, 2 bars of air. This process was summarized in Fig. 3.10.



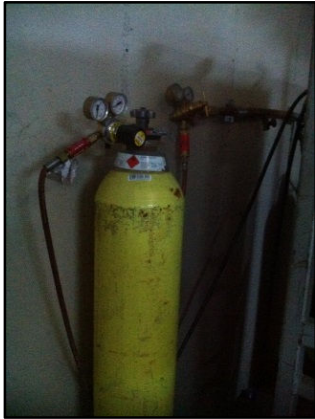
(a)



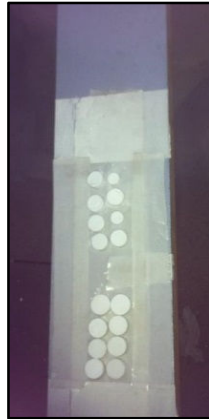
(b)



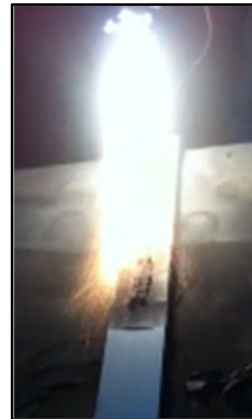
(c)



(d)



(e)



(f)



(g)



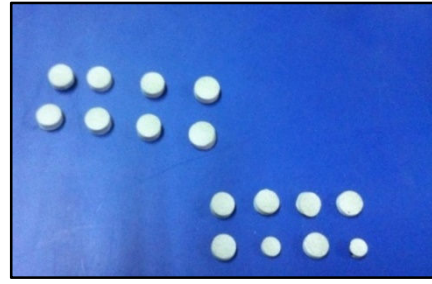
(h)



(i)



(j)



(k)

Figure 3.10. Our process of Bov.HA flame spray coating; a) Cleaned powder filler, b) Combustion Flame Spray System, c) Oxygen tubers, d) Acetylen tube, e) Our specimens put in the order for the process, f) and g) Bond coating application (specific color and shape of the flame; White and irregular), h) and i) Bovine HA coating application (specific color and shape of the flame; Yellowish orange and long curved), j) At the end of the application, our specimens, k) Our specimens when cooled down to the room temperature.

Scanning electron microscopy (SEM) and energy dispersive spectroscopy (EDX) were used to characterize the microstructure of the coatings; adhesion layers, bond coats and to measure the coating thickness.

The hardness measurements of the samples were done using Shimadzu Corporation (Scientific Instruments, Japan) Microhardness Tester, 500 g load for 20 s because any trace couldn't be seen for 100 g load and 200 g load, so this load and time can be a standard for this material to find out the hardness of the coating but also with the indentation testing, the fracture toughness, then the adhesion strength of each coating layer.

4. RESULTS and DISCUSSION

4.1. Results and Discussion of Beneficiation of Seydişehir Alumina

4.1.1. Differential Thermal Analysis Results and Discussion

25 % of the alumina produced in Seydişehir Primary Aluminum Smelter is α -alumina, the rest is the aluminum oxide phase. So there is still a great amount of alumina untransformed and also some quantity of possible boehmite phase remained as the dehydration reaction still occurs at about 375 °C, as the DTA analysis of alumina raw powders (see, Fig. 4.1) showed a phase transformation present between 1125 °C and 1250 °C, therefore the alumina powders were sintered at 1200 °C during 2 hours for the completion of phase transformation from γ - Al_2O_3 to α - Al_2O_3 (Corundum structure), XRD results approve this achievement (Fig. 4.3) [51].

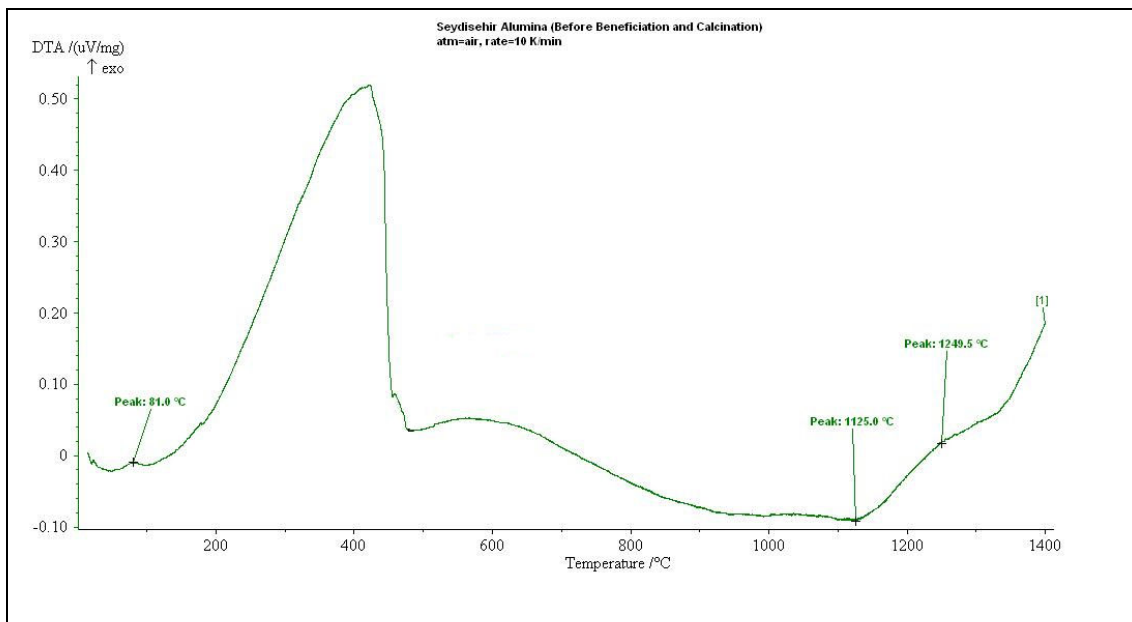


Figure 4.1. The DTA thermogram of Seydişehir alumina before beneficiation and calcination.

4.1.2. XRF Analysis Results and Discussion

The quantitative analysis results of the powders with different leaching times were presented at the Table 4.1. As seen in the Table 4.1, the most convenient leaching time is 3 hours comparing the percentage of alumina, iron and sodium content which were the most crucial parameters for the degree of beneficiation. The highest alumina, the lowest sodium content and also the optimum iron content were met after 3 hours leaching procedure. The calibration curves of Seydisehir alumina samples explain graphically this deduction in Fig. 4.2 [51].

Table 4.1. Seydisehir alumina (raw and with different leaching times) samples' composition (mass %) [51].

Samples	Fe (measured)	Na (measured)	Al (measured)
Sample 1 (raw powder)	0,04048	2,37028	86,3108
Sample 2 (1 hour leaching)	0,03909	0,87791	83,4366
Sample 3 (3 hour leaching)	0,03848	0,58710	89,5170
Sample 4 (5 hour leaching)	0,03876	0,68854	89,2492

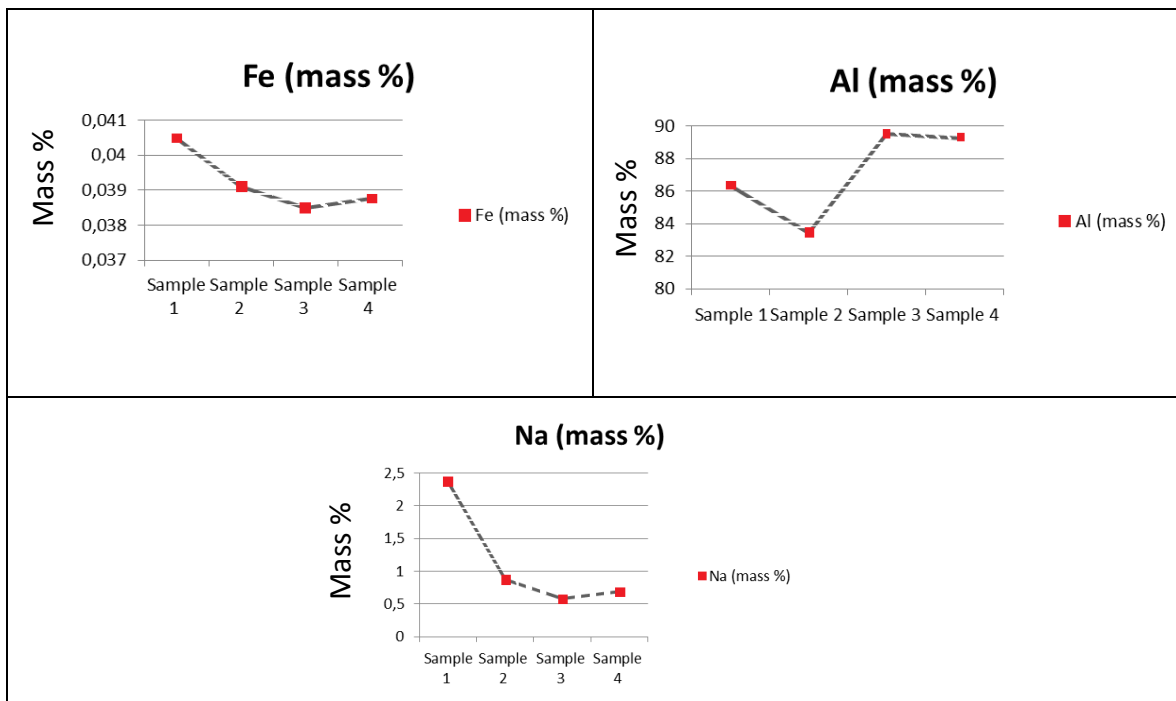


Figure 4.2. The calibration lines of Seydisehir alumina samples [51].

4.1.3. XRD Analysis Results and Discussion

As it was shown in the Figure 4.3. before the beneficiation and calcination, several aluminum oxide types including the corundum (α -alumina) and also sodium oxide phases were present at the structure. After beneficiation and calcination at 1200 °C, the complete transformation of aluminum oxides and the elimination of sodium oxide were observed.

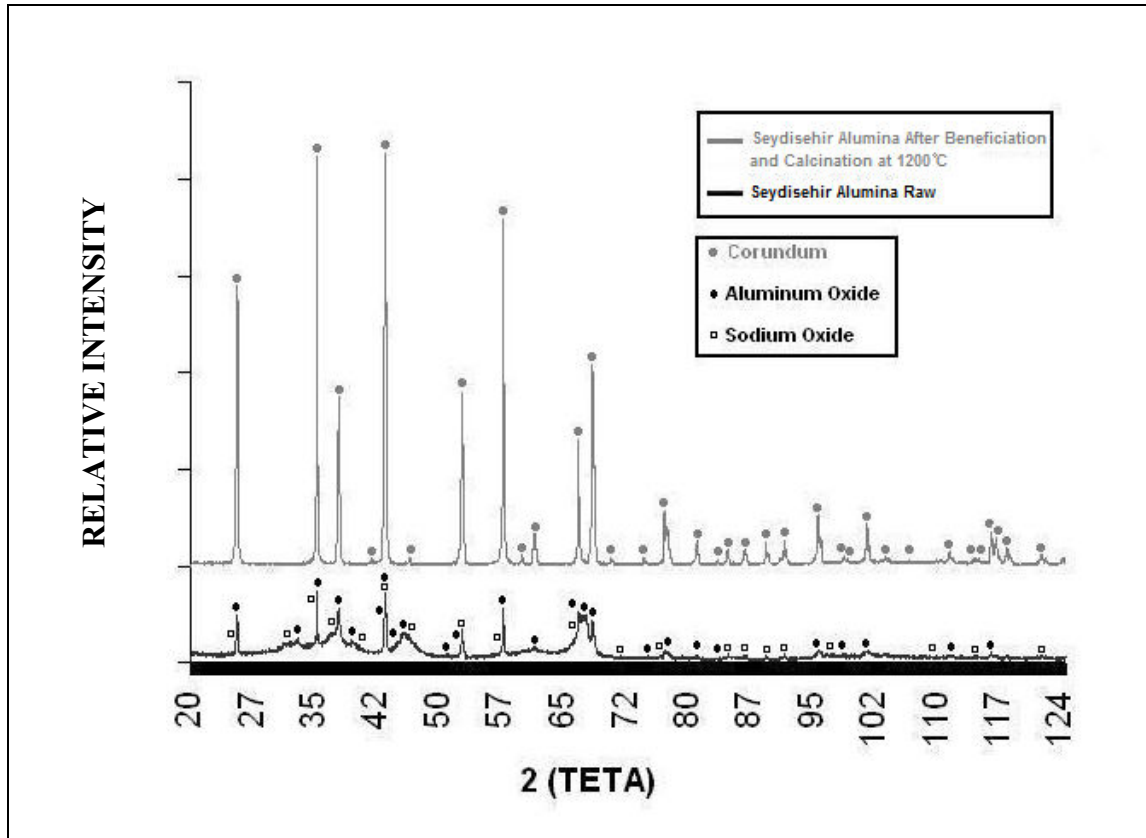


Figure 4.3. The XRD patterns of raw Seydisehir alumina and Seydisehir alumina powders after beneficiation and calcination at 1200 °C.

4.1.4. SEM Analysis Results and Discussion

After ball milling using alumina balls (10 mm of diameter) for 24 hours, grain sizes were observed using SEM. It is realized that, leaching time is also effective on the diminution of particle size (Fig. 4.4).

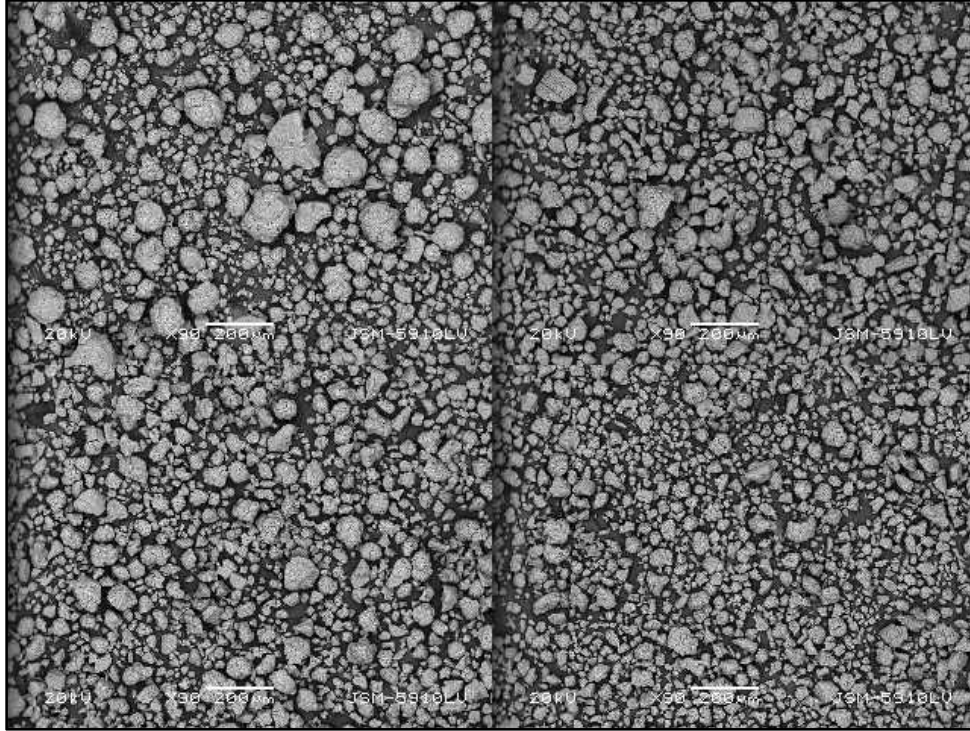


Figure 4.4. SEM micrographs of Seydisehir alumina powders (x90 magnification); Seydisehir raw alumina powder (**upleft**), after 3 hours of beneficiation and after calcination at 1200 °C (**downleft**), after 5 hours of beneficiation and after calcination at 1200 °C for 2 hours (**downright**).

4.1.5. Laser Particle Size Results and Discussion

The average particle size distribution was detected and calculated using Malvern laser particle sizer. The results were shown in Fig. 4.5. The average particle size was 31,20 μm and largely culminated in this particle size area. It can be claimed that the size distribution is mono dispersive. The SEM results verified our laser particle sizer's findings and also with increasing time of leaching, a diminution in particle sizes is observed (Fig. 4.4).

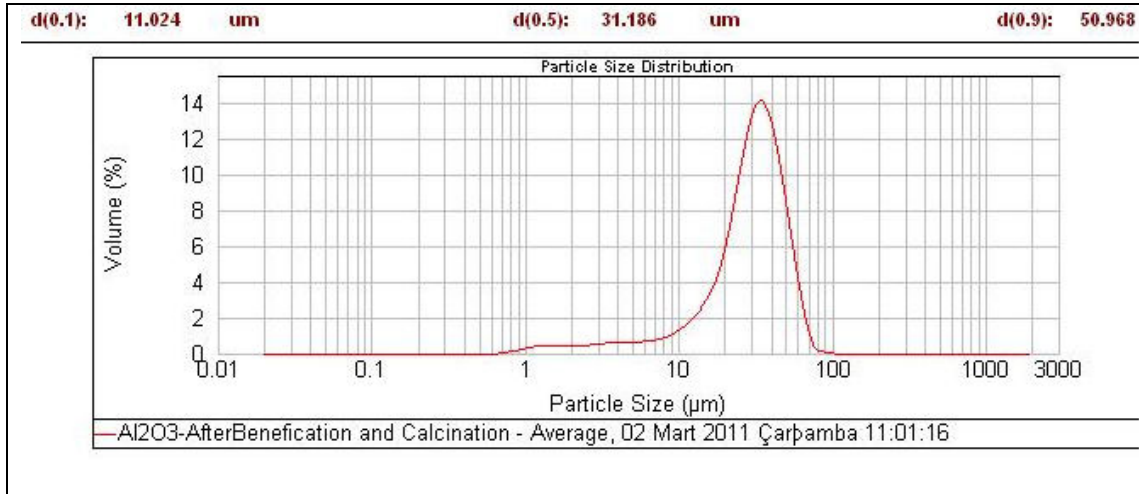


Figure 4.5. The average particle size distribution of Seydisehir alumina powders after beneficiation and calcination before ball milling.

4.2. Results and Discussion of Production of Alumina-Titania Biocomposite

4.2.1. Archimèdes Density Measurement Results and Discussion

After the Archimèdes density measurement, it was realized that the -S- type specimens are slightly denser comparing to -L- type specimens –for their compositions see Table 3.3- (Table 4.2.). The densities belonging to different samples are given in Fig. 4.6, it can be considered in normal range (3-3,4 g/cm³) of the tialite. The porosity of the material is also less in the S type specimens.

Table 4.2. Results of Archimèdes density measurements.

	Va	Vb	Da	Db	Pa
S1	0,388	0,400	3,131	3,036	3,038
S2	0,420	0,476	3,397	3,002	11,638
S3	0,748	0,761	3,167	3,068	2,949
S4	0,611	0,639	3,190	3,053	4,293
L1	0,462	0,722	4,684	2,998	35,991
L2	0,877	0,921	3,159	3,009	4,758
L3	0,884	1,110	3,768	3,003	20,309
L4	0,586	0,956	4,688	2,874	38,701

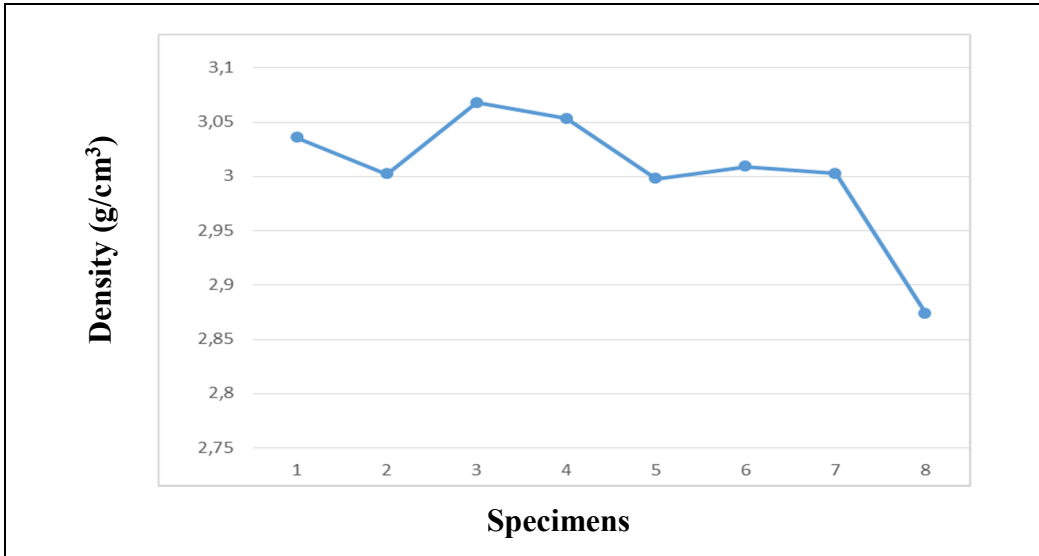


Figure 4.6. Graphical comparison of the specimens' density (1-4; S1-4 and 5-8; L1-4).

4.2.2. XRD Analysis Results and Discussion

The diffraction peaks observed in XRD patterns belong to tialite phase completely, this result points out success in obtaining tialite phase formation even without adding any additives at 1600 °C, lower than the temperature mentioned in literature [17-34]. But the addition of secondary additives, which are magnesia and silica, were not detected inside the peak distribution because of the detection limit of the XRD instrument (5 wt. %). They might shade slightly the main alumina-titania phases diminishing their intensities; this effect is more pronounced in the –S- type composites with higher impurity content which is higher comparing to the –L- type samples (Fig. 4.7. and 4.8.). The main difference is the difference in the peak intensities for different batches (samples). “S” specimens show higher values than other (Fig. 4.9.). This result can be attributed to the residual iron oxide content of –S- type specimens (Seydişehir Alumina, after 3 h leaching and calcination at 1200 °C) comparing to –L- type (Laboratory scale alumina) which were much more industrially purified and processed alumina powders. The numbers –such as S1 or L2- indicate here, the amount of magnesia increasing, i.e. “1”; no addition and “4”; 4,5 wt. % with 1 wt. % of silica which is the same for “2”, “3” and “4” as they are all mentioned in Table 3.3.

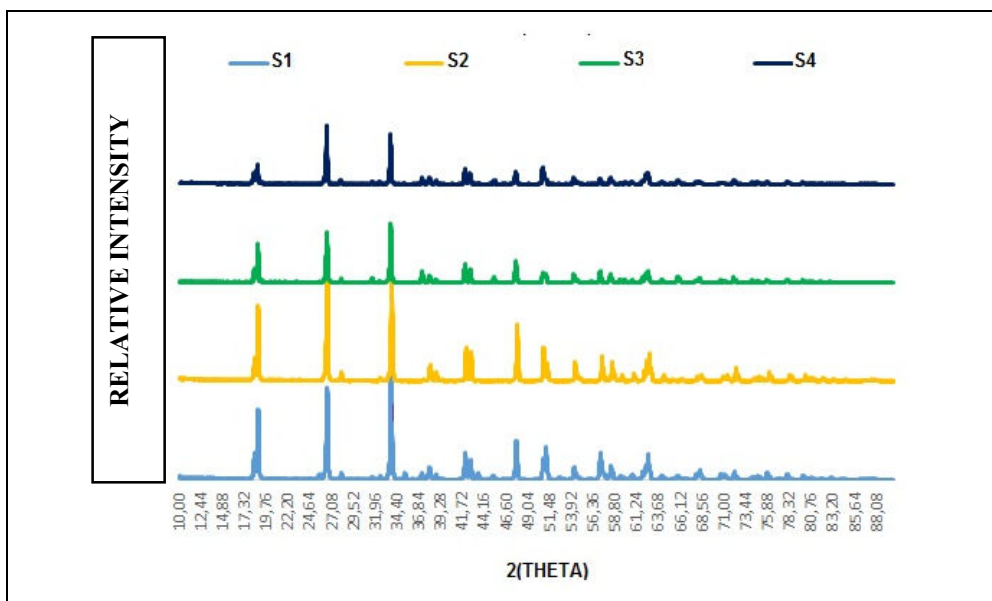


Figure 4.7. The XRD peaks of -S- type specimens.

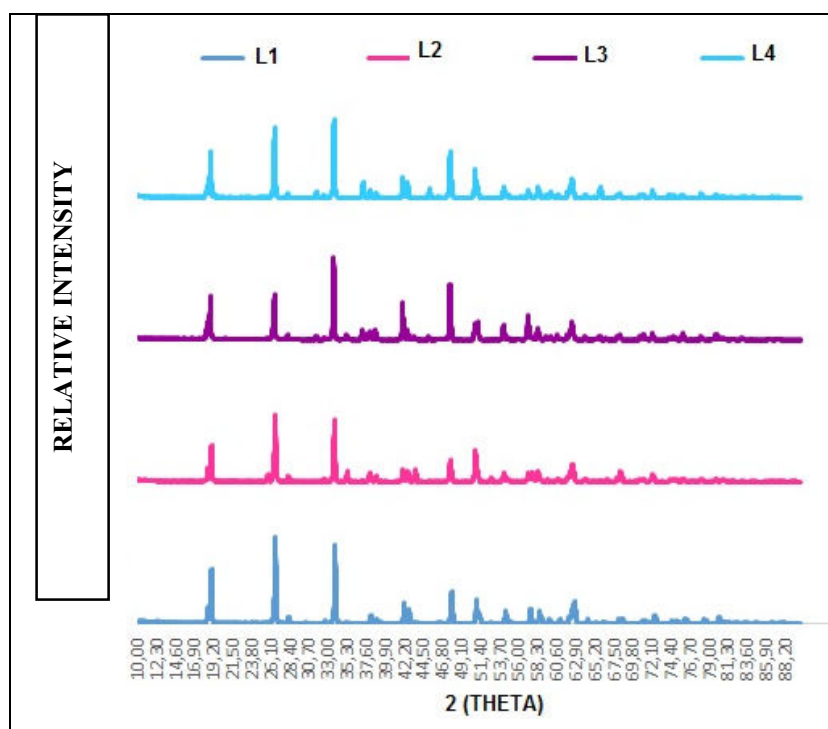


Figure 4.8. The XRD peaks of -L- type specimens.

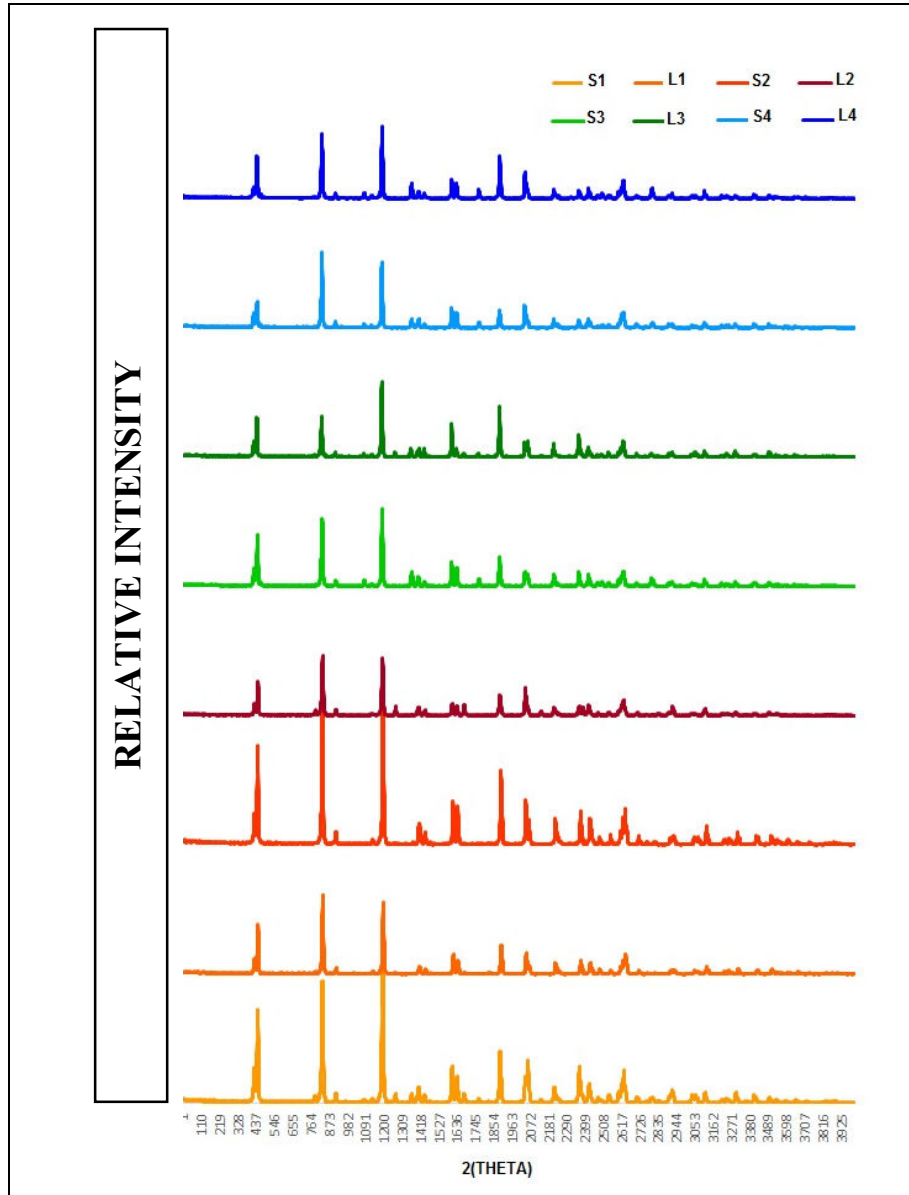
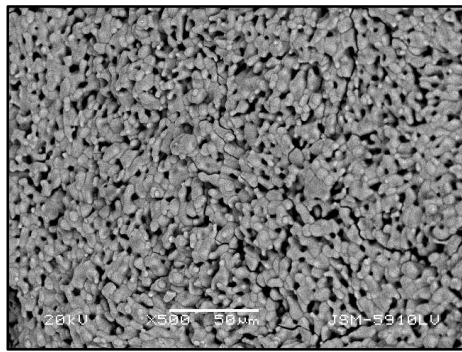


Figure 4.9. The comparison of XRD peaks of our specimens.

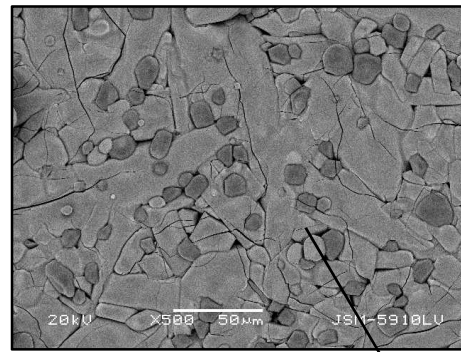
4.2.3. SEM and EDS Analysis Results and Discussion

According to the SEM microstructure of the specimens shown in Fig. 4.10 and 4.11, due to the morphology of the starting powders, -L- type specimens' grains were much more spherical while -S- type specimens are quite disordered and but less porous, which was also coherent with the Archimedes density results. It was also obvious that, the addition of 2,5 wt. % MgO and 1 wt. % SiO₂ (Quartz phase) caused the extreme grain growth of the main phase in both group of specimens, the inclusions situated in the grain boundaries

didn't help to slow down this phenomenon in -L- type specimens. Besides this, the finer grains were found in the microstructure of S3 type specimen which had the lowest porosity and the highest density amongst all the specimens.

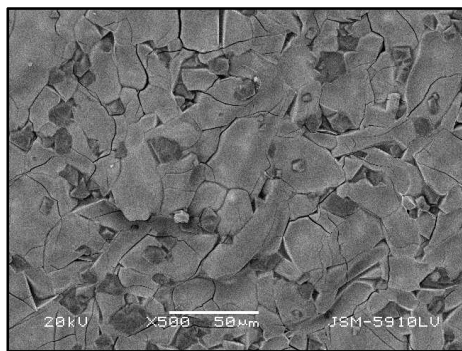


(L1)

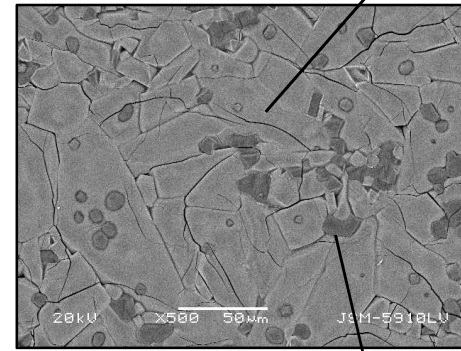


(L2)

Al_2TiO_5

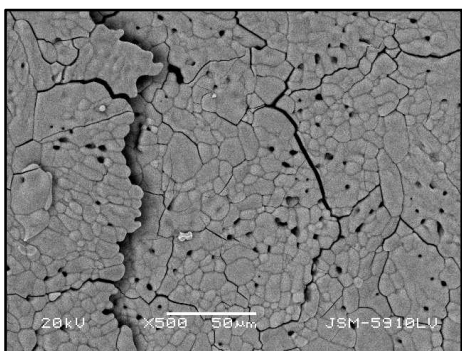


(L3)

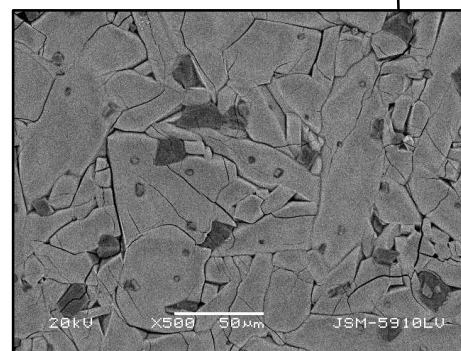


(L4)

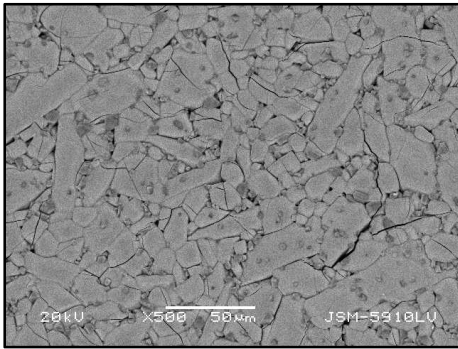
Spinel phase



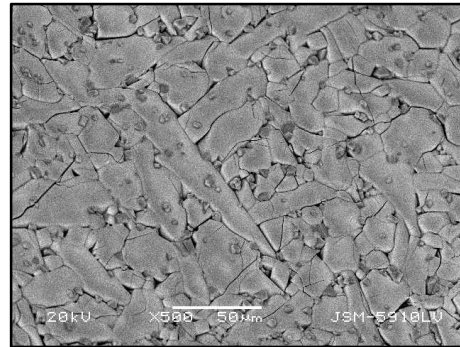
(S1)



(S2)

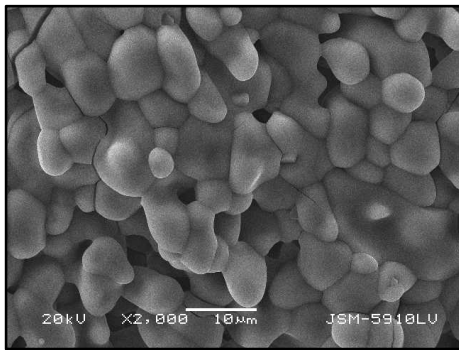


(S3)

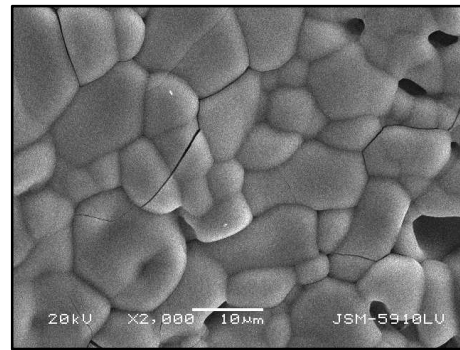


(S4)

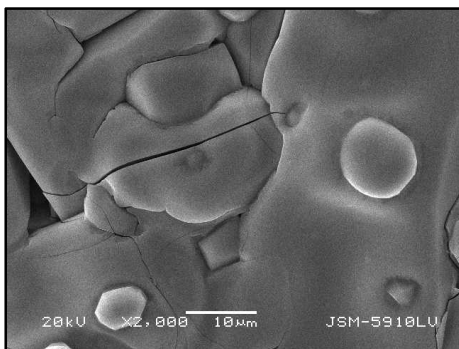
Figure 4.10. Comparison of all the batches sintered at the same temperature (1600 °C) with the same magnification (x500, back scattering mode).



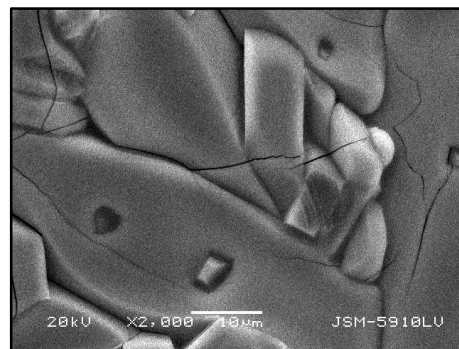
(L1)



(S1)

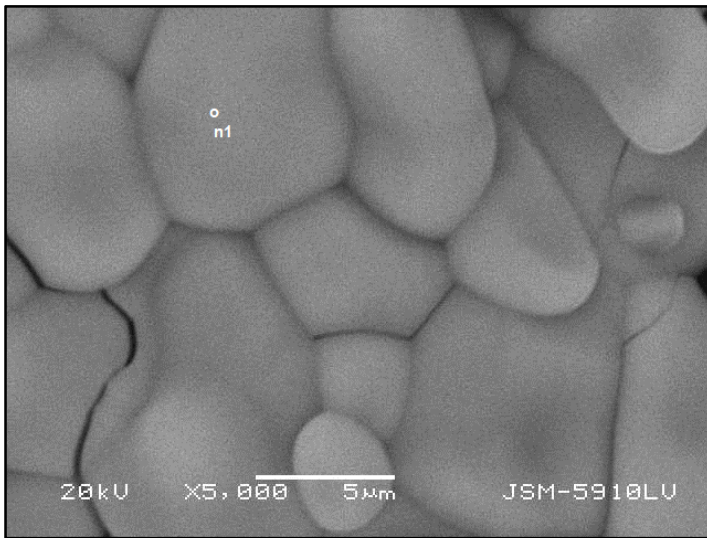


(L2)



(S2)

In this research, as it was expected, the EDS analysis of L1 and S1 type materials showed a homogeneous structure, there was only the aluminum titanate matrix composed of alumina and titania phases present in the structure confirmed in the EDS analysis mentioned in Fig.4.12 and 4.13. In the EDS analysis (L4 and S4 samples; Fig.4.14 and 15, respectively) it is concluded that the angular, sharp edged inclusions in the grain boundaries contained mainly alumina-titania and little amounts of MgO and SiO₂, indicating the presence of spinel phase.



Processing option : All elements analyzed (Normalised)

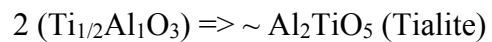
Spectrum	O	Al	Ti	Total
Spectrum 1	48.60	25.12	26.28	100.00
Max.	48.60	25.12	26.28	
Min.	48.60	25.12	26.28	

All results in Weight Percent

$$\text{O: } 48.60 / 16 = 3.075 \sim 3$$

$$\text{Al: } 25.12 / 12 = 0.93 \sim 1$$

$$\text{Ti: } 26.28 / 48 = 0.54 \sim 1/2$$



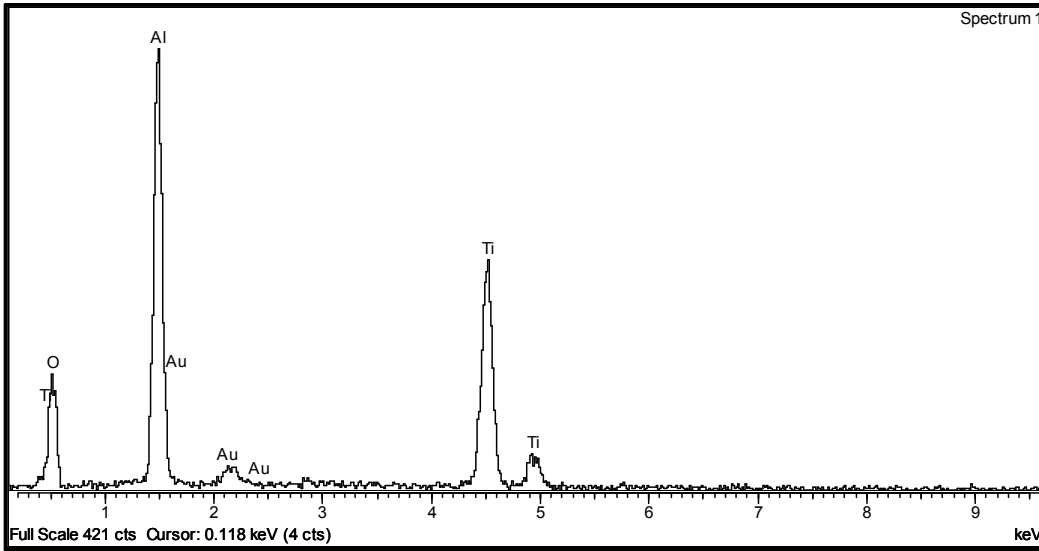
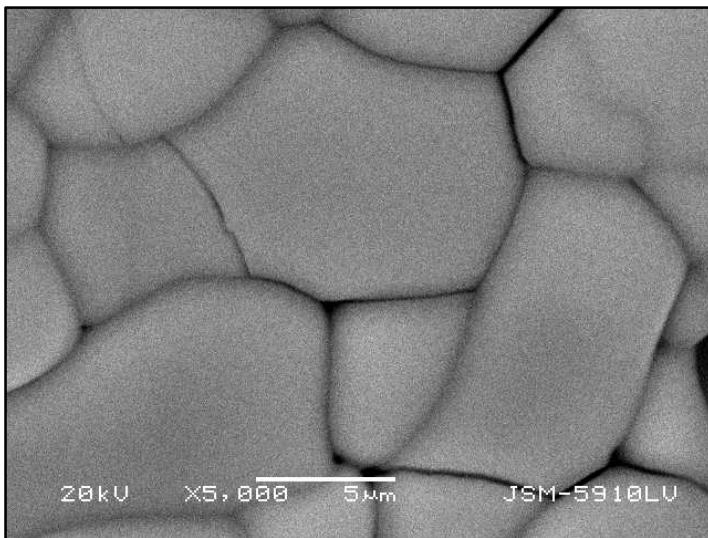


Figure 4.12. SEM microstructure (x5000, back scattering mode) and the related EDS analysis of L1 type specimen.



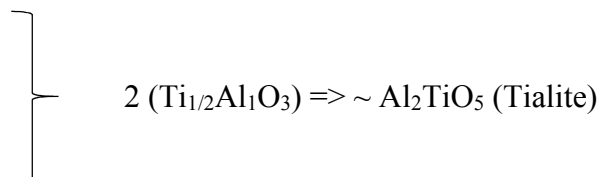
Processing option : All elements analyzed (Normalised). All results in Weight Percent.

Spectrum	O	Al	Ti	Total
Spectrum 1	45.57	26.69	27.75	100.00
Max.	45.57	26.69	27.75	
Min.	45.57	26.69	27.75	

$$\text{O: } 45.57 / 16 = 2.848 \sim 3$$

$$\text{Al: } 26.69 / 27 = 0.98 \sim 1$$

$$\text{Ti: } 27.75 / 48 = 0.57 \sim \frac{1}{2}$$



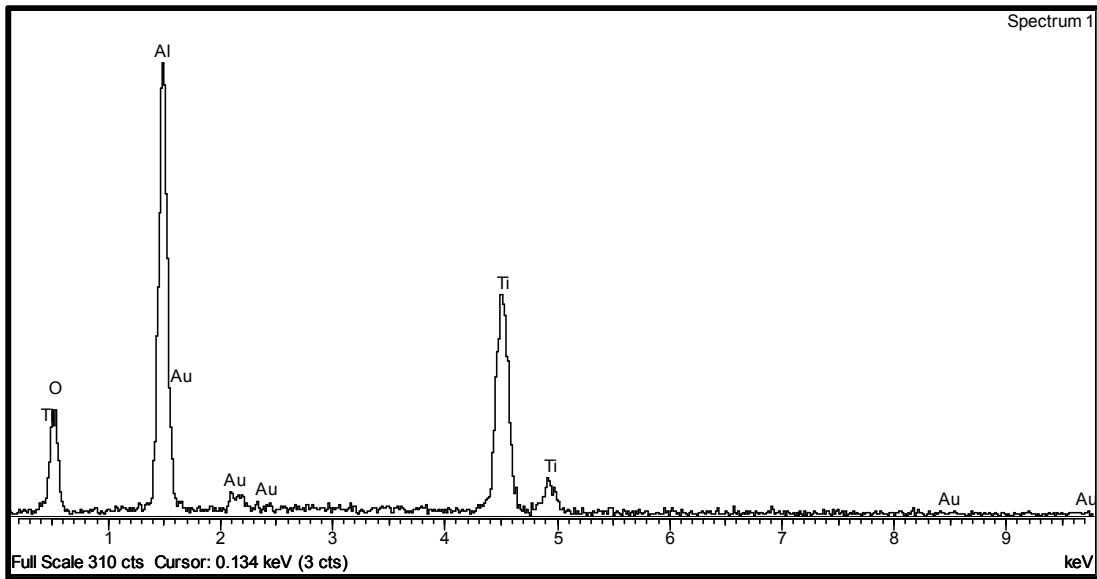
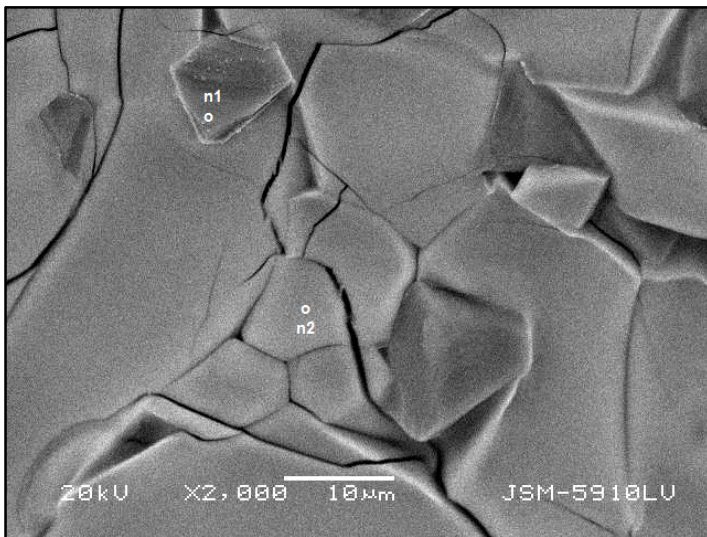


Figure 4.13. SEM microstructure (x5000, back scattering mode) and the related EDS analysis of S1 specimen.



Processing option : All elements analyzed (Normalised)

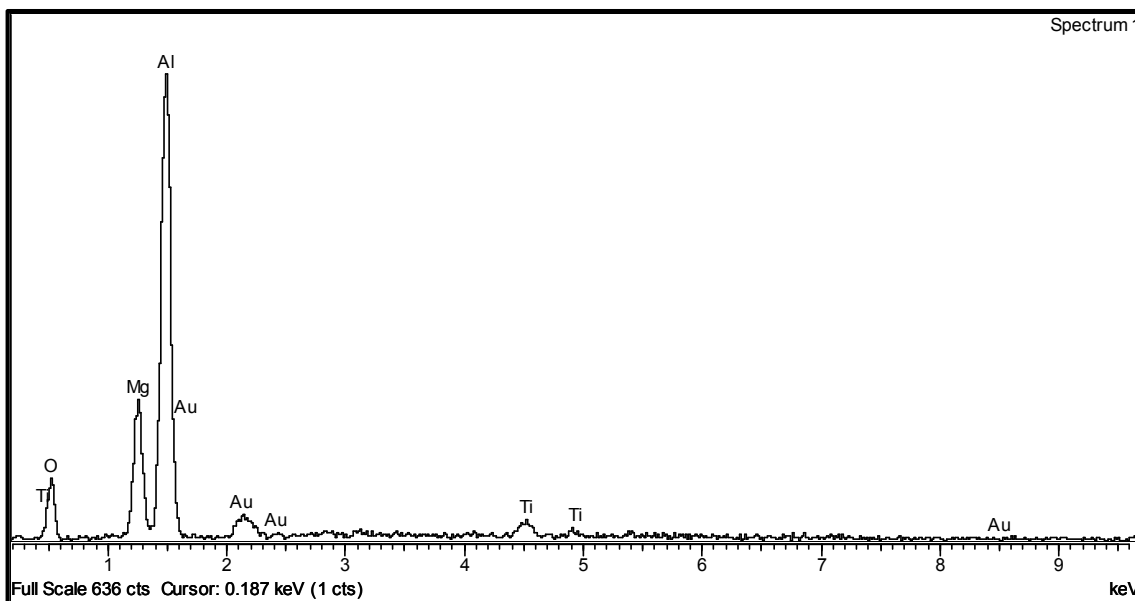
Spectrum	O	Mg	Al	Ti	Total
Spectrum n1	30.62	13.30	51.93	4.15	100.00
Max.	30.62	13.30	51.93	4.15	
Min.	30.62	13.30	51.93	4.15	

O: $30.62 / 16 = 1.91 \sim 2$
 Al: $51.93 / 27 = 1.92 \sim 2$
 Ti: $4.15 / 48 = 0.08 \sim 0.01$
 Mg: $13.30 / 24.30 = 0.55 \sim \frac{1}{2}$

$2(\text{Mg}_{0.55}\text{Al}_{1.92}\text{O}_{1.91}) \Rightarrow \sim \text{Al}_{3.84}\text{Mg}_{1.1}\text{O}_{3.82}$; point 'n1'. These EDS results taken at point 'n1' indicated that particles formed on the junctions are Al rich solid solution of spinel ' $\text{Al}_{3.84}\text{Mg}_{1.1}\text{O}_{3.82}$ ' possessing some oxygen vacancies.

All results in Weight Percent

EDS analysis of the point 'n1'



Processing option : All elements analyzed (Normalised)

Spectrum	O	Mg	Al	Si	Ti	Total
Spectrum n2	37.16	1.41	24.58	0.13	36.73	100.00
Max.	37.16	1.41	24.58	0.13	36.73	
Min.	37.16	1.41	24.58	0.13	36.73	

All results in Weight Percent

O: $37.16 / 16 = 2.3225 \sim 2$
 Al: $24.58 / 27 = 0.91 \sim 1$
 Ti: $36.73 / 48 = 0.7652 \sim 1$

$\text{Ti}_1\text{Al}_1\text{O}_2 \Rightarrow$ Because of the diffusion, the area is poor in aluminum dioxide in 'n2' rather than 'n1'.

EDS analysis of the point 'n2'

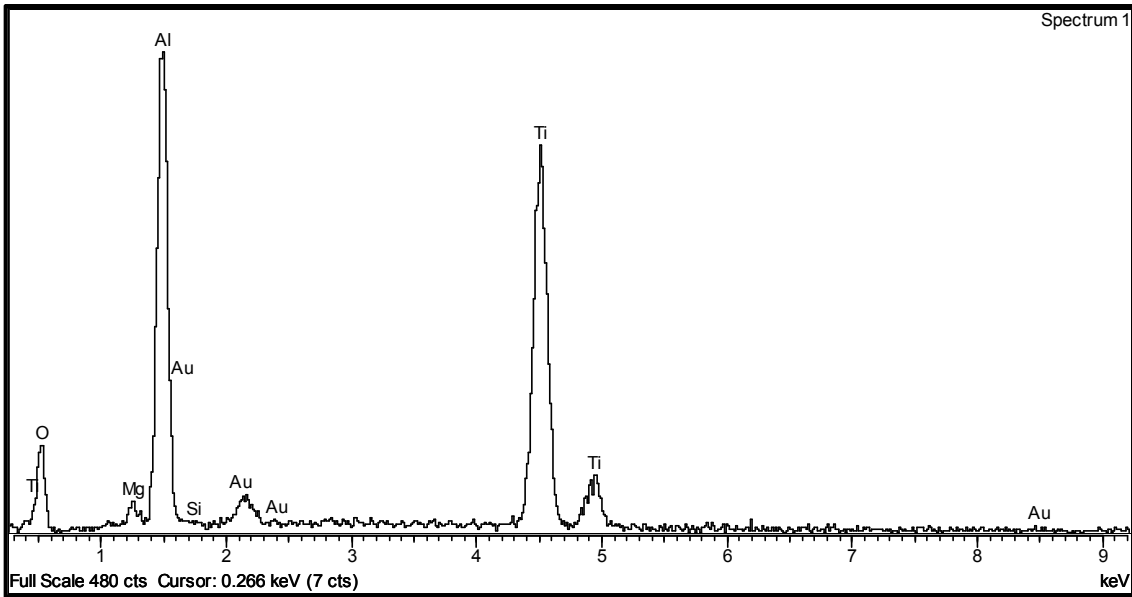
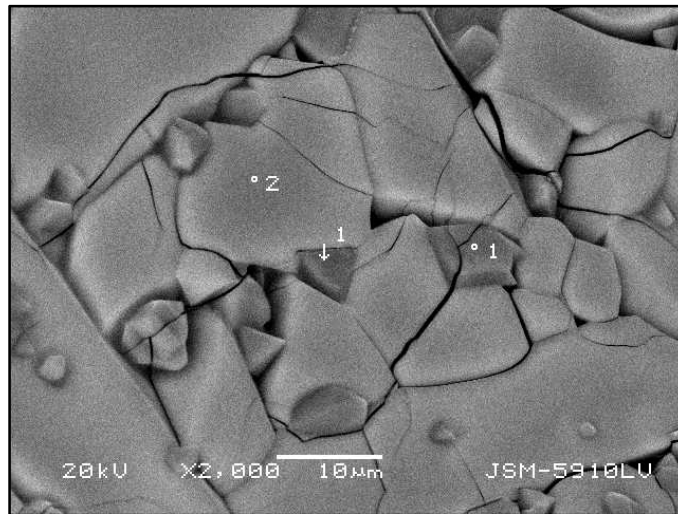


Figure 4.14. SEM microstructure (x2000, back scattering mode) and the related EDS analysis of L4 specimen indicating different composition at the different places of the structure “n1” and “n2”.



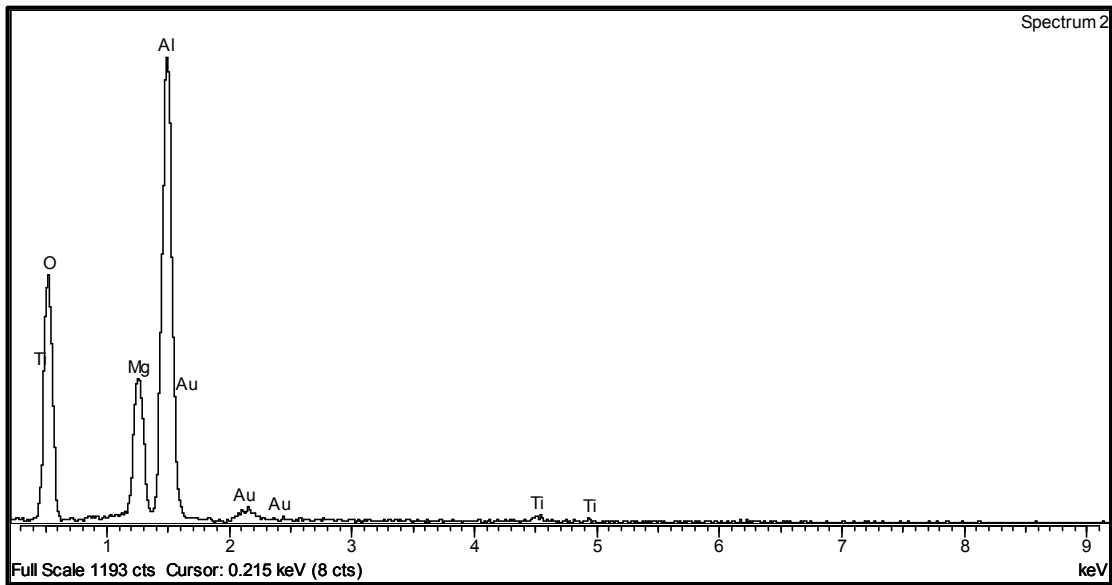
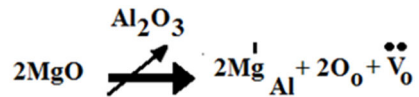
Processing option : All elements analyzed (Normalised)

Spectrum	O	Mg	Al	Ti	Total
Spectrum 2	53.08	11.02	35.16	0.75	100.00
Max.	53.08	11.02	35.16	0.75	
Min.	53.08	11.02	35.16	0.75	

O: 53.08 / 16 = 3.31 ~ 3
 Al: 35.16 / 27 = 1.3 ~ 1
 Mg: 11.02 / 24.30 = 0.45 ~ 1/2

2(Mg_{0.5}Al_{1.3}O_{3.31}) => ~ Al_{2.6}Mg_{1.0}O_{6.62} ; point 'n1'. These EDS results taken at point 'n1' indicated that particles formed on the junctions are Al rich solid solution of spinel 'Al_{2.6}Mg_{1.0}O_{6.62}' possessing some oxygen vacancies.

EDS analysis of the point 'n1'



Processing option : All elements analyzed (Normalised)

Spectrum	O	Mg	Al	Si	Ti	Total
Spectrum 1	49.53	1.56	25.08	0.12	23.71	100.00
Max.	49.53	1.56	25.08	0.12	23.71	
Min.	49.53	1.56	25.08	0.12	23.71	

O: 49.53 / 16 = 3.1 ~ 3
 Al: 25.08 / 27 = 0.93 ~ 1
 Ti: 23.71 / 48 = 0.49 ~ 1/2
 Mg: 1.56 / 24.30 = 0.06

2(Ti_{0.5}Al_{0.93}O₃) => Al₂Ti_{1.0}O₆ ~ Al₂TiO₅ (Tialite)

EDS analysis of the point 'n2'

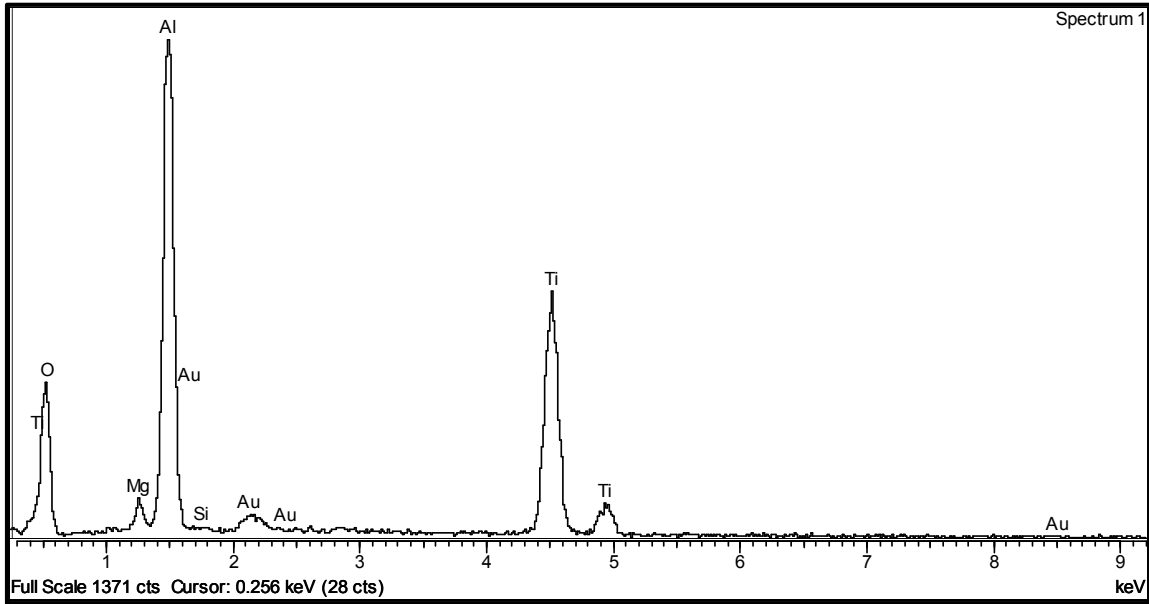


Figure 4.15. SEM microstructure (x2000, back scattering mode) and the related EDS analysis of S4 specimen indicating different composition at the different places of the structure “1” and “2”.

IV.2.4. Microhardness Testing Results and Discussion

The microhardness values, standard deviation of the composites are given in Table 4.3.

Table 4.3. Results of microhardness testing of the alumina-titania biocomposite.

Specimens	Values of Microhardness (HV)					Standard Deviation	Average Microhardness (HV)
S1	452	785	514	487	622	120,71	572
S2	804	824	794	720	864	47,15	801,2
S3	995	720	818	921	898	94,04	870,4
S4	1156	925	1400	1455	1515	219,60	1290,2
L1	240	270	343	374	403	61,73	326
L2	774	614	680	590	710	66,31	673,6
L3	748	882	853	586	876	112,43	789
L4	1082	998	900	1156	1504	206,48	1128

According to these results shown graphically in Fig. 4.16, the -S-type materials are harder, which is consistent with the XRD analysis, Archimèdes density measurement and SEM microstructure evaluation. S4 should be considered as the hardest among all due to the affect of magnesia and silica addition into the crystal lattice of the material (especially magnesia confirmed by the EDS analysis in Fig 4.15 (Also see, the comparison of the specimens' hardnesses with standard deviation lines).

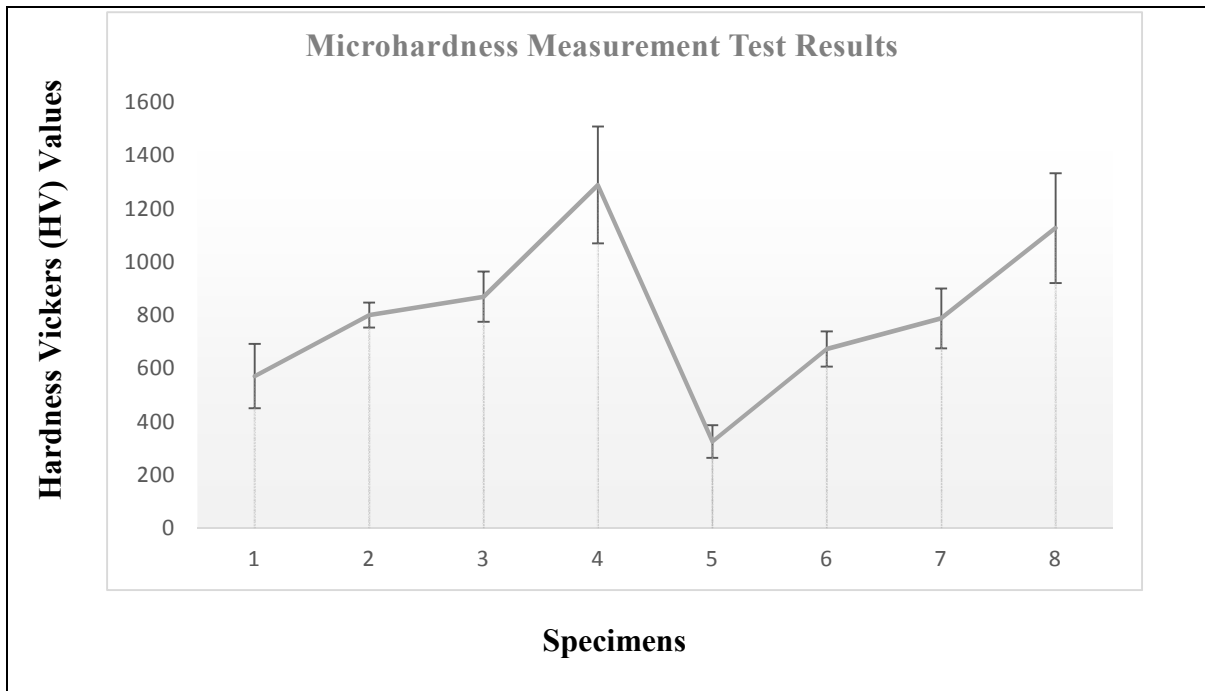


Figure 4.16. Comparison of the specimens' hardnesses (1: S1, 2:S2, 3:S3, 4:S4, 5:L1, 6:L2, 7:L3, 8:L4).

4.2.5. Compressive Strength Testing Results and Discussion

Because of the reason specified in previous chapters and titles, the -S- type materials' compressive strength were highly over the -L- type materials (See table 4.4 and Fig. 4.17). Here the S2 type specimens' compressive strength is highest among all, it could be attributed to the combination of its comparatively granular microstructure containing less microcracks than -S3- and -S4- type specimens with the a degree of addition of magnesia and silica sintering densifying additives.

Table 4.4. Results of compressive strength testing results.

Specimens	Compressive Strength Values (N)			Standard Deviation (N)	Standard Deviation (MPa)	Average (N)	Average (MPa)
L1	16460	22690	16580	2908,98	17,21	18576,67	109,92
L2	22315	21190	17590	2015,25	13,99	20365	141,42
L3	23850	16950	12935	4507,62	31,30	17911,67	124,39
L4	16520	15200	19220	1673,08	11,62	16980	117,92
S1	17824	20732	13487	2976,88	22,51	17347,67	131,17
S2	26740	26325	32630	2879,38	21,77	28565	215,99
S3	15680	23547	18747	3237,56	24,48	19324,67	146,12
S4	18990	27645	23545	3535,016	26,73	23393,33	176,89

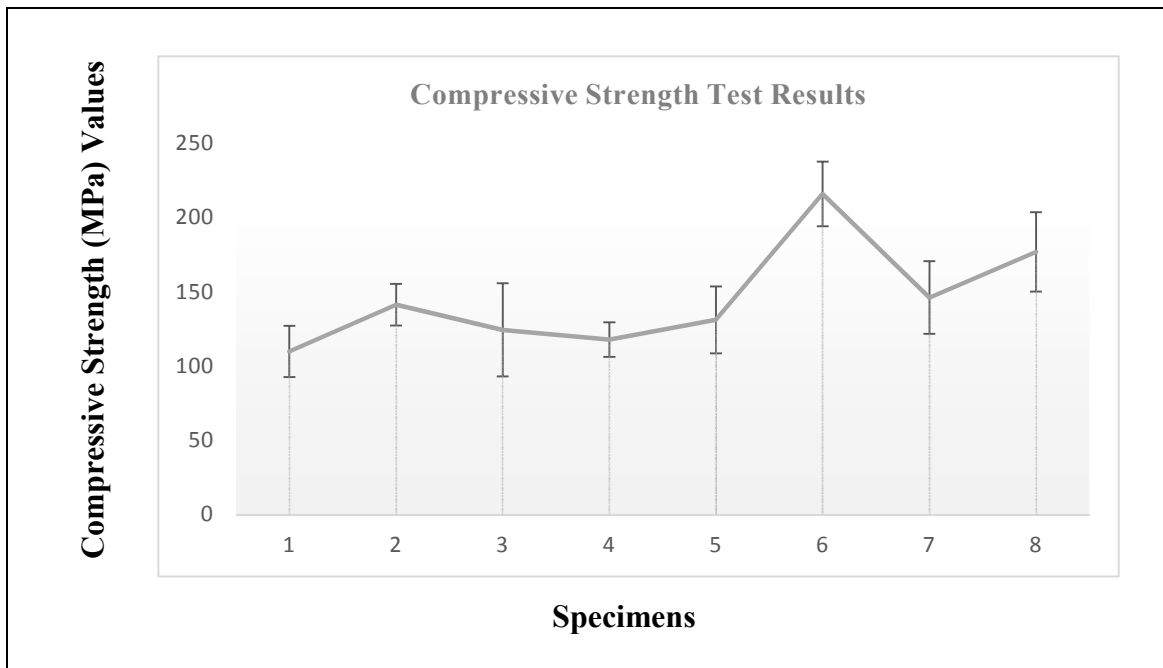


Figure 4.17. Comparison of the specimens' compressive strength. (1: S1, 2: S2, 3:S3, 4:S4, 5:L1, 6:L2, 7:L3, 8:L4).

4.3. Results and Discussion of Coating with HA the Alumina-Titania Substrate using Flame Spray Process

IV.3.1. Microhardness Testing Results and Discussion

The microhardness of the specimens seemed to be increased as the porous structure on the surface of the material firstly filled with bond coating, then with bovine HA, finally to obtain a smooth measurement surface, it was polished before the analysis, therefore a pore free and denser surface were created to run the analysis (See, Table 4.5, Fig.4.18). As the substrate was hard but brittle, the surface after coating became tougher, following this procedure the surface hardness was increased in parallel with the increased fracture toughness.

Table 4.5. Results of microhardness testing of the alumina-titania biocomposite coated with HA using the combustion flame spray method.

Specimens	Microhardness Values (HV)			Standard Deviation (HV)	Average Microhardness Value (HV)
CS1	1020	725	840	121,40	861,67
CS2	853	533	787	137,95	724,33
CS3	1422	1438	1605	82,75	1488,33
CS4	1150	1597	1880	300,52	1542,33
CL1	646	435	459	94,32	513,33
CL2	889	623	734	109,09	748,67
CL3	732	676	752	32,17	720,00
CL4	1181	534	1214	313,07	976,33

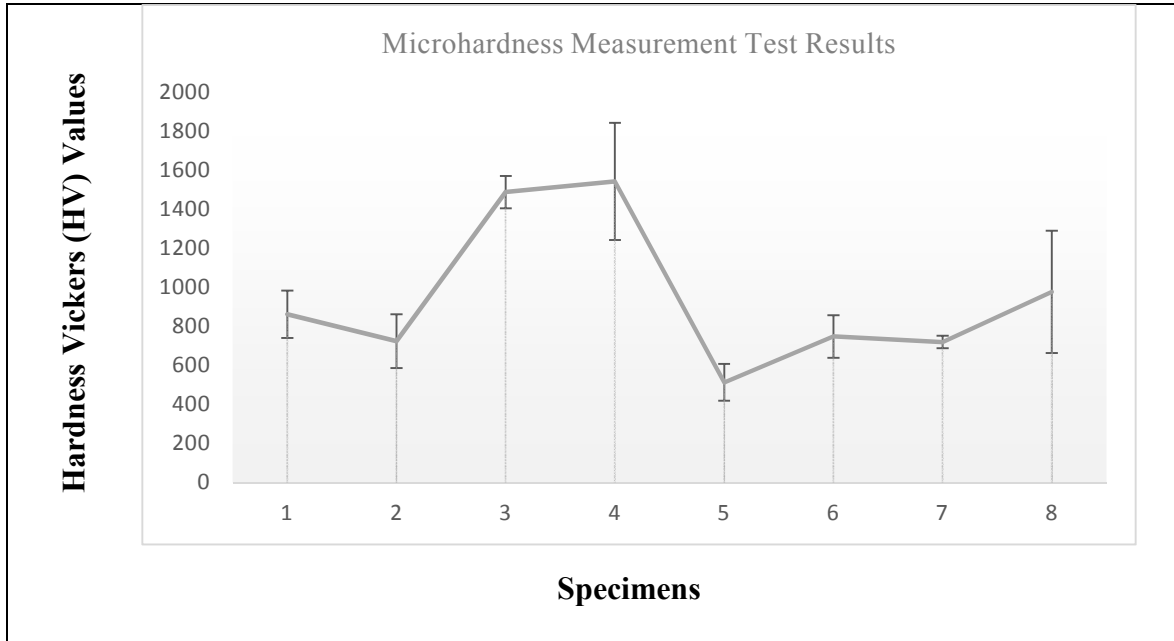


Figure 4.18. Comparison of the specimens' hardnesses after coating (1: CS1, 2: CS2, 3:CS3, 4:CS4, 5:CL1, 6:CL2, 7:CL3, 8:CL4).

During microhardness testing, the fracture toughness of the coating layers and the substrate itself were cross-sectionally measured but any sign of fracture was not seen due to uniaxial pressing and the unidirectional deposition of thermal spray coating layer, the hardness of the material (substrate + surface coating) on the perpendicular direction to the force is high therefore the material shows resistance to penetration of diamond tip, however laterally (parallel to the face) the material instead of resisting to the forces applied by diamond tip, absorbs energy (See, Fig. 4.19), on each cases no start of crack propagation could be observed, which could be attributed to the high toughness of the material.

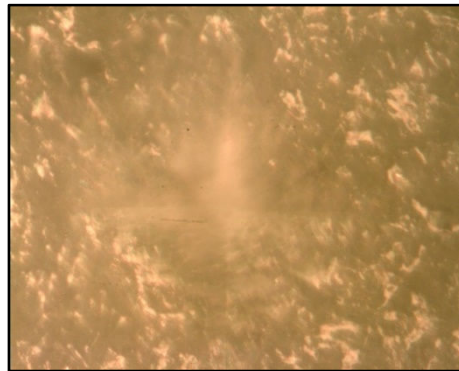


Figure 4.19. Trace of diamond probe of Vickers microhardness measurement device taken on the coating's cross-section.

4.3.2. SEM and EDS Analysis Results and Discussion

The SEM and EDS analysis of the coated samples were performed, in addition to the stereomicroscopic analysis. The coating thickness of these materials are adequate for a possible tympanoplastic implant to be used in the ear. On every specimen, the layer of interlayer; bond coating Ni-20Cr and the main coating; bovine hydroxyapatite were present and visible, they were both detected via stereomicroscopic analysis and SEM & EDS analysis in detail (Fig. 4.20 - 4.27). Besides according to the EDS analysis, the transformation of bovine hydroxyapatite to tricalcium phosphate was observed due to heat input during thermal spray coating process. The chemical formulae of the bond coating (Ni-20Cr) and the substrate (aluminumtitanate) were also double checked in samples taken in both groups of specimens (“L” types and “S” types; Fig. 4. 28 and 4.29). Some parts of bovine hydroxyapatite were removed during polishing with diamond paste for stereomicroscopic analysis and can be seen in Fig. 4.20, 4.22, 4.23, 4.26. In Fig. 4.28 and 4.29 the coating layers and the substrate were labeled by “1”, “2”, “3” to define the main coating layer, the bond coat and the substrate, respectively. The main coating thickness of the material varies from 72 to 201 μm and the bond coating layers’ were between 39-82 μm . Even though the bond coating layer deposition looked more homogenous due to its metallical nature, the coating layers were not very smoothly deposited on the substrate because of the discrepancies in the manual coating process. Therefore there are mainly four factors which could affect the layer thickness: a) speed of manual scan, b) distance to the sample, c) flame strength, d) spraying flux. The heat input didn’t only cause the transformation of the up coating layer but also thermal shock of some specimens, which was seen as cracks formed in Fig. 4.23 and 4. 24 following rapid cooling after thermal spray procedure.

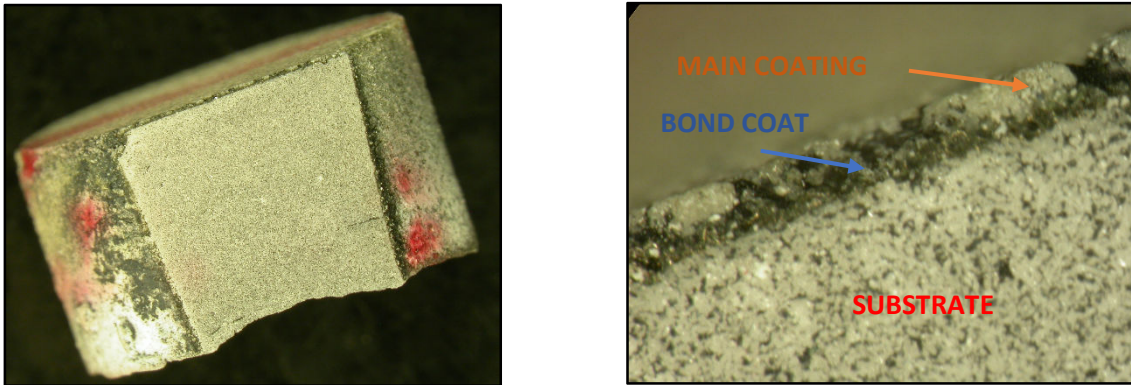


Figure 4.20. Stereomicroscopy (x50 at upper left and x 100 at upper right middle respectively) and SEM images (x250, back scattering mode, down) of the L1 type specimen.

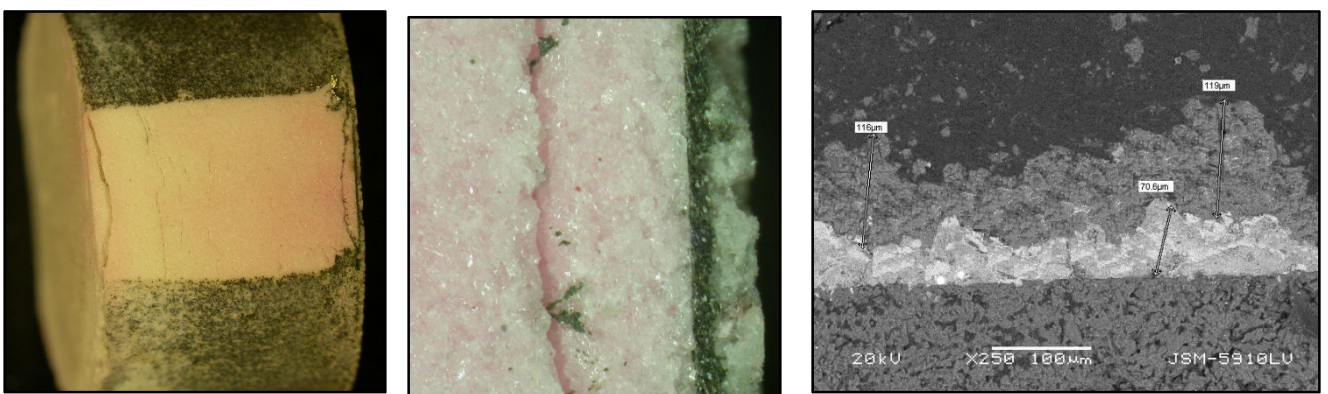


Figure 4.21. Stereomicroscopy (x50 at left and x 100 in the middle respectively) and SEM images (x250, back scattering mode, at right) of the L2 type specimen.

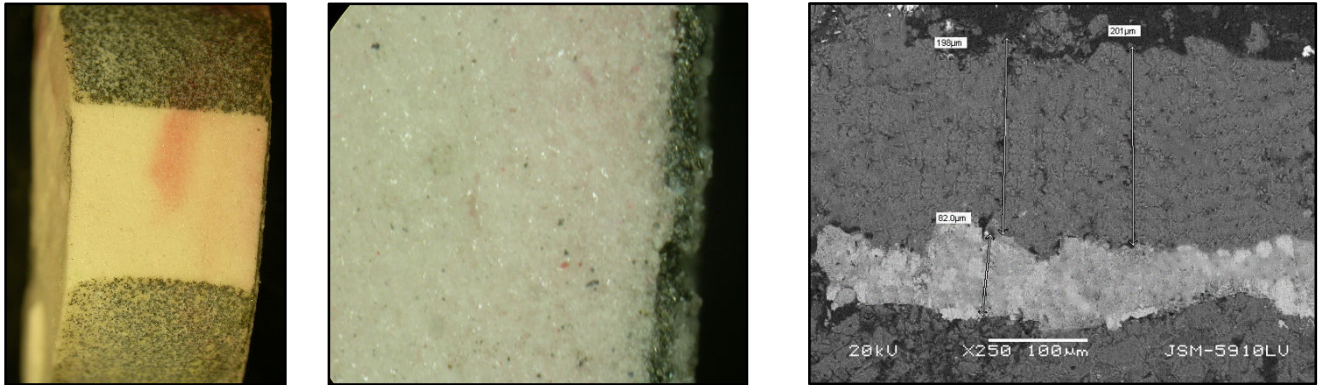


Figure 4.22. Stereomicroscopy (x50 at left and x 100 in the middle respectively) and SEM images (x250, back scattering mode, at right) of the L3 type specimen.

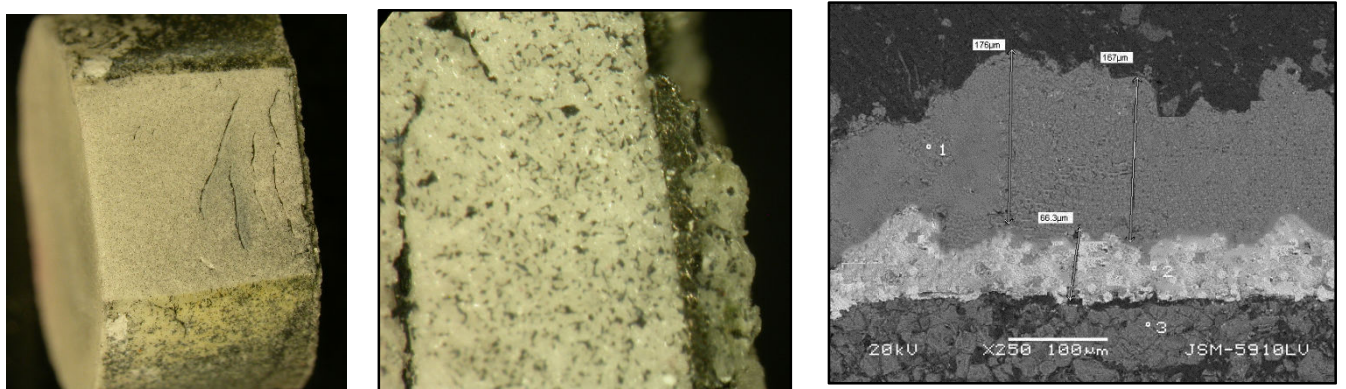


Figure 4.23. Stereomicroscopy (x50 at left and x 100 in the middle respectively) and SEM images (x250, back scattering mode, at right) of the L4 type specimen.

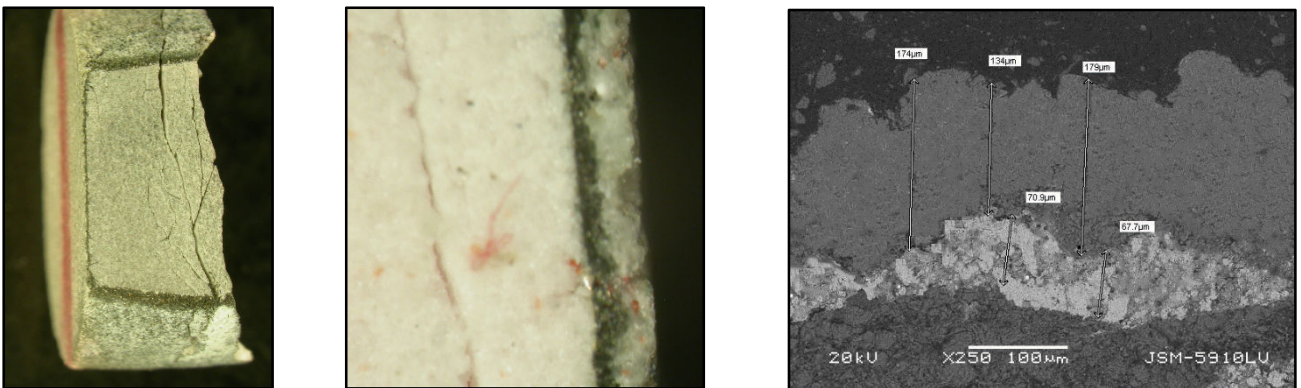


Figure 4.24. Stereomicroscopy (x50 at left and x 100 in the middle respectively) and SEM images (x250, back scattering mode, at right) of the S1 type specimen.

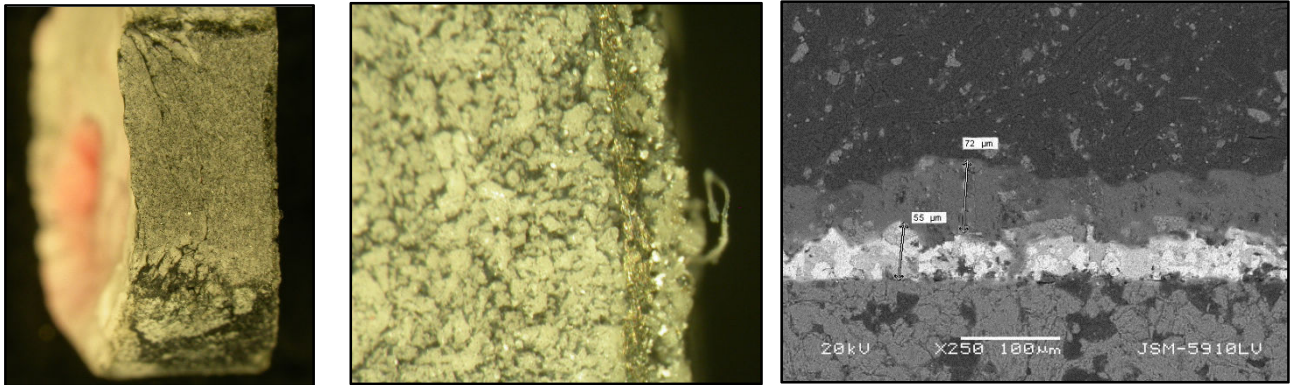


Figure 4.25. Stereomicroscopy (x50 at left and x 100 in the middle respectively) and SEM images (x250, back scattering mode, at right) of the S2 type specimen.

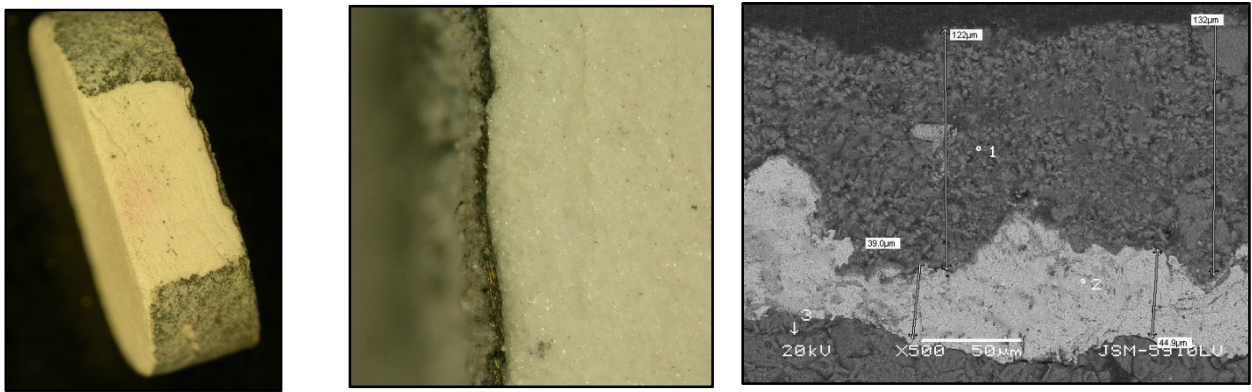


Figure 4.26. Stereomicroscopy (x50 at left and x 100 in the middle respectively) and SEM images (x250, back scattering mode, at right) of the S3 type specimen.

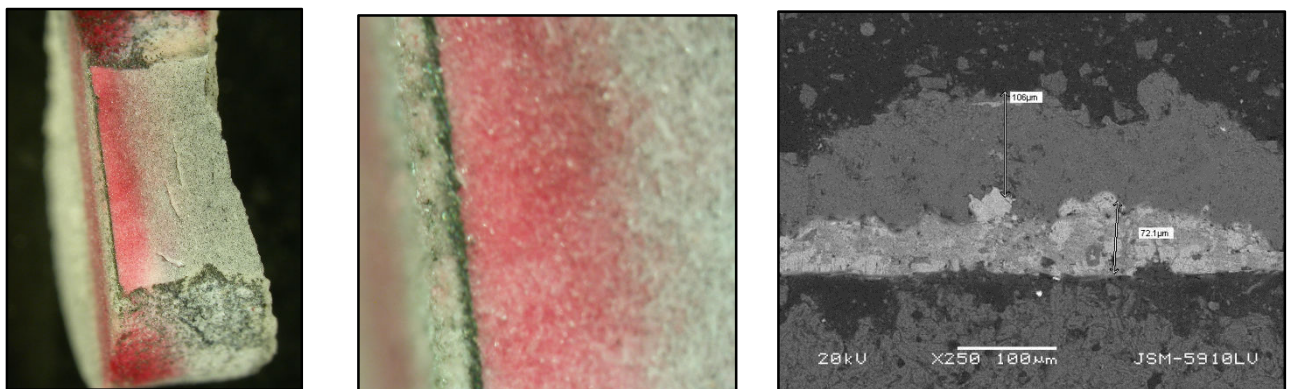
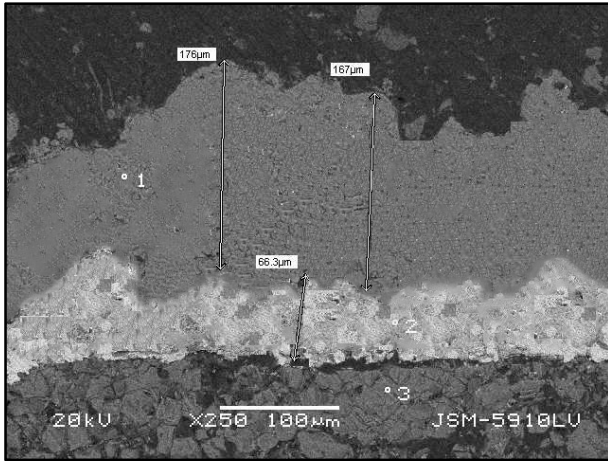


Figure 4.27. Stereomicroscopy (x50 at left and x 100 in the middle respectively) and SEM images (x250, back scattering mode, at right) of the S4 type specimen.



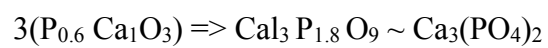
Processing option : All elements analyzed (Normalised)

Spectrum	O	P	Ca	Total
Spectrum "1"	44.46	18.78	36.76	100.00
Max.	44.46	18.78	36.76	100.00
Min.	44.46	18.78	36.76	100.00

$$\text{O: } 44.46 / 16 = 32.77 \sim 3$$

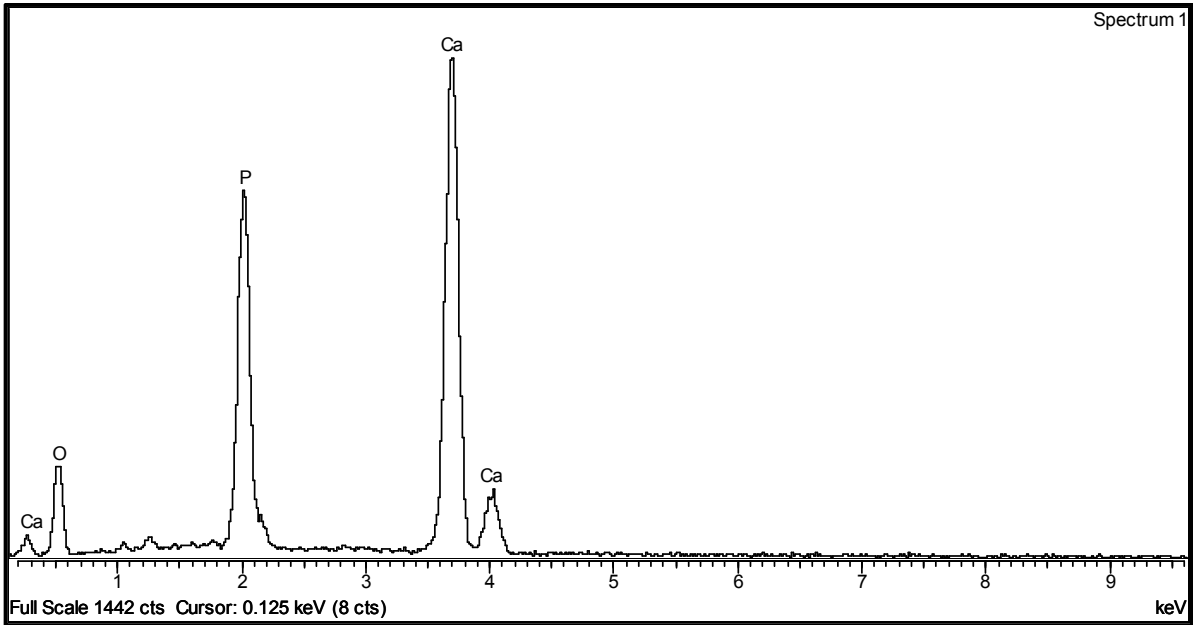
$$\text{P: } 18.78 / 31 = 0.605 \sim 0.6$$

$$\text{Ca: } 36.76 / 40 = 0.919 \sim 1$$



Tricalcium phosphate

All results in Weight Percent

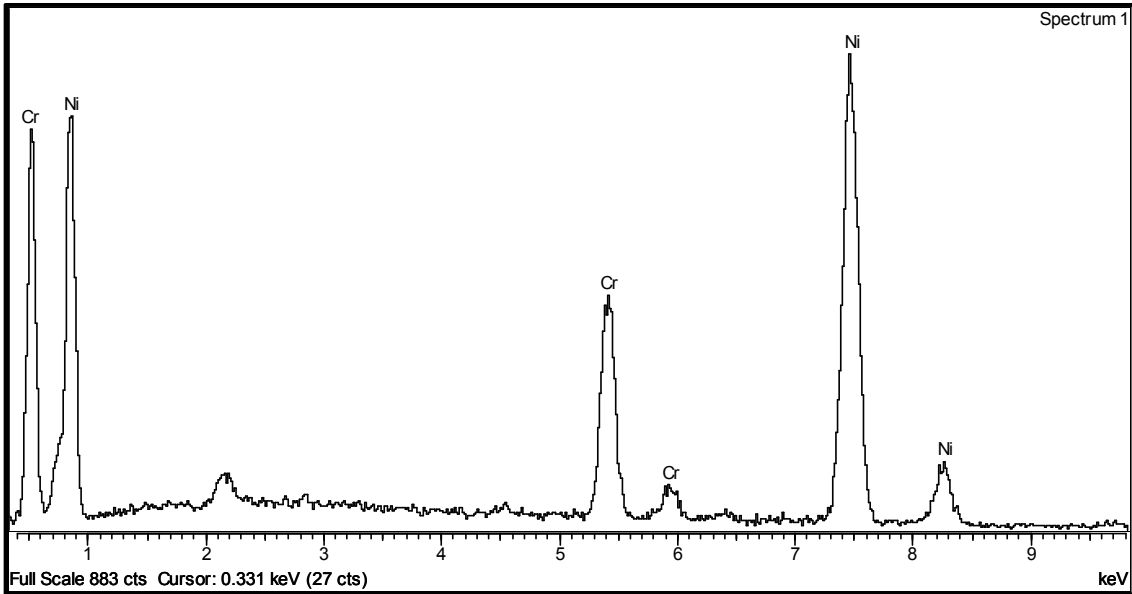


Processing option : All elements analyzed (Normalised)

Spectrum	Cr	Ni	Total
Spectrum "2"	18.64	81.36	100.00
Max.	18.64	81.36	100.00
Min.	18.64	81.36	100.00

Cr: $18.64 / 52 = 0.3584$ }
 Ni: $81.36 / 58.7 = 1.386$ } Ni-20Cr (Weight percentage) bond coating

All results in Weight Percent



Processing option : All elements analyzed (Normalised)

Spectrum	O	Al	Ti	Total
Spectrum "3"	42.63	20.44	36.92	100.00
Max.	42.63	20.44	36.92	100.00
Min.	42.63	20.44	36.92	100.00

O: $42.63 / 16 = 3.1 \sim 3$

Al: $20.44 / 27 = 0.93 \sim 1$

Ti: $36.92 / 48 = 0.49 \sim \frac{1}{2}$



All results in Weight Percent

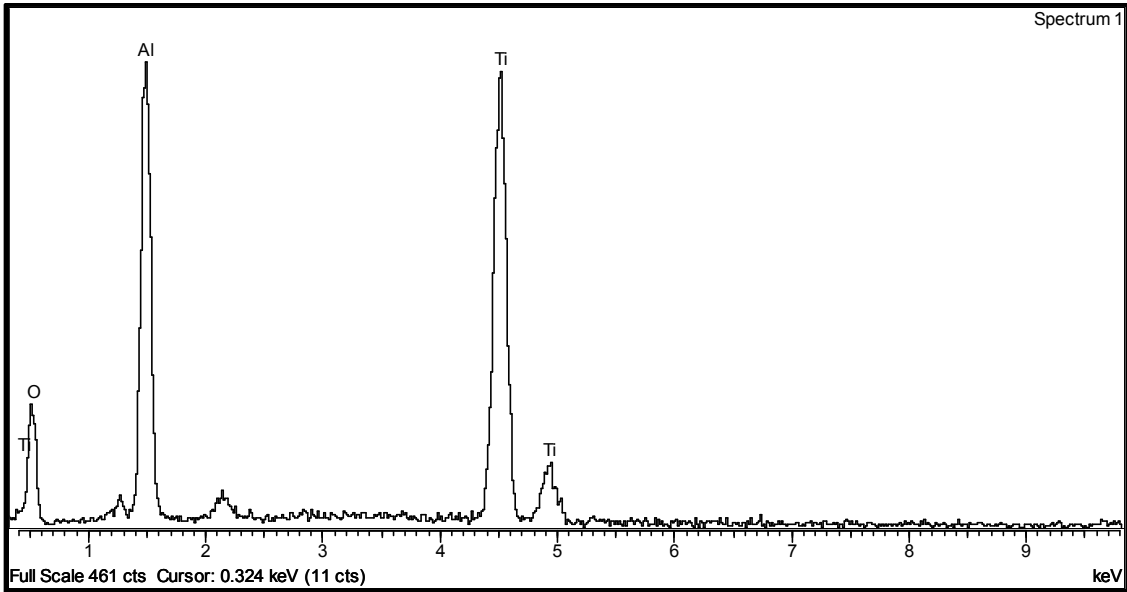
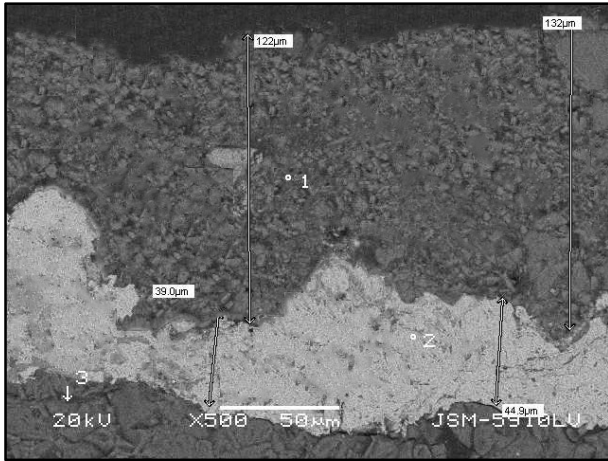


Figure 4.28. SEM microstructure (x2000, back scattering mode) and the related EDS analysis of L2 specimen indicating different composition at the different places of the structure “1” ,“2” and “3”.



Processing option : All elements analyzed (Normalised)

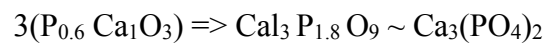
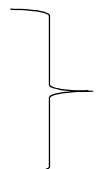
Spectrum	O	P	Ca	Total
Spectrum "1"	47.83	18.15	34.02	100.00
Max.	47.83	18.15	34.02	100.00
Min.	47.83	18.15	34.02	100.00

All results in Weight Percent

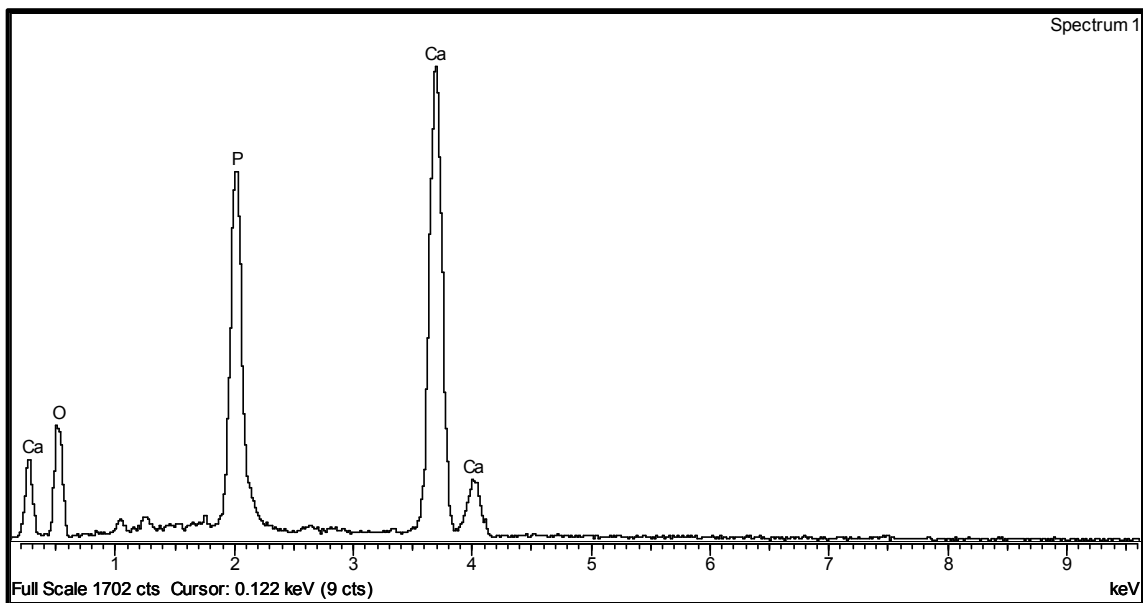
O: $47.83 / 16 = 2.98 \sim 3$

P: $18.15 / 31 = 0.5854 \sim 0.6$

Ca: $34.02 / 40 = 0.8505 \sim 1$



Tricalcium phosphate

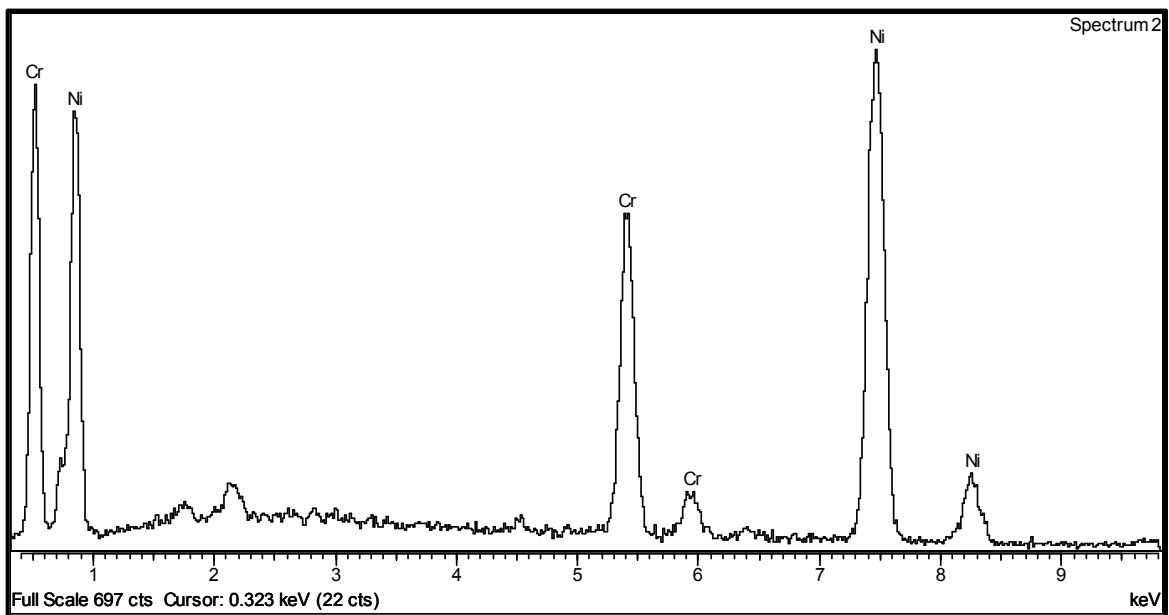


Processing option : All elements analyzed (Normalised)

Spectrum	Cr	Ni	Total
Spectrum "2"	22.37	77.63	100.00
Max.	22.37	77.63	100.00
Min.	22.37	77.63	100.00

Cr: $22.37 / 52 = 0.4302$
 Ni: $77.63 / 58.7 = 1.3224$ } Ni-20Cr (Weight percentage) bond coating

All results in Weight Percent



Processing option : All elements analyzed (Normalised)

Spectrum	O	Al	Ti	Total
Spectrum "3"	49.51	25.41	25.08	100.00
Max.	49.51	25.41	25.08	100.00
Min.	49.51	25.41	25.08	100.00

$O: 49.51 / 16 = 3.093 \sim 3,1$
 (Tialite)

$Al: 25.41 / 27 = 0.941 \sim 1$

$Ti: 25.08 / 48 = 0.5225 \sim \frac{1}{2}$

$2(Ti_{0.5}Al_1O_{3.1}) \Rightarrow Al_2Ti_{1.0}O_{6.2} \sim Al_2TiO_5$
 (Tialite)

All results in Weight Percent

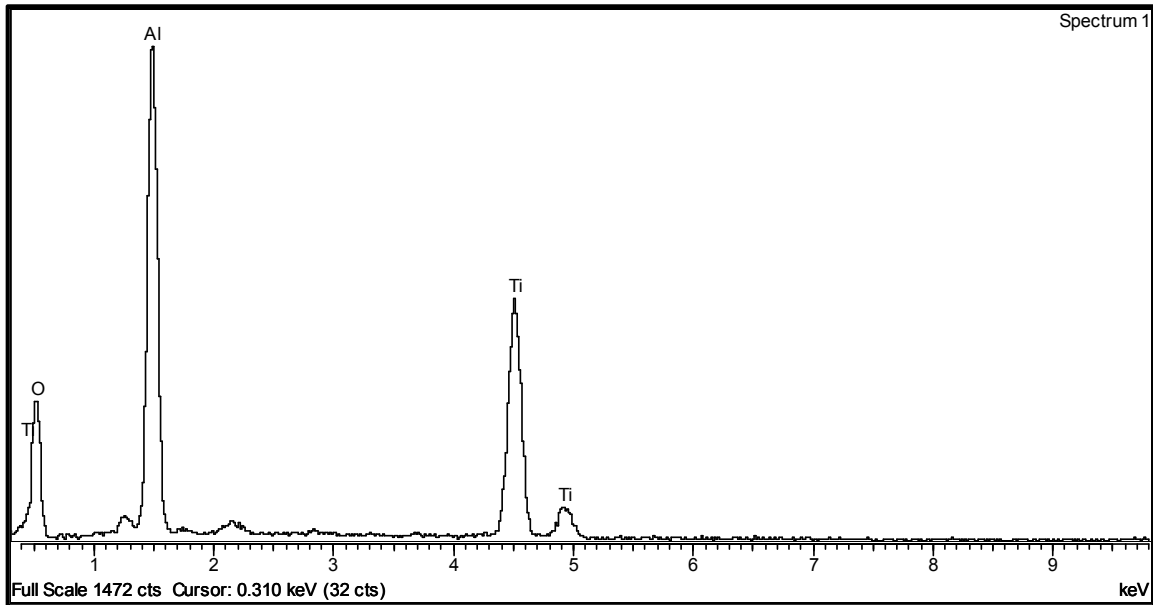


Figure 4.29. SEM microstructure (x2000, back scattering mode) and the related EDS analysis of S2 specimen indicating different composition at the different places of the structure "1", "2" and "3".

5. CONCLUSION

In this study, three objectives were pursued;

1-Beneficiation of Seydişehir Alumina and its characterization

2-Production of Alumina-Titania Biocomposite and its characterization

3-Coating with HA the alumina-titania substrate using flame spray process and its characterization

Amongst them, the beneficiation of Seydişehir alumina was successfully terminated decreasing not only sodium content but also iron oxide content offering a new method for this procedure [51].

25 % of the alumina produced in Seydisehir alumina factory is α -alumina, the rest is the aluminum oxide phase. So there was still a great amount of alumina untransformed and also some quantity of possible boehmite phase remained. But applying the new method explained in detail earlier proposed during this research; following beneficiation and calcination at 1200 °C, the complete transformation of aluminum oxides and the elimination of sodium oxide were observed.

After ball milling using alumina balls (10 mm of diameter) for 24 hours, grain sizes were decreased and observed using SEM. It is realized that, leaching time is also effective on the diminution of particle size. The average particle size was 31,20 μm in this range. It can be claimed that the size distribution is mono dispersive. The SEM results verified our laser particle sizer's findings and also with increasing leaching time, a diminution in particle sizes is also observed by SEM.

In this research, the second object was to produce an alumina-titania biocomposite, at relatively lower temperature. This can be achieved by different compositions easier to produce in which tialite synthesis can be done over 1800 °C; but the raw batch choice was correctly decided obtaining single tialite phase in the structure after sintering at 1600 °C. The possible residual phases -such as spinel-, not transformed or not at exact tialite composition were not detected as their weight percentage was under 5 wt.%. In addition of these results, the choice of Seydişehir alumina was also proved correct as it increased the hardness and compressive strength values comparing to the laboratory scale alumina. Also a new material, the tialite as a new biomaterial was proposed in this research. After

the Archimèdes density measurement, it was realized that the -S- type specimens were slightly denser comparing to -L- type specimens –which could be considered in normal range (3-3,4 g/cm³) of the tialite. The porosity of the material was also less in the S type specimens.

The diffraction peaks observed in XRD patterns belonged to tialite phase completely, the result pointed out success in obtaining tialite phase formation even without adding any additives at 1600 °C, lower than the temperature mentioned in literature [17-34]. The main difference was the difference in peak intensities for different batches (samples). “S” specimens showed higher values than other. This result could be attributed to the residual iron oxide content of –S- type specimens comparing to –L- type which were much more than industrially purified and processed alumina powders.

According to SEM microstructure of the specimens due the morphology of the starting powders, -L- type specimens’ grains were much more spherical while –S- type specimens were quite disordered, but less porous which was also coherent with the Archimedes density results. It was also obvious that, the addition of 2,5 wt. % MgO and 1 wt. % SiO₂ (Quartz phase) caused the extreme grain growth of the main phase in both group of specimens: the inclusions situated in the grain boundaries didn’t help to slow down this phenomenon in –L- type specimens. Besides this, the finer grains were found in the microstructure of S3 type specimen which had the lowest porosity and the highest density amongst all the specimens. But as the main matrix is much more brittle, the inclusions behave as the crack stopping areas at the lower percentage of magnesia and silica. When the addition of silica was very little, no glassy phase was observed in the microstructure. The microcracks present could have the major contribution in its low thermal coefficient, anisotropy and low electrical conductivity but also low compression strength. Hardness was also increased by the addition of sintering aids.

In this research, as it was expected, the EDS analysis of L1 ad S1 type materials showed a homogeneous structure, there was only the aluminum titanate matrix composed of alumina and titania phases present in the structure confirmed by EDS analysis; in addition small amounts of spinel was also detected which was thought to ameliorate the mechanical properties. In the EDS analysis of L4 and S4 samples, it was concluded that the angular, sharp edged inclusions in the grain boundaries contained mainly alumina-titania and little amounts of MgO and SiO₂, indicating the presence of spinel phase.

The hardness and compressive strength of -S-type materials were higher, which was consistent with the XRD analysis, Archimèdes density measurement and SEM microstructure evaluation.

In this research the final objective was the production of a successful coating applied by the combustion flame spray to coat the HA, here using bovine HA. As the substrate was hard but brittle, the surface after coating became tougher. The coating was very tough with evidence of no visible crack formation could be observed. The coating thickness of these materials was adequate for a possible tymphonoplastic implant to be used in the ear. The main coating thickness of the material varies from 72 to 201 μm and the bond coating layers' were between 39-82 μm . This showed a heterogenous coating thickness which was attributed to random nature of the manual process. The heat input did not only cause the transformation of the upper coating layer but also caused thermal shock of some specimens. Further application of this procedure in the industry should be carried out using an automated system and a peripheral cooling circle for a better and homogenous coating and for preventing thermal shock effect during rapid cooling. Further research will be performed on the performance of these tialite samples in SBF solution "*in vitro*" in an isothermal system.

REFERENCES

- [1] “Biomaterials, Principles and Applications”, ed. Joon B. Park, Joseph D. Bronzino, , CRC Press, Boca Raton, FL, 2003.
- [2] Soo Whon Lee, Carlos Morillo, Joaquín Lira-Olivares, Seung Ho Kim, Tohru Sekino, Koichi Niihara, Bernard J. Hockey, “Tribological and microstructural analysis of Al₂O₃/TiO₂ nanocomposites to use in the femoral head of hip replacement”, *Wear* 255 (2003) 1040–1044.
- [3] M. Jayasankar, S. Ananthakumar, P. Mukundan, W. Wunderlich, K.G.K. Warriar, “Al₂O₃ @ TiO₂—A simple sol–gel strategy to the synthesis of low temperature sintered alumina–aluminium titanate composites through a core–shell approach”, *Journal of Solid State Chemistry* 181 (2008) 2748–2754.
- [4] E. Vernè, M. Bosetti, C. Vitale Brovarone, C. Moiescu, F. Lupo, S. Spriano, M. Cannas, “Fluoroapatite glass-ceramic coatings on alumina: structural, mechanical and biological characterisation”, *Biomaterials* 23 (2002) 3395–3403.
- [5] <http://evertsmith.com/treatment/exceed-acetabular-cup/>
- [6] P. Souza Santos, H. Souza Santos, S.P. Toledo, “Standard Transition Aluminas. Electron Microscopy Studies”, *Materials Research*, Vol. 3, No. 4, 104-114, 2000.
- [7] <http://theestory.com/topics/6480>.
- [8] Turan Tambaş, Serdar Özgen, “Seydişehir alüminasının slip döküm parametrelerinin Belirlenmesi”, *İTÜ Dergisi/D Mühendislik*, Cilt:6, Sayı:2, 83-94, Nisan 2007.
- [9] <http://www.diva-portal.org/smash/get/diva2:126149/FULLTEXT01.pdf>
- [10] R. Janes, L.J. Knightley, “Synthetic routes to microfine biphasic titania–alumina powders”, *Dyes and Pigments* 56 (2003) 111–124.
- [11] Ulrike Diebold, “The surface science of titanium oxide”, *Surface Science Reports* 48 (2003) 53-229.
- [12] J.M. Macak, H. Tsuchiya, A. Ghicov, K. Yasuda, R. Hahn, S. Bauer, P. Schmuki, “TiO₂ nanotubes: Self-organized electrochemical formation, properties and applications”, *Current Opinion in Solid State and Materials Science* 11 (2007) 3–18.
- [13] Johan Forsgren, Fredrik Svahn, Tobias Jarmar, Håkan Engqvist, “Formation and adhesion of biomimetic hydroxyapatite deposited on titanium substrates”, *Acta Biomaterialia* 3 (2007) 980–984.

- [14] Tadashi Kokubo, "Apatite Formation on Surfaces of Ceramics, Metals and Polymers in Body Environment", *Acta mater.* Vol. 46, No. 1, pp. 2519--2527, 1998.
- [15] Hanan H. Beherei, Khaled R. Mohamed, Gehan T. El-Bassyouni, "Fabrication and characterization of bioactive glass (45S5)/titania biocomposites", *Ceramics International* 35 (2009) 1991–1997.
- [16] Mahlaba A. Debeila, Mpfuzeni C. Raphulu, Emma Mokoena, Miguel Avalos, Vitalii Petranovskii, Neil J. Coville, Mike S. Scurrall, "The effect of gold on the phase transitions of titania", *Materials Science and Engineering A* 396 (2005) 61–69.
- [17] Chun-Hong Chen, Hideo Awaji, "Temperature dependence of mechanical properties of aluminum titanate ceramics", *Journal of the European Ceramic Society* 27 (2007) 13–18.
- [18] <http://www.azom.com/article.aspx?ArticleID=1223>
- [19] S. Bueno, M.H. Berger, R. Moreno, C. Baudín, "Fracture behaviour of microcrack-free alumina–aluminium titanate ceramics with second phase nanoparticles at alumina grain boundaries", *Journal of the European Ceramic Society* 28 (2008) 1961–1971.
- [20] Sang-Yeup Park, Sug-Woo Jung, Yung-Bin Chung, "The effect of starting powder on the microstructure development of alumina–aluminum titanate composites", *Ceramics International* 29 (2003) 707–712.
- [21] M. Sobhani, H.R. Rezaie, R. Naghizadeh, "Sol–gel synthesis of aluminum titanate (Al_2TiO_5) nano-particles", *Journal of Materials Processing Technology* 206 (2008) 282–285.
- [22] S. Ananthakumar, M. Jayasankar, K.G.K. Warriar, "Microstructural, mechanical and thermal characterisation of sol–gel-derived aluminium titanate–mullite ceramic composites", *Acta Materialia* 54 (2006) 2965–2973.
- [23] C.G. Shi and I.M. Low, "Effect of Spodumene Additions on the Sintering and Densification of Aluminum Titanate", *Materials Research Bulletin*, Vol. 33, No. 6, pp. 817–824, 1998.
- [24] E. Otterstein, G. Karapetyan, R. Nicula, M. Stir, C. Schick, E. Burkel, "Sol–gel synthesis and characterization of fine-grained ceramics in the alumina–titania system", *Thermochimica Acta* 468 (2008) 10–14.
- [25] Ana M. Segadães, Márcio R. Morelli, Ruth G. A. Kiminami, "Combustion Synthesis of Aluminium Titanate, *Journal of the European Ceramic Society* 18 (1998) 771–781.

- [26] I.D. Alecu, R.J. Stead, “Further tailoring of material properties in non-equimolar aluminium titanate ceramic materials, *Journal of the European Ceramic Society* 27 (2007) 679–682.
- [27] I.M. Low, Z. Oo, “Reformation of phase composition in decomposed aluminium titanate”, *Materials Chemistry and Physics* 111 (2008) 9–12.
- [28] R.D. Skala, D. Li, I.M. Low, “Diffraction, structure and phase stability studies on aluminium titanate”, *Journal of the European Ceramic Society* 29 (2009) 67–75.
- [29] I.M. Low, Z. Oo, B.H. O’Connor, “Effect of atmospheres on the thermal stability of aluminium titanate”, *Physica B* 385–386 (2006) 502–504.
- [30] R. Naghizadeh, H.R. Rezaie, F. Golestani-fard, “The influence of composition, cooling rate and atmosphere on the synthesis and thermal stability of aluminum titanate”, *Materials Science and Engineering B* 157 (2009) 20–25.
- [31] T. Korim, “Effect of Mg^{2+} - and Fe^{3+} -ions on formation mechanism of aluminium titanate”, *Ceramics International* 35 (2009) 1671–1675.
- [32] H.R. Rezaie, R. Naghizadeh, N. Farrokhnia, S. Arabi, M. Sobhani, “The effect of Fe_2O_3 addition on tialite formation”, *Ceramics International* 35 (2009) 679–684.
- [33] S. M. Lang, C. L. Fillmore, L. H. Maxwell, “The System Beryllia-Alumina-Titania: Phase Relations and General Physical Properties of Three-Component Porcelains”, *Journal of Research of the National Bureau of Standards* Vol. 48, No. 4, April 1952, Research Paper 2316.
- [34] A.S. YGul’ko Berezhnoi, N.V., “The system $MgO-Al_2O_3-TiO_2$ ”, *Ukr. Khim. Zh.* (Russ. Ed.), 21[2] 158-166 (1955).
- [35] Sumit Pramanik, Avinash Kumar Agarwal, K.N. Rai, Ashish Garg, “Development of high strength hydroxyapatite by solid-state-sintering process”, *Ceramics International* 33 (2007) 419–426.
- [36] María Vallet-Regí, José María González-Calbet, “Calcium phosphates as substitution of bone tissues”, *Progress in Solid State Chemistry* 32 (2004) 1–31.
- [37] Dean-Mo Liu, T. Troczynski, Wenjea J. Tseng, “Aging effect on the phase evolution of water-based sol–gel hydroxyapatite”, *Biomaterials* 23 (2002) 1227–1236.
- [38] Biqin Chen, Tao Zhang, Jingxian Zhang, Qingling Lin, Dongliang Jiang, “Microstructure and mechanical properties of hydroxyapatite obtained by gel-casting process”, *Ceramics International* 34 (2008) 359–364.

- [39] Viviane V. Silva, Fernando S. Lameiras, Rosana Z. Domingues, “Microstructural and mechanical study of zirconia-hydroxyapatite (ZH) composite ceramics for biomedical applications”, *Composites Science and Technology* 61 (2001) 301-310.
- [40] F.N. Oktar, “Hydroxyapatite–TiO₂ composites”, *Materials Letters* 60 (2006) 2207–2210.
- [41] Azade Yelten, Suat Yilmaz, Faik N. Oktar, “Sol–gel derived alumina–hydroxyapatite–tricalcium phosphate porous composite powders”, *Ceramics International* 38 (2012) 2659–2665.
- [42] S. Salman, O. Gunduz, S. Yilmaz, M. L. Öveçoğlu, Robert L. Snyder, S. Agathopoulos, F.N. Oktar, “Sintering effect on mechanical properties of composites of natural hydroxyapatites and titanium”, *Ceramic International* 35 (2009) 2965-2971.
- [43] Zeming He, J. Ma, Cong Wang, “Constitutive modeling of the densification and the grain growth of hydroxyapatite ceramics”, *Biomaterials* 26 (2005) 1613–1621.
- [44] Kyuseog Hwang, Jongeun Song, Boan Kang, Yeongjoo Park, “Sol–gel derived hydroxyapatite films on alumina substrates”, *Surface and Coatings Technology* 123 (2000) 252–255.
- [45] X. Miao, Y. Hu, J. Liu, X. Huang, “Hydroxyapatite coating on porous zirconia”, *Materials Science and Engineering C* 27 (2007) 257–261.
- [46] G. Dadsı, O. Laboux, R. Le Geros, “Outcome and perspectives in bioactive coatings: What’s new, what’s coming”, *ITBM-RBM* 2002; 23: 317-325, Elsevier SAS.
- [47] L. Duta, F.N. Oktar, G.E. Stan, G. Popescu-Pelin, N. Serban, C. Luculescu, I.N. Mihailescu, “Novel doped hydroxyapatite thin films obtained by pulsed laser deposition”, *Applied Surface Science* 265 (2013) 41– 49.
- [48] L. Sevgi Ozyegin, Faik N. Oktar, Gultekin Goller, E. Sabri Kayali, Tokay Yazici, “Plasma-sprayed bovine hydroxyapatite coatings”, *Materials Letters* 58 (2004) 2605–2609.
- [49] Qing Ye, Katsuichiro Ohsaki, Kunio Li, Dong-Jun Li, Chun-Sheng Zhu, Teruhiro Ogawa, Satoru Tenshin, Teruko Takano-Yamamoto, “Histological reaction to hydroxyapatite in the middle ear of rats”, *Auris Nasus Larynx* 28 (2001) 131–136.
- [50] “Handbook of Thermal Spray Technology”, ed. J.R. Davis, Davis & Associates, September 2004 ASM International, USA.

[51] Ekin elik, Burcu N. etiner, Z. Engin Erkmn, “Ceramic Filter Production from Seydişehir Alumina”, SERES Eskişehir 2011, poster and oral presentation.

CURRICULUM VITAE

Name, Surname : Burcu Nilgün ÇETİNER
Birth Place and Date : Üsküdar, 21/03/1984
Foreign Language : Fransızca, İngilizce ve İtalyanca
E-mail : nilgun.cetiner@marmara.edu.tr

Education

Degree	Program	Üniversite/Lise	Mezuniyet Yılı
Lise	Science	Galatasaray High School	2003
Üniversite	Dept. of Metallurgical and Materials Eng.	Kocaeli University	2008

Professional Life

Year	Company/Institution	Job
2009	Marmara University	Research Assistant